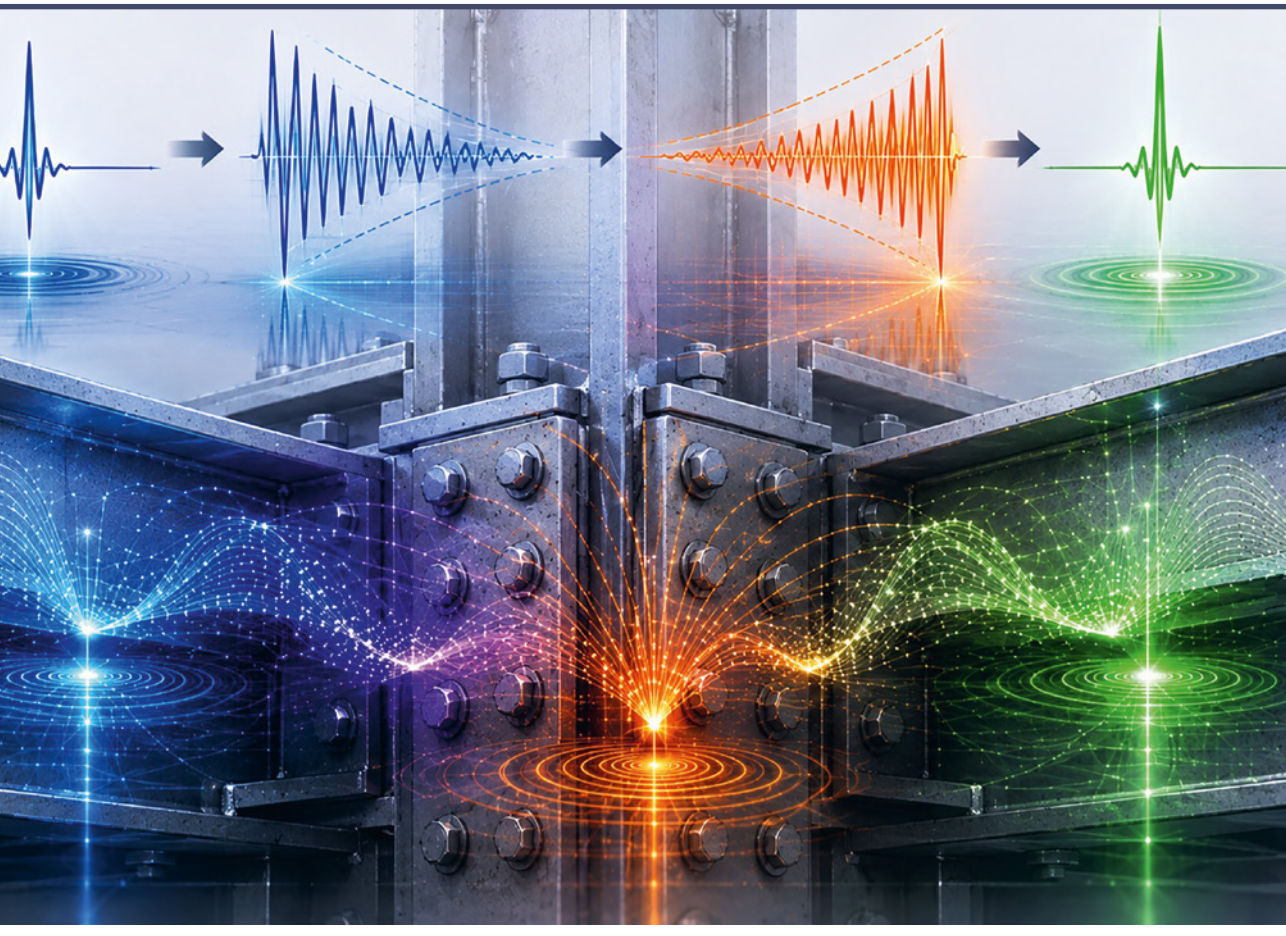
RIGA TECHNICAL UNIVERSITY

Viktors Kurtenoks

MULTIDIMENSIONAL ASSESSMENT OF STRUCTURAL JOINT INTEGRITY VIA AXIS-MATCHED RESPONSE CORRELATION ENHANCED BY TIME-REVERSAL IMPACT FOCUSING

Doctoral Thesis



RTU Press
Riga 2026

RIGA TECHNICAL UNIVERSITY
Faculty of Civil and Mechanical Engineering
Institute of High-Performance Materials and Structures

Viktors Kurtenoks
Doctoral Student of the Study Programme “Civil Engineering”

MULTIDIMENSIONAL ASSESSMENT OF STRUCTURAL JOINT INTEGRITY VIA AXIS-MATCHED RESPONSE CORRELATION ENHANCED BY TIME-REVERSAL IMPACT FOCUSING

Doctoral Thesis

Scientific supervisors
Professor Dr. sc. ing.
JEVGENIJS BARKANOVS
Dr. sc. ing.
ALEKSEJS TATARINOVS

Riga 2026

Kurtenoks, V. Multidimensional assessment of structural joint integrity via axis-matched response correlation enhanced by time-reversal impact focusing. Doctoral Thesis. – Riga: RTU Press, 2026. – 138 p.

Published in accordance with the decision of the Promotion Council “RTU P-06” of 17 August 2026, Decision No. 04030-9.6/22.

The cover image was created by the author using generative artificial intelligence tools.

DOCTORAL THESIS PROPOSED TO RIGA TECHNICAL UNIVERSITY FOR THE PROMOTION TO THE SCIENTIFIC DEGREE OF DOCTOR OF SCIENCE

To be granted the scientific degree of Doctor of Science (Ph. D.), the present Doctoral Thesis has been submitted for the defence at the open meeting of RTU Promotion Council on 27 November 2026 at 14:00 at the Faculty of Civil and Mechanical Engineering of Riga Technical University, 6A Ķīpsalas Street, Room 538.

OFFICIAL REVIEWERS

Professor Dr. sc. ing. Aleksandrs Korjakins
Riga Technical University, Latvia

Professor Dr. habil. sc. ing. Igor Kabashkin
Transport and Telecommunication Institute, Latvia

Professor Dr. Raimondas Pomarnacki
Vilnius Gediminas Technical University, Lithuania

DECLARATION OF ACADEMIC INTEGRITY

I hereby declare that the Doctoral Thesis submitted for the review to Riga Technical University for the promotion to the scientific degree of Doctor of Science (Ph. D.) is my own. I confirm that this Doctoral Thesis had not been submitted to any other university for the promotion to a scientific degree.

Viktors Kurtenoks ……. (signature)
Date: ……

The Doctoral Thesis has been written in English. It consists of an Abstract; 7 chapters; 18 figures; 2 tables; 9 appendices; the total number of pages is 138, including appendices. The Bibliography contains 33 titles.

ANOTĀCIJA

Uzticama konstrukciju savienojumu integritātes novērtēšana ir būtiska inženierbūvju drošības un ekspluatācijas piemērotības nodrošināšanai, tomēr esošajām diagnostikas pieejām konstrukciju strukturālā stāvokļa monitoringā bieži ir raksturīga virzieniski nepilnīga novērojamība. Lielākajā daļā metožu mērījumi faktiski ir viendimensionāli vai arī, izmantojot daudzasu sensorus, tie joprojām balstās uz tādu ierosmi, kas nenodrošina kontrolētu daudzdimensionālu reakciju intereses punkta apkārtnē. Tā rezultātā agrīnas stadijas, pa asīm selektīvas degradācijas pazīmes var palikt neatklātas, tādējādi ierobežojot pašreizējās diagnostikas prakses uzticamību.

Šajā promocijas darbā, kas sagatavots kā publikāciju kopums, ir izstrādāta un eksperimentāli validēta sinhronizēta daudzdimensionāla diagnostikas pieeja, kas paredzēta minēto ierobežojumu pārvarēšanai. Zinātniskā novitāte ir saistīta ar piecu savstarpēji atkarīgu komponentu sistemātisku integrāciju: trīsdimensiju paātrinājuma mērījumu pāriem konstrukciju savienojuma pretējās pusēs kopīgā reakcijas apgabalā, kas fokusēts ar laika reversijas metodi; kontrolētu daudzdimensionālu ierosmi, kas balstīta uz laika reversijas viļņu fokusēšanas principiem; sinhronizētiem ierosmes un mērīšanas kanāliem; katras ass koherences novērtēšanu starp pretējo pušu paātrinājuma reakciju pāriem, kā arī virzienisko indikatoru apvienošanu vienā skalārā savienojuma stāvokļa metrikā.

Promocijas darba pamatā ir trīs savstarpēji papildinošas publikāciju grupas, kas veido vienotu pētījuma trajektoriju. Pirmajā grupā ir izveidots pa asīm saskaņotu daudzasu reakciju mērījumu pamats, kā arī korelācijā balstīti indikatori, skalāru metriku apvienošanas pieeja un degradācijas imitācijas procedūras dažādiem konstrukciju objektiem un materiāliem. Otrā grupa sniedz laika reversijas viļņu fokusēšanas teorētisko bāzi, kas nepieciešama, lai reakciju salīdzināšanu attiecinātu arī uz kontrolētu daudzdimensionālu ierosmi. Trešā grupa aplūko augstas precizitātes laika mērīšanas un daudzkanālu sinhronizācijas metodes, kas nepieciešamas konsekventas laika reversijas fokusēšanas nodrošināšanai sadalītās mērījumu sistēmās ar digitāli savienotiem sensoriem un garām, pret trokšņiem noturīgām pārraides līnijām. Kopā šīs grupas veido piedāvātās pieejas metodoloģisko pamatu, kurā daudzasu reakcijas novērtēšana, ierosmes kontrole un laika ziņā saskaņota izkliedētā mērīšana tiek uzskatītas par vienotas konstrukciju savienojumu diagnostikas metodoloģijas savstarpēji saistītām sastāvdaļām.

Integrētā metodoloģija ir validēta sinhronizētā daudzdimensionālā konstrukciju savienojuma eksperimentā, kurā pakāpeniska degradācija tiek imitēta, kontrolēti samazinot skrūves pievilkšanas momentu astoņos posmos. Rezultāti demonstrē, ka kontrolēta daudzdimensionāla ierosme uzlabo virzienisko novērojamību, samazina no ass atkarīgu reakciju neviennozīmību un uzlabo reakciju reproducējamību pakāpeniskas degradācijas apstākļos. Apvienotā daudzasu komponentu koherences metrika (Multiaxial Component Coherence Metric, MCCM) uzrāda monotonu samazināšanos visos degradācijas posmos, nodrošinot tādu diagnostisko jutību, ko atsevišķu asu indikatori nespēj konsekventi sasniegt.

Metodoloģiskās sastāvdaļas ir dokumentētas astoņās zinātniskajās publikācijās un vienā izsniegtā patentā. Šajā darbā ir integrēta aparatūras izstrāde, sinhronizācija, uz viļņu procesiem balstīta ierosmes kontrole un konstrukciju daudzasu reakcijas novērtēšana reproducējamā ietvarā konstrukciju savienojumu nesagraujošai novērtēšanai.

ABSTRACT

Reliable assessment of structural joint integrity is essential for ensuring the safety and serviceability of engineering structures, yet existing diagnostic approaches in structural health monitoring frequently suffer from directionally incomplete observability. Most methods are effectively one-dimensional in sensing or, when multiaxial sensing is employed, still rely on excitation that does not ensure a controlled multidimensional response around the point of interest. As a result, early-stage, axis-selective degradation signatures may remain undetected, limiting the diagnostic reliability of current practice.

This doctoral thesis, through publications, develops and experimentally validates a synchronized multidimensional diagnostic approach designed to overcome these limitations. The core innovation lies in the systematic integration of five interdependent components: paired three-dimensional acceleration measurements on opposite sides of a structural joint within a shared time-reversal-focused response domain, controlled multidimensional excitation based on time-reversal wave-focusing principles, synchronized excitation and sensing channels, per-axis coherence evaluation between paired opposite-side acceleration responses, and fusion of directional indicators into a single scalar metric of joint condition.

The thesis is supported by three complementary publication groups forming a unified research trajectory. The first group establishes axis-matched multiaxial response measurements, correlation-based indicators, scalar-metric fusion, and degradation emulation across different structural objects and materials. The second group provides the time-reversal wave-focusing basis required to extend response comparison toward controlled multidimensional excitation. The third group addresses high-precision timing and multichannel synchronization methods required to enable consistent time-reversal focusing in distributed measurement systems with digitally connected sensors and long-distance noise-immune transmission lines. Together, these groups form the methodological basis of the proposed approach, in which multiaxial response evaluation, excitation control, and time-consistent distributed sensing are treated as interconnected components of a single structural joint diagnostic methodology.

The integrated methodology is validated through a synchronized, multidimensional structural joint experiment that emulates progressive degradation via controlled bolt-torque reduction over eight stages. The results demonstrate that controlled multidimensional excitation improves directional observability, reduces axis-dependent response ambiguity, and enhances response reproducibility under progressive degradation conditions. The fused Multiaxial Component Coherence Metric (MCCM) exhibits a monotonic decrease across all degradation stages, providing a diagnostic sensitivity that individual single-axis indicators cannot consistently achieve.

The methodological components are documented in eight scientific publications and one granted patent. This thesis integrates hardware design, synchronization, wave-based excitation control, and multiaxial structural response evaluation into a reproducible framework for the non-destructive assessment of structural joints.

CONTENTS

LIST OF ABBREVIATIONS 8
CHAPTER 1: OVERVIEW 9
1.1. Introduction 9
1.2. State of the Art 9
1.2.1. Localized Joint Diagnostic Approaches 10
1.2.2. Response Comparison and Multiaxial Observability 11
1.2.3. Time-Reversal Methods and Axis-Specific Excitation Control 11
1.2.4. Distributed Acquisition and Synchronization 12
1.2.5. Research Gap 12
1.3. Aim of Research 12
1.4. Main Statement 13
1.5. Scientific Novelty 13
1.6. Research Objectives 13
1.7. Structure of the Thesis 14
1.8. Publications and Scientific Dissemination 14
CHAPTER 2: METHODOLOGICAL SCOPE AND PREREQUISITES 17
2.1. Measured Quantities and Scale Treatment 17
2.2. Experimental Objects 17
2.3. Sensor Configuration and Positioning Requirements 17
2.3.1. Virtual Coaxial Alignment Requirement 18
2.3.2. Effect on Waveform Comparability (RCR) 18
2.3.3. Effect on Time-Reversal Defocusing 19
2.3.4. Practical Bandwidth Criterion for Sensor Spacing 19
2.4. Actuator Configuration and Positioning Requirements 20
2.5. Degradation Emulation 21
2.6. Time-Reversal Impact Focusing Principles 21
2.7. Multidimensional Time-Reversal Impact Focusing (MTRIF) 23
2.8. Time-Domain Coherence Prerequisite and CNSS Rationale 25
2.9. Response Coherence Ratio (RCR) 25
2.10. Multiaxial Component Coherence Metric (MCCM) 26
CHAPTER 3: HARDWARE–SOFTWARE PLATFORM FOR DATA ACQUISITION 27
3.1. Purpose and Scope of the Platform 27
3.2. System Overview and Core Architecture 27
3.3. Excitation Subsystem 28

3.4. Sensing, Acquisition, and Noise-Robust Data Transfer 28
3.5. Time-Reference Support and CNSS Observables 28
3.6. Control Software and User Interface 29
3.7. Key Specifications of the Platform 29
CHAPTER 4: DATA COLLECTION 31
4.1. Baseline Object and Joint Configuration 31
4.1.1. Sensor Placement 32
4.1.2. Actuator Placement 32
4.1.3. Degradation Method 32
4.2. Measurement Steps 32
CHAPTER 5: SIGNAL PROCESSING AND METRIC EVALUATION 34
5.1. Per-Axis RCR Evaluation 34
5.2. MCCM Computation 35
CHAPTER 6: METRIC EVALUATION RESULTS 36
6.1. Per-Axis RCR Repeatability Across Five Measurement Cycles 36
6.2. MCCM Repeatability and Degradation Trend 36
6.3. Dispersion Analysis of RCR and MCCM 37
CHAPTER 7: FINAL REMARKS 40
7.1. Main Conclusions 40
7.2. Practical Recommendations 40
7.3. Further Development 41
7.4. Limitations of the Current Study 41
ACKNOWLEDGEMENT 43
APPENDICES 44
Appendix 1 45
Appendix 2 54
Appendix 3 63
Appendix 4 76
Appendix 5 88
Appendix 6 101
Appendix 7 106
Appendix 8 113
Appendix 9 123
REFERENCES 135

LIST OF ABBREVIATIONS

Abbreviation	Explanation of Abbreviation
3DOF	Three Degrees of Freedom
6DOF	Six Degrees of Freedom (three linear and three rotational axes)
AMR	Axis-Matched Response
CNSS	Cross-Node Sample Synchronization
FPGA	Field-Programmable Gate Array
I²S	Inter-IC Sound
IMU	Inertial Measurement Unit
LVDS	Low-Voltage Differential Signaling
MCCM	Multiaxial Component Coherence Metric
MTRIF	Multidimensional Time-Reversal Impact Focusing
POI	Point of Interest
RCM	Response-Comparison Metric
RCR	Response Coherence Ratio
RMS	Root Mean Square
SHM	Structural Health Monitoring
SPI	Serial Peripheral Interface
TR	Time Reversal
USB	Universal Serial Bus

CHAPTER 1: OVERVIEW

1.1. Introduction

Structural joint diagnostics in SHM are frequently limited by incomplete observability when single-axis sensing and excitation are employed. Because joint degradation can be axis-selective, early-stage damage may manifest along specific translational components while remaining weakly expressed or undetected along others. Multiaxial sensing alone is insufficient when excitation remains effectively one-dimensional, as it does not reliably stimulate the full directional response field around the joint. Simply increasing impact energy is not a viable alternative, since it may introduce nonlinear effects, reduce repeatability, and overstress the joint interface.

To overcome these limitations, this thesis develops a diagnostic framework that shifts the focus toward controlled multidimensional joint assessment. The framework begins by acquiring three Axis-Matched Response (AMR) pairs from 3DOF sensors mounted on opposite sides of the joint. To ensure that these AMR components are obtained under controlled multidimensional excitation conditions, Multidimensional Time-Reversal Impact Focusing (MTRIF) is used to synthesize a virtual impact point at the Near-sensor location, producing triaxial linear excitation. This multidimensional interaction is supported by Cross-Node Sample Synchronization (CNSS), which maintains the sample-level temporal consistency required for waveform-level comparison. The framework then uses the Response Coherence Ratio (RCR) to evaluate the pointwise coherence of each AMR pair. Finally, the three RCR values are fused into the Multiaxial Component Coherence Metric (MCCM), providing a scalar indicator that reduces axis-dependent dispersion and supports interpretation of the joint structural condition.

1.2. State of the Art

This section critically reviews structural-joint SHM methods relevant to localized wave-based and vibration-based diagnostics. The review concentrates on active diagnostic approaches in which excitation is introduced into the structure and the measured response is used to assess degradation-related changes at the monitored joint. Global modal monitoring methods and general condition-monitoring systems are considered only as contextual background where they help clarify the limitations of localized joint diagnostics. The literature search was conducted using the Scopus and Web of Science databases with search terms including combinations of “structural joint,” “bolted joint monitoring,” “time reversal,” “structural health monitoring,” “multiaxial sensing,” “waveform comparison,” and “vibration-based diagnostics.” The search was supplemented by forward and backward citation tracking from key references.

The reviewed literature was selected according to three inclusion criteria. First, the study had to be relevant to structural joints, including bolted, bonded, riveted, composite, lap-joint, or similar connection regions. Second, the method had to involve an active wave- or vibration-based diagnostic scheme, where excitation is introduced into the structure and the response is analyzed after interaction with the monitored joint. Third, the diagnostic information had to be related to degradation-induced changes in the local dynamic behavior of the monitored joint, including stiffness, coupling, wave propagation, or response transfer characteristics.

Time-Reversal (TR) studies are considered as a separate group because TR focusing is one of the enabling principles of the proposed framework; therefore, selected works beyond

structural-joint SHM are included where they provide methodological background for controlled replay, focusing, or multi-emitter excitation.

The selected studies were analyzed according to the following methodological criteria:

1. Cross-joint response acquisition - whether responses are measured on both sides of the structural joint, allowing degradation to be evaluated through changes in dynamic coupling between the connected structural elements.
2. Excitation directional diversity - whether excitation activates only one dominant direction or propagation path or provides controlled excitation diversity capable of stimulating several directional response components near the joint.
3. Sensing dimensionality and multichannel interpretation - whether the response is measured using single-axis or multiaxial sensing, and whether multiple response components are interpreted independently or fused into a combined diagnostic indicator.
4. Cross-joint waveform comparison- whether the method compares full waveform responses measured on opposite sides of the joint, rather than relying only on scalar energy, modal, impedance, or spectral indicators.
5. Time-Reversal axis-specific excitation - whether TR replay is used as a general focusing procedure, or whether separate axis-specific replay conditions are formed to control excitation of the receiving point along the measured response axes.
6. Distributed acquisition and synchronization - whether the sensing architecture uses centralized acquisition, short-range analog wiring, or distributed digital nodes, and whether synchronization is explicitly maintained at the sample level.

These criteria are not used to rank the reviewed studies by general SHM performance. They are used to identify which methodological requirements are already addressed in the literature and which remain insufficiently integrated for localized multidimensional structural-joint diagnostics. The following subsections discuss the reviewed works against these criteria.

1.2.1. Localized Joint Diagnostic Approaches

Frequency-response, guided-wave, and impedance-based approaches constitute the main body of localized structural-joint diagnostics. Frequency-response and transfer-based methods evaluate joint degradation through changes in dynamic characteristics between excitation and response locations. Tol and Özgüven [1] demonstrated that bolted-joint loosening modifies local transfer characteristics and vibration-response behavior, while related frequency-response comparison and cross-signature approaches were investigated in [2]. Guided-wave and Lamb-wave methods provide stronger localization capability because they are sensitive to wave interaction with joint degradation. Such approaches were applied to composite bolted joints, bolted-joint degradation, active piezoelectric sensing, and diffuse-wave or guided-wave monitoring of loosening and degradation [3–7].

Electromechanical impedance methods estimate joint condition through changes in local electromechanical coupling between piezoelectric transducers and the monitored structure [8–11]. These approaches provide high local sensitivity to stiffness and coupling variation near the joint. However, when assessed against the criteria defined above, these methods typically rely on scalar indicators, limited propagation paths, or directionally constrained actuator–receiver configurations. Their principal limitation is therefore not insufficient damage sensitivity per se; rather, it is the incomplete integration of cross-joint multiaxial acquisition, controlled excitation diversity, and waveform-level Near/Far response comparison. For example, while guided-wave methods [3,4] can detect bolt loosening through changes in wave propagation, they typically evaluate a single propagation path and do not capture the full three-dimensional response of the joint region. Similarly, impedance-based methods [8–10] provide high local sensitivity but

measure changes in electromechanical coupling at a single transducer location without cross-joint response comparison.

1.2.2. Response Comparison and Multiaxial Observability

Several studies show that degradation-sensitive information can be extracted by comparing dynamic responses measured at different structural locations [1,2,6]. Such approaches reduce dependence on detailed analytical models, relying instead on experimentally observed changes in response induced by degradation. Earlier studies associated with the present thesis [12–15] investigated localized response-comparison strategies using paired multiaxial response acquisition near structural joints. These studies demonstrated that degradation-sensitive behavior may appear differently across measurement directions depending on joint geometry, wave propagation paths, and excitation conditions.

Multiaxial sensing increases the directional information available from the structure, and six-degree-of-freedom and multichannel sensing concepts have been investigated for structural monitoring applications [16,17]. However, multiaxial sensing alone does not guarantee complete observability of the degradation state. If excitation remains effectively direction-limited, some response components may be weakly activated, and degradation-sensitive changes may remain hidden or unstable in individual channels. The key methodological issue is therefore not merely whether multiple response components are measured, but whether they are measured on both sides of the joint under excitation conditions that activate the relevant directional response field.

1.2.3. Time-Reversal Methods and Axis-Specific Excitation Control

Time-Reversal (TR) methods provide a mechanism for wavefield refocusing based on reciprocity [18]. By replaying time-reversed responses through the original propagation paths, wave energy can be concentrated near a selected point of interest. In the context of this thesis, the key question is not merely whether TR focusing is applied, but whether replay conditions are formed in an axis-specific manner such that the receiving point is excited along the measured response axes.

TR techniques have been applied to structural-condition assessment and joint diagnostics in several studies [19–25]. These studies demonstrate that TR replay can improve localization and sensitivity to joint-related changes. However, most reported implementations remain limited to excitation directions, constrained propagation paths, or single-component response evaluation. They generally do not employ TR replay to form axis-specific excitation conditions combined with synchronized multiaxial Near/Far waveform comparison across the joint. For instance, Du et al. [20,23] demonstrated bolt-preload monitoring using virtual time-reversal focusing, but the excitation and sensing remained confined to a single propagation direction. Wang and Song [24] combined vibro-acoustic modulation with time reversal for bolt loosening detection, yet the method evaluated only a single modulation index rather than multiaxial waveform coherence.

Earlier studies by the author and collaborators [26–29] investigated multi-emitter TR focusing in acoustical systems operating in attenuative propagation environments. These studies are not treated here as structural-joint diagnostic works; rather, they serve as methodological precursors demonstrating that coordinated replay from multiple emitters can concentrate wave energy near a selected spatial location. This principle supports the transition toward controlled axis-specific and multidirectional excitation in localized structural-joint diagnostics.

1.2.4. Distributed Acquisition and Synchronization

Distributed sensing architectures are becoming increasingly relevant for practical SHM systems [16,30]. However, many waveform-sensitive methods, including TR replay and direct waveform comparison, have been demonstrated in centralized laboratory configurations in which excitation and acquisition share a common timing domain. In such configurations, synchronization is implicitly ensured by common acquisition hardware or by short-range analog sensor wiring.

This assumption becomes problematic when sensing nodes are spatially distributed and digitize signals independently. Independent sampling clocks introduce systematic offset and thermal drift. For scalar or slowly varying indicators, such timing errors may be less critical. For waveform-level comparison, TR replay, and pointwise coherence evaluation, however, timing inconsistency directly affects waveform shape, phase relations, replay consistency, and interchannel comparability. The synchronization requirements become particularly stringent when TR focusing is used for controlled axis-specific excitation, because timing errors reduce the quality and repeatability of the focused response. Most existing TR-based SHM studies either assume ideal synchronization or operate in centralized configurations where this assumption is implicitly satisfied.

Synchronization-related studies associated with the present work [31–33] investigated timing stability, temporal reconstruction, and sample-consistency maintenance in distributed multichannel acquisition systems. These studies provide the technical basis for maintaining waveform-level consistency when excitation and sensing nodes are separated.

1.2.5. Research Gap

The reviewed literature demonstrates substantial progress in localized structural-joint diagnostics. Existing studies provide damage-sensitive methods based on frequency-response variation, guided waves, impedance changes, response comparison, TR focusing, multiaxial sensing, and distributed acquisition.

However, these methodological elements have predominantly been investigated in isolation. The reviewed works do not sufficiently integrate controlled axis-specific multidirectional excitation, paired cross-joint multiaxial response acquisition, waveform-level Near/Far response comparison, sample-level synchronization, and fused multichannel interpretation within a single diagnostic chain.

This limitation defines the research gap addressed by the present thesis. To bridge this gap, the proposed framework integrates multidirectional Time-Reversal excitation focusing, paired Near/Far 3DOF sensing, synchronized waveform-level response comparison, per-axis coherence evaluation, and fused multichannel interpretation into a unified methodology for localized structural-joint assessment.

1.3. Aim of Research

The aim of this research is to develop and experimentally validate a multidimensional methodology for structural joint integrity assessment that integrates controlled axis-specific excitation, synchronized cross-joint multiaxial sensing, and waveform-level coherence evaluation.

The proposed approach uses Multidimensional Time-Reversal Impact Focusing (MTRIF) to synthesize an axis-specific virtual impact at the Near-sensor location using spatially distributed actuators. The structural condition of the joint is evaluated through three Axis-Matched Response (AMR) pairs measured by Near and Far 3DOF sensors mounted on opposite sides of

the joint. Per-axis coherence is quantified using the Response Coherence Ratio (RCR), and the resulting values are fused into the Multiaxial Component Coherence Metric (MCCM).

1.4. Main Statement

The research hypothesis of this thesis was delineated as follows:

1. Structural joint degradation can be more completely characterized through multiaxial response analysis of axis-matched response pairs (AMR) measured on opposite sides of the joint than through single-point, unidirectional response evaluation.
2. Physically meaningful AMR pair analysis requires a controlled multidimensional response field in the analyzed joint region, which can be synthesized by Multidimensional Time-Reversal Impact Focusing (MTRIF).
3. Reliable implementation of the AMR–MTRIF structural joint assessment methodology is not possible without precise synchronization between excitation and sensing nodes, which is achieved in this thesis by Cross-Node Sample Synchronization (CNSS).

1.5. Scientific Novelty

1. The novelty lies in the formation of a controlled multiaxial response field in the analyzed joint region by means of Multidimensional Time-Reversal Impact Focusing (MTRIF).
2. A new approach has been developed and validated for the per-axis evaluation of three directionally specific Axis-Matched Response (AMR) pairs within a common MTRIF-focused response region.
3. A novel integrated methodological framework has been formulated, developed, and validated for multidimensional structural joint diagnostics by combining MTRIF, AMR, and Cross-Node Sample Synchronization (CNSS), where CNSS is treated as the key enabling component required for reliable framework operation.

1.6. Research Objectives

To achieve the stated research aim, the following objectives are established:

1. To develop a synchronized hardware–software platform implementing Cross-Node Sample Synchronization (CNSS) to ensure continuous sample-level alignment between excitation and sensing nodes under temporal and thermal variations.
2. To implement Multidimensional Time-Reversal Impact Focusing (MTRIF) using a multi-actuator configuration in order to synthesize an axis-specific virtual impact at the Near-sensor location.
3. To establish a paired cross-joint 3DOF sensing scheme using Near and Far sensors mounted on opposite sides of the joint and to form three Axis-Matched Response (AMR) pairs from matched linear acceleration components.
4. To develop a per-axis waveform-level coherence evaluation procedure based on the Response Coherence Ratio (RCR) for the three AMR pairs under progressive degradation.

5. To formulate the Multiaxial Component Coherence Metric (MCCM) as a fused scalar indicator combining the three per-axis RCR values to reduce axis-dependent dispersion and improve diagnostic interpretability.
6. To experimentally validate the integrated framework on a baseline structural joint under progressive degradation conditions and to relate the final methodology to supporting experimental evidence reported in the appended publications.

1.7. Structure of the Thesis

The thesis consists of seven chapters. Chapter 1 outlines the problem of structural joint diagnostics, reviews the current literature, and defines the research aim, main statements, scientific novelty, and objectives. Chapter 2 defines the methodological scope, including the 3DOF sensing requirements, the MTRIF concept, the CNSS rationale, and the formal definitions of AMR, RCR, and MCCM. Chapter 3 describes the hardware–software platform, including the system architecture, excitation subsystem, sensing chain, and synchronization implementation. Chapter 4 presents the experimental setup and data-collection workflow, including sensor and actuator placement, degradation stages, and dataset composition. Chapter 5 details the signal-processing and metric-calculation procedures, focusing on triaxial RCR evaluation and MCCM fusion. Chapter 6 presents the metric-evaluation results, including per-axis RCR trends and fused MCCM behavior across degradation stages. Chapter 7 summarizes the findings, provides practical recommendations, and outlines directions for further development.

The publications forming the basis of the thesis are listed in Section 1.8, while the main chapters synthesize their methodological contributions into a unified diagnostic framework.

1.8. Publications and Scientific Dissemination

This thesis is based on eight scientific publications [12–15,27,31–33] and one granted patent. The appended works do not represent independent or unrelated studies; rather, they document the progressive development of the methodological and engineering components synthesized in this thesis into a unified framework for localized structural-joint diagnostics.

The research trajectory began with response-comparison methods for structural joints. The work on coaxial acceleration correlation for structural-joint quality assessment [12] introduced the principle of comparing vibration responses measured in three spatial directions using coaxially oriented 3D accelerometers placed at different parts of a structural joint. The related non-model vibration analysis study [13] supported the use of experimentally observed response changes rather than detailed analytical models as the basis for structural-joint assessment. These publications established the initial methodological direction developed further in Chapter 2 as paired Near/Far response acquisition and in Chapter 5 as waveform-level metric evaluation.

The next stage extended this concept toward multiaxial structural-joint diagnostics under degradation. The study on non-destructive damage detection by coaxial correlation in 6D space [14] presented paired multiaxial sensing on opposite sides of a structural joint, synchronized excitation–response acquisition, repeated measurements, averaging, and similarity-based evaluation for monitoring degradation. The timber-joint study [15] further demonstrated that response comparison between sensors placed on different sides of a joint can be used to assess degradation in timber structural connections. Together, these publications demonstrated that degradation-sensitive response behavior may differ across measurement directions, thereby

supporting the need for per-axis evaluation and fused multichannel interpretation. In this thesis, these earlier concepts are formalized as Axis-Matched Response (AMR) pairs, Response Coherence Ratio (RCR), and Multiaxial Component Coherence Metric (MCCM), described in Chapters 2 and 5 and evaluated in Chapter 6.

The same experimental program also revealed the engineering requirements for reliable cross-joint comparison. The early response-comparison studies showed that correlation-based interpretation depends on repeatable excitation, comparable sensor placement, stable acquisition timing, and the possibility of repeated excitation with averaging. In [14] and [15], this led to practical synchronization of excitation start with the acquisition frame and to repeated measurement workflows. However, these solutions remained tied to specific experimental configurations and did not yet provide a generalized synchronization concept applicable to distributed digital sensing nodes, long cable runs, timing drift, or temperature-dependent acquisition instability.

The synchronization-related publications [31–33] advanced this engineering requirement further. The study on thermal stability of a multi-channel precise time-tagging system [31], the study on multi-channel synchronization for picosecond time-tagging [32], and the work on compensation of time-interval accuracy error [33] investigated timing stability, channel synchronization, and compensation of clock-related errors. In this thesis, these results are used to support the Cross-Node Sample Synchronization (CNSS) concept described in Chapters 2 and 3. CNSS generalizes the synchronization requirement from start-of-frame alignment toward continuous sample-level consistency, which is required for waveform-level Near/Far comparison, Time-Reversal replay, and pointwise RCR evaluation in Chapter 5.

The Time-Reversal component of the framework evolved from earlier work on controlled replay and focusing. The study on nonlinear land-mine detection using wide-bandwidth time-reversal techniques [27] is not treated in this thesis as a structural-joint diagnostic validation case. Instead, it provides methodological background for controlled time-reversed replay, focusing, and multi-emitter excitation. This experience is adapted in Chapter 2 for the formulation of Multidimensional Time-Reversal Impact Focusing (MTRIF), where spatially distributed actuators are used to synthesize an axis-specific virtual impact at the Near-sensor location.

The granted patent on non-destructive testing of building structures complements the scientific publications by documenting the system-level concept of integrated structural assessment. In the context of this thesis, it supports the practical implementation perspective of the hardware–software framework described in Chapter 3 and the overall integration logic introduced in Chapter 1.

Together, the appended publications document the transition from localized response comparison toward a synchronized multidimensional diagnostic methodology integrating MTRIF, AMR, CNSS, and multiaxial coherence evaluation into a unified structural-joint assessment framework.

CHAPTER 2: METHODOLOGICAL SCOPE AND PREREQUISITES

2.1. Measured Quantities and Scale Treatment

The measured quantities are linear accelerations expressed in m/s². In this methodology, three linear-acceleration components are recorded on the Near side and matched with three corresponding components on the Far side to form three AMR pairs.

Sensor outputs are acquired as 16-bit digital values. Conversion to SI units is not required for the proposed diagnostic metrics, since the evaluation is based on normalized waveform comparison. Near and Far signals forming each AMR pair are synchronized and normalized prior to RCR computation. Consequently, RCR and MCCM are treated as scale-independent coherence metrics derived from normalized acceleration data rather than absolute-amplitude measures.

The time axis in all plots is presented in milliseconds, while synchronization and signal comparisons are executed within the reconstructed common master clock domain.

2.2. Experimental Objects

Methodological validation was performed on structural joints encompassing various materials, connection types, and degradation scenarios. The research program included both timber and steel joints.

The experimental objects served two functions:

Supporting the development of individual methodological components reported in the appended publications [12–15].

Providing a baseline case for the final validation of the integrated framework.

Consistent with the thesis format, the final methodology is validated on a baseline structural joint, while earlier experimental objects provide complementary evidence for specific components. Intermediate validation cases did not always employ the full integrated configuration but were essential for developing the underlying framework.

2.3. Sensor Configuration and Positioning Requirements

The measurement setup employs 3DOF accelerometers mounted on opposite sides of the structural joint (Figure 2.1). Each sensor acquires three orthogonal linear-acceleration components X, Y, Z. Matching these Near-side components $X_{Near}, Y_{Near}, Z_{Near}$ with the corresponding Far-side axes $X_{Far}, Y_{Far}, Z_{Far}$ forms three AMR pairs.

This configuration enables the implementation of MTRIF by defining the Near-sensor location as the virtual impact point. The resulting synchronized data provide the basis for per-axis RCR estimation and final MCCM fusion. The Near sensor captures the reference excitation state, while the Far sensor records the response transmitted through the joint interface.

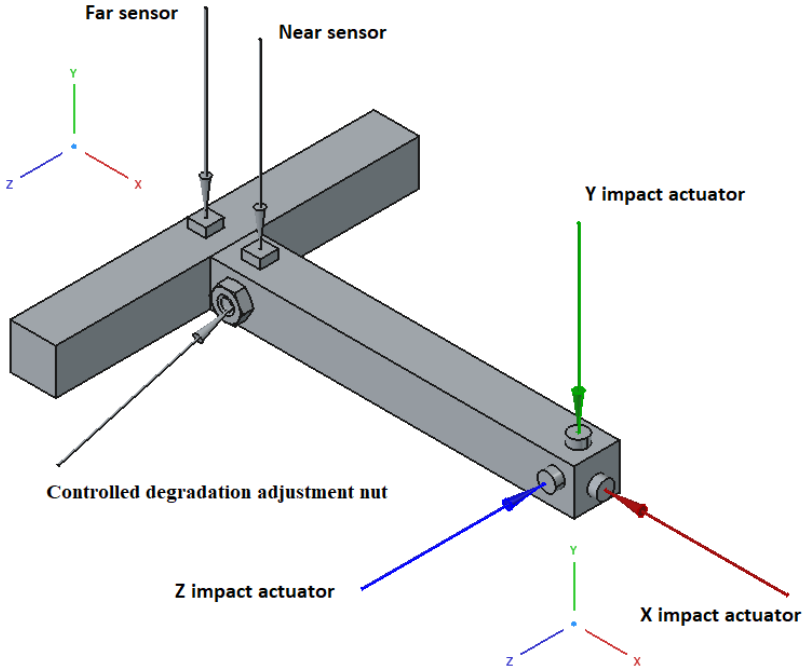


Fig. 2.1. Minimum sensor configuration and measurement geometry.

2.3.1. Virtual Coaxial Alignment Requirement

This requirement, termed virtual coaxial alignment, ensures that the matched axes of the Near and Far sensors are geometrically collinear and directionally consistent (Figure 2.1). For valid AMR formation, alignment must be maintained between the corresponding linear-acceleration axes X, Y, Z of the two sensors.

In this framework, the Near sensor is placed on the virtual impact side established by MTRIF, while the Far sensor captures the response transmitted through the joint. In baseline implementation, alignment was achieved through precise physical mounting (detailed in Chapter 4). While residual misalignment could be corrected via coordinate frame transformation, this approach is treated as an extension and is discussed only in Chapter 7.

2.3.2. Effect on Waveform Comparability (RCR)

Waveform comparability within an AMR pair requires the spacing between Near and Far measurement points along a matched axis to be less than one-quarter of the shortest relevant wavelength $\lambda/4$. Violation of this condition increases phase mismatch, thereby reducing the reliability of pointwise coherence evaluation and the robustness of the RCR estimate (Section 2.9).

Figure 2.2 illustrates this effect for three normalized spacing conditions: 0, $\lambda/4$ and $\lambda/3$. As spacing increases, waveform overlap decreases, causing a corresponding drop in RCR. In the illustrated case, the $\lambda/4$ condition retains over 50 % of the reference metric level, whereas the $\lambda/3$ condition reduces it by more than a factor of two relative to the zero-shift baseline. This reduction represents a critical loss of diagnostic sensitivity for the RCR methodology.

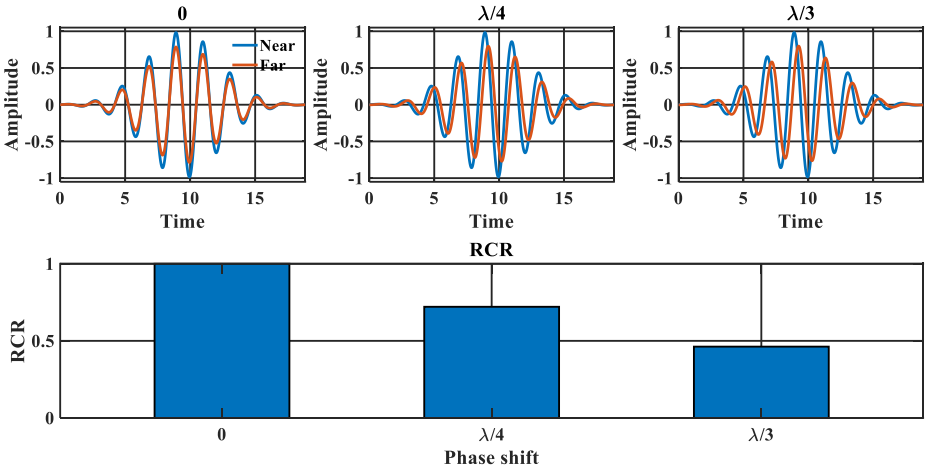


Fig. 2.2. Effect of phase shift on RCR.

2.3.3. Effect on Time-Reversal Defocusing

The λ/4 criterion also governs the spatial extent of the focal spot produced by MTRIF. Focused energy remains concentrated within a region of approximately λ/4 around the Near-sensor location. If the Far sensor is positioned beyond this focal region, it records a defocused, lower-amplitude signal that does not represent the intended virtual impact response.

The λ/4 condition is therefore critical for maintaining the physical validity of the Near/Far comparison (Figure 2.3). While the Near sensor captures the reference focused state, the Far sensor must remain within the focal zone to record the corresponding transmitted response. Exceeding this spacing threshold leads to a loss of both RCR robustness and physical representativeness of the AMR pairs.

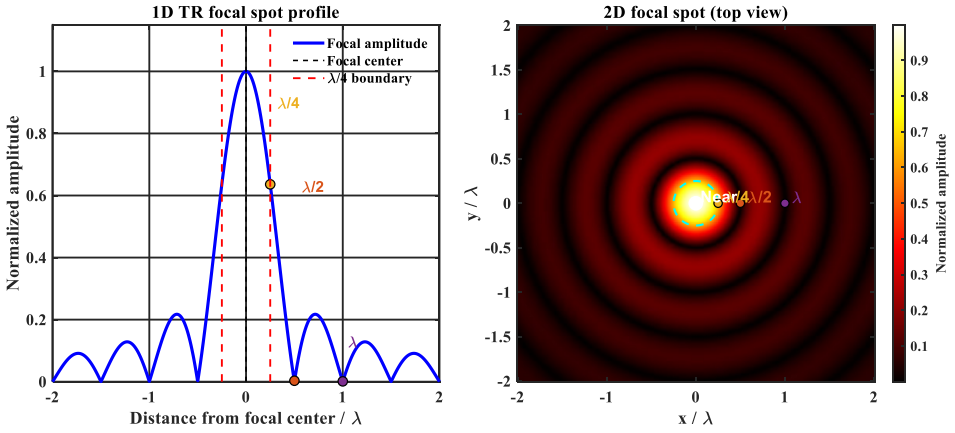


Fig. 2.3. TR focal spot and defocusing with increasing distance from the focus.

2.3.4. Practical Bandwidth Criterion for Sensor Spacing

The maximum permissible distance between Near and Far measurement points is constrained by the highest usable frequency f_{max} in the signal. This frequency is determined by the Nyquist limit, actuator bandwidth, structural dynamics, and the system noise floor.

In this study, signal components remain observable up to 9 kHz (Figure 2.4). The maximum admissible spacing d_{max} is defined by the quarter-wavelength criterion:

$$d_{\max} \approx \frac{\lambda_{\min}}{4} = \frac{c_p(f_{\max})}{4f_{\max}} \tag{2.1}$$

Variables in Eq. (2.1) are defined as follows: λ_{min} is the minimum wavelength at f_{max} $c_p(f_{max})$ is the flexural-wave phase velocity and f_{max} is the upper frequency limit.

For the HEA 100 steel beam, the phase velocity at 9 kHz is 2.7–3.4 km/s, resulting in a $\lambda/4$ limit of 75–96 mm. The experimental Near/Far spacing was approximately 30 mm (Figure 4.2a), which satisfies the criterion without additional bandwidth restrictions. If larger spacing is required, f_{max} must be reduced via zero-phase filtering to maintain wavelength compatibility with the sensor positions.

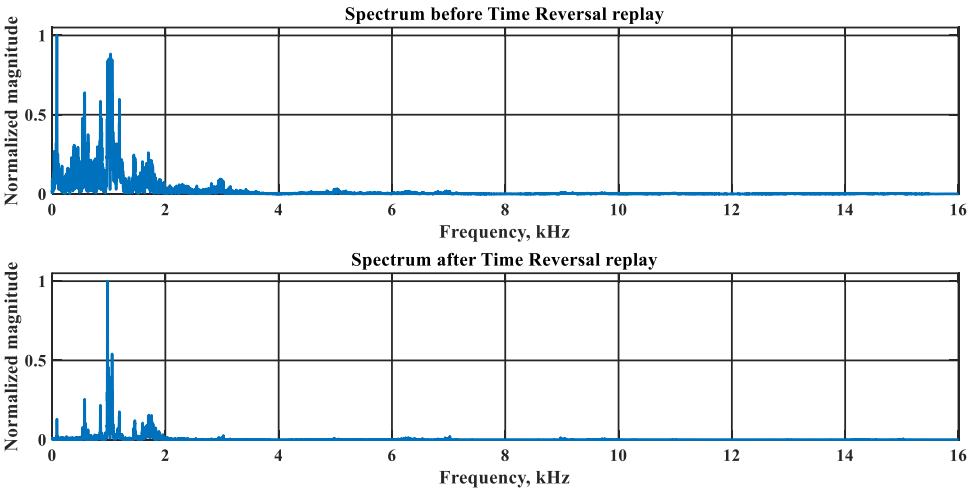


Fig. 2.4. Measured response spectra before and after Time-Reversal replay.

2.4. Actuator Configuration and Positioning Requirements

The actuator configuration must provide diverse excitation paths to facilitate multiaxial activation at the target region. Ideally, actuators are arranged to excite the principal directions of structural response independently. This independence is enhanced by increasing the number of actuators or introducing controlled asymmetry through off-center placement to stimulate complex wavefields.

The MTRIF framework does not require pure single-axis excitation at individual actuator locations. Instead, it relies on distinct transfer paths to ensure that time-reversed wavefields converge at the Near-sensor location, producing a focused multiaxial response. This multidimensional focus is essential for stimulating all three orthogonal axes represented in the AMR pairs.

In this study, a three-actuator configuration was implemented as a baseline solution. This arrangement facilitates both axis-selective sequential replay and multicomponent response activation. The role of the actuator configuration is to provide a sufficient basis for

multidimensional focusing at the Near location, enabling robust RCR estimation and MCCM fusion. The practical realization of this three-actuator setup is detailed in Figure 4.2b.

2.5. Degradation Emulation

Progressive joint degradation is defined in this thesis as a controlled reduction or modification of the mechanical coupling and stiffness of the investigated connection. In the appended publications, degradation-sensitive behavior was investigated under different structural and material scenarios, including direction-dependent response changes, selective fastener removal, bolt-torque variation, and measurements performed under varying static loading conditions. These studies provided complementary evidence that joint condition changes may affect different response axes in different ways.

For the integrated framework developed in this thesis, degradation emulation is used to generate repeatable structural states with progressively altered transmission properties across the joint. The purpose of this sequence is not to reproduce every possible real damage mechanism, but to provide controlled joint-integrity states for evaluating whether the MTRIF–AMR diagnostic cycle and multiaxial Near/Far comparison remain sensitive to progressive changes in joint condition.

In the baseline validation experiment, this concept was implemented by controlled reduction of bolt tightening torque (Figure 4.2c). The specific degradation sequence is detailed in Section 4.1.3 and Chapter 4.

2.6. Time-Reversal Impact Focusing Principles

Time Reversal (TR) is a wavefield refocusing technique grounded in the principle of reciprocity. Following [18], time reversal is equivalent to phase conjugation in the frequency domain. For a propagated signal,

$$Y(\omega) = H(\omega)S(\omega) \tag{2.2}$$

time reversal gives

$$Y_{TR}(\omega) = Y^{*}(\omega), \tag{2.3}$$

and the refocused field becomes

$$Z(\omega) = H(\omega)\, Y^{*}(\omega) = H(\omega)\, H^{*}(\omega)\, S^{*}(\omega) = |H(\omega)|^{2}\, S^{*}(\omega), \tag{2.4}$$

where $Y(\omega)$ is the received signal spectrum, $S(\omega)$ is the excitation spectrum, $H(\omega)$ is the transfer function of the structure, $Z(\omega)$ is the refocused field, the superscript (*) denotes complex conjugation and ω represents angular frequency.

Within this framework, TR serves as a mechanism for the virtual relocation of excitation from a physical actuator to a remote target position. By replaying time-reversed responses, injected energy is spatially localized and focused at the target location.

For broadband mechanical impacts, the structure selectively transmits frequency components compatible with its dynamic properties. Re-emitting the time-reversed response from the actuator location causes wave fronts to converge at the original recording point, recreating a

focused excitation. TR therefore functions as both a virtual relocation mechanism and a physically selective focusing process.

The basic TR procedure consists of four steps:

1. Emission of a broadband impulse into the structure via an actuator (Figure 2.5a).
2. Acquisition of the response at the target sensor position (Figure 2.5b).
3. Re-emission of the time-reversed acquired signal (Figure 2.5c).
4. Acquisition of the response at the target sensor position (Figure 2.5d).

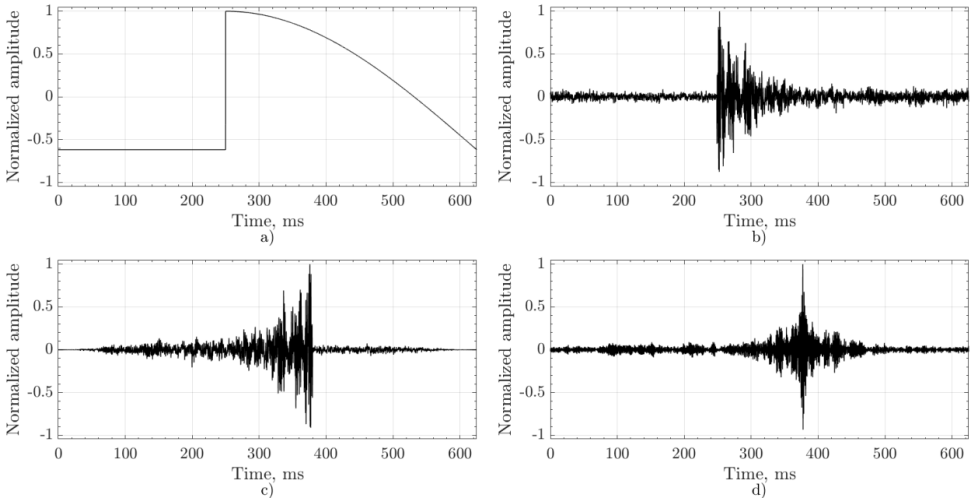


Fig. 2.5. Four-step Time-Reversal procedure in one dimension.

A representative practical application relevant to this principle was implemented by the author in earlier work on buried land-mine detection using time-reversal focusing with multiple emitters and a single receiver [27] (Fig. 2.6). In that application, coordinated replay from several actuators increased the focused energy at the target region and demonstrated that time-reversal focusing can remain effective even in strongly attenuative media. In the context of the present thesis, this earlier result is important not as a direct structural-joint experiment, but as a methodological precedent showing that coordinated multi-actuator replay can be used to concentrate energy at a selected remote location. This principle forms the conceptual basis for the multidimensional extension introduced in the following section.



Fig. 2.6. Experimental Time-Reversal land-mine detection setup.

2.7. Multidimensional Time-Reversal Impact Focusing (MTRIF)

The MTRIF framework extends the TR principle from single-component focusing to simultaneous multiaxial excitation at the point of interest. The procedure is executed as follows:

1. A broadband pulse is emitted by the actuator oriented along the X direction (Figure 2.7a), and the collinear X-component of the response is recorded at the Near sensor (Figure 2.7b).
2. A broadband pulse is emitted by the actuator oriented along the Y direction (Figure 2.7e), and the collinear Y-component of the response is recorded at the Near sensor (Figure 2.7g).
3. A broadband pulse is emitted by the actuator oriented along the Z direction (Figure 2.7i), and the collinear Z-component of the response is recorded at the Near sensor (Figure 2.7l).
4. MTRIF replay preparation: The captured collinear X, Y, and Z components are normalized and time-reversed. These waveforms are assigned as replay signals for their corresponding actuators.
5. Simultaneous replay: The three time-reversed signals are emitted simultaneously, each through the same actuator used during the characterization step. This synchronized emission generates a simultaneous triaxial focused response at the Near-sensor position (Figures 2.8e, 2.8k, and 2.8q).

To improve repeatability and suppress uncorrelated noise, each excitation signal in the MTRIF workflow was emitted multiple times. The corresponding responses recorded at the receiving sensor side were averaged before being used for replay preparation or subsequent metric evaluation.

Although only the collinear components are used to synthesize the MTRIF replay signals, the full triaxial response is recorded at each characterization step to monitor the system's behavior. As shown in Figure 2.7, structural coupling and modal mixing mean that the peak response does not always occur in the axis nominally collinear with the actuator. This can be observed for the X, Y, and Z-direction excitation cases in Figures 2.7b–d, 2.7f–h, and 2.7j–l, respectively.

For verification only, the prepared time-reversed signals were also replayed sequentially (Figures 2.8a–d, 2.8g–j, and 2.8m–p). This step is not part of the final MTRIF excitation procedure; it is used to confirm that time-reversed replay increases the contrast of the intended target components at the POI.

During simultaneous replay, the transmitted response is also recorded at the Far sensor (Figures 2.8f, 2.8l, and 2.8r). This response is not used to construct the MTRIF excitation itself, but it is later used for AMR, RCR, and MCCM evaluation. Thus, the procedure establishes the repeatable and synchronized triaxial excitation condition required for the proposed diagnostic framework.

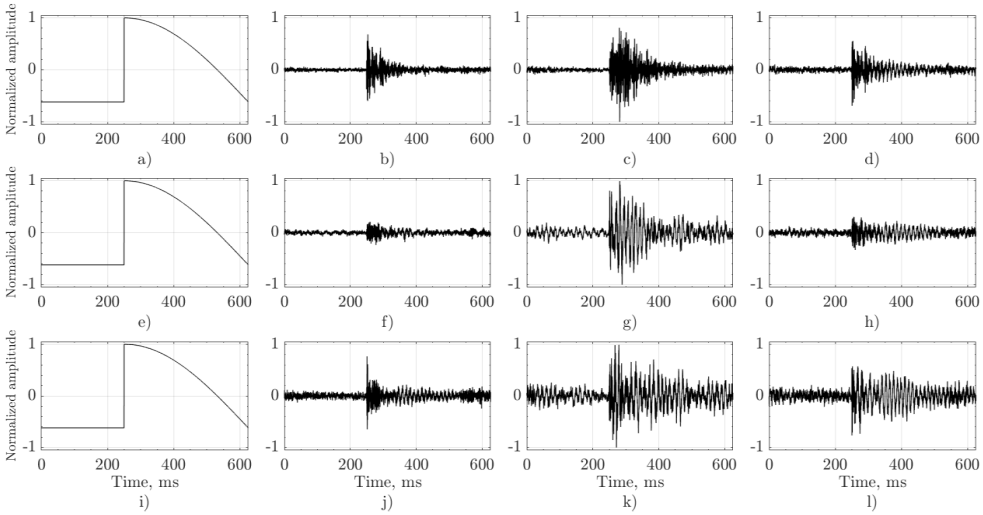


Fig. 2.7. Originally emitted signals and selected directional response signals for replay preparation.

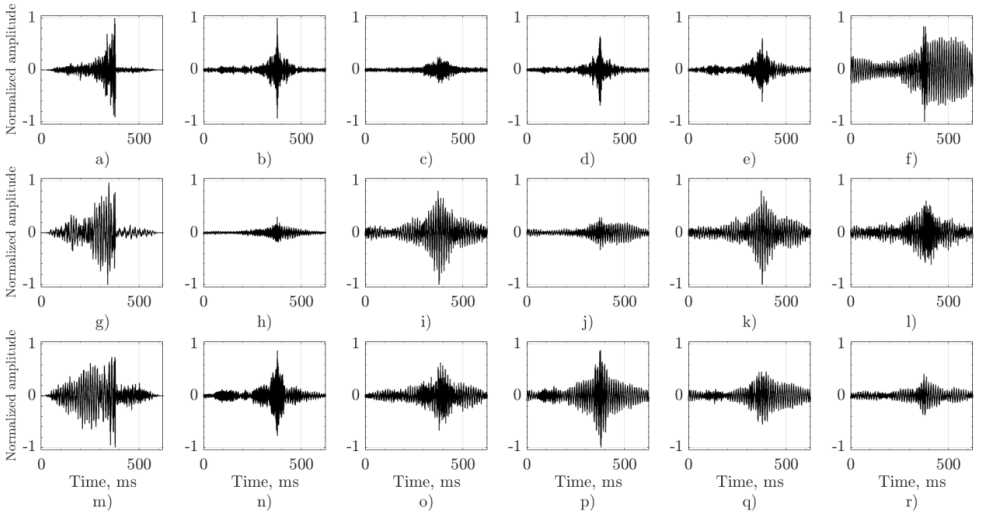


Fig. 2.8. Multiaxial response to time-reversed replay.

2.8. Time-Domain Coherence Prerequisite and CNSS Rationale

Both Time-Reversal focusing and RCR-based comparison require continuous sample-level alignment across all channels. Start-time synchronization alone is insufficient because independent clock domains diverge due to static offset and temperature-dependent drift. This divergence degrades the time consistency required for MTRIF replay and pointwise comparison.

To maintain signal comparability, the accumulated timing inconsistency Δt_{max} must satisfy the quarter-period criterion relative to the highest retained frequency f_{max}:

$$\Delta t_{\max} < \frac{1}{4 f_{\max}} \tag{2.5}$$

The variables in Eq. (2.5) are the maximum admissible accumulated timing error Δt_{max} and the highest usable frequency f_{max}. For a 32 kHz sampling rate, the Nyquist frequency is 16 kHz period $T = 62.5$ µs, yielding a Δt_{max} limit of 15.6 µs. A typical oscillator mismatch of 30 ppm over 10 s produces 300 µs of error, exceeding the acceptable threshold [31,33].

CNSS preserves a common time reference across independently clocked nodes. Figure 2.9 illustrates: (a) the signal in the master clock domain; (b) the signal in the local sensor clock domain under drift; and (c) the signal reconstructed via marker-based resampling. Recorded markers serve as timing observables to estimate mismatch and restore sample-level alignment [32,33]. Although deviations in Figure 2.9 are exaggerated for clarity, uncorrected real-world drift is sufficient to degrade phase consistency and RCR evaluation.

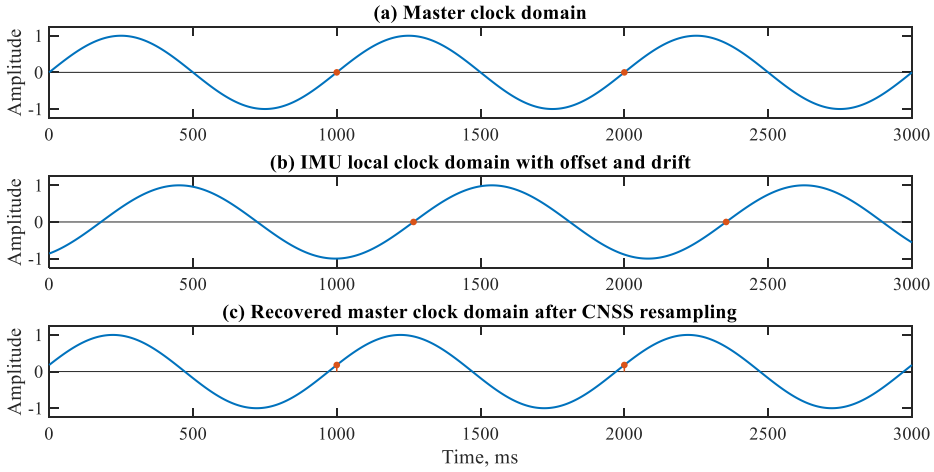


Fig. 2.9. Illustration of clock offset, drift, and marker-based recovery via CNSS.

2.9. Response Coherence Ratio (RCR)

Because the proposed methodology evaluates three AMR pairs formed by matched linear-acceleration components measured along corresponding axes on the Near and Far sides of the joint, the key challenge was to select an appropriate per-axis coherence metric [12–14]. The selected metric should be:

- invariant to absolute amplitude;

- sensitive to waveform shape and relative amplitude within corresponding AMR;
- robust to low-energy or noisy AMR pairs;

During the development of the methodology, several candidates were considered:

- Normalized Cross-Correlation RMS (NCCR);
- Pearson Correlation Coefficient;
- Cosine Similarity;
- Response Coherence Ratio (RCR).

Table 2.1.

Qualitative comparison of candidate per-axis similarity metrics used during metric selection

Metric	Amplitude Invariance	Shape Sensitivity	Noise Robustness	Notes
NCCR	✓	✓	✗ Poor on noisy axes	Fails on low-signal channels
Pearson Correlation	✓	✓	✗ Poor on noisy axes	Classical but unstable at low SNR
Cosine Similarity	✓	✗ Poor	✗ Poor on noisy axes	Unstable under partial match
RCR	✓	✓	✓ Robust	Best suited for 3DOF MCCM

A comparative evaluation of the candidate per-axis similarity metrics is presented in Table 2.1. On the basis of this evaluation, RCR was selected as the final per-axis metric because it offers the best balance among shape sensitivity, amplitude invariance, noise robustness, and practical repeatability within the AMR cross-joint evaluation framework [12–14]. Specifically, the peak-to-RMS formulation of RCR (detailed in Section 5.1) naturally attenuates noisy or weakly activated channels because random noise produces a low peak-to-RMS ratio, whereas a coherent waveform match produces a pronounced peak in the pointwise product signal. This self-weighting property makes RCR better suited than Pearson correlation or cosine similarity for applications where individual AMR pairs may have substantially different signal-to-noise ratios. A quantitative comparison of all four candidate metrics on the same baseline dataset is documented in the appended publications [12,14].

2.10. Multiaxial Component Coherence Metric (MCCM)

The MCCM is the fused scalar indicator of joint condition within the proposed framework [12,14,15]. It consolidates the three per-axis RCR values derived from the linear-acceleration AMR pairs into a single scalar metric. This fusion reduces axis-dependent dispersion and enhances the interpretability of the joint-condition assessment. The Euclidean-norm formulation was selected over alternative fusion strategies (weighted sum, geometric mean, or minimum-value approaches) because it preserves the contribution of all three axes without requiring prior knowledge of axis-specific sensitivity or weighting coefficients. The mathematical procedure for MCCM computation is detailed in Section 5.2.

CHAPTER 3: HARDWARE–SOFTWARE PLATFORM FOR DATA ACQUISITION

3.1. Purpose and Scope of the Platform

The proposed methodology requires a dedicated hardware–software platform providing the following capabilities:

- synchronized multi-actuator excitation;
- multi-channel 6DOF sensing;
- high noise immunity for remotely placed sensors;
- high-speed bidirectional data transfer between the acquisition hardware and the host computer;
- precise long-term time-domain synchronization between actuators and sensors.

Together, these requirements define the minimal functional platform structure shown in Figure 3.1 [14,27,31–33]. Its detailed architecture and subsystem organization are described in the following sections.

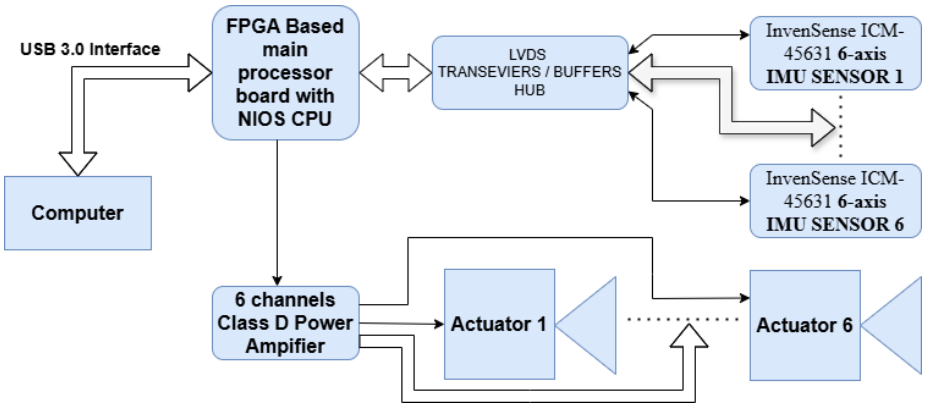


Fig. 3.1. Hardware–software platform block diagram.

3.2. System Overview and Core Architecture

The core architecture is centered on an FPGA-based main processor board (Intel Cyclone IV EP4CE22), which provides the acquisition and control functions required by the platform (Figure 3.1), including:

- timing control in the platform master clock domain;
- excitation waveform generation and control;
- acquisition and handling of SPI data streams from distributed IMU sensors;
- frame synchronization marker generation, injection, and capture;
- data framing and packaging for recording and transfer.

Sensor data are transferred through a hub of LVDS transceivers and buffers that extends the digital SPI sensor interface over long cable runs to the FPGA, providing high noise immunity and enabling remote sensor placement. Actuators are driven by a custom six-channel Class D power amplifier controlled by the FPGA unit. Communication with the host computer is

provided through a USB 3.0 interface for platform configuration, measurement control, and high-speed bidirectional dataset transfer.

3.3. Excitation Subsystem

The excitation subsystem delivers controlled mechanical input to the structure. It consists of a custom six-channel Class D power stage driving up to six vibration actuators. The amplifier is controlled via an I²S digital audio bus, enabling real-time waveform streaming from the FPGA without the need for extensive on-chip memory. The Class D topology ensures high efficiency and low heat dissipation during multi-channel operation.

The actuators are resonance-based vibration speakers attached directly to the structural member (Figure 3.2). These devices inject vibrations into the surface, using the structure itself as the radiating medium. This configuration ensures efficient mechanical coupling and compact mounting suitable for MTRIF excitation.

In the current implementation, the effective bandwidth is limited by the sensor sampling rates. For the accelerometer channels, the usable upper frequency limit is approximately 16 kHz.



Fig. 3.2. Resonance speaker used as an actuator.

3.4. Sensing, Acquisition, and Noise-Robust Data Transfer

The platform supports up to six 6DOF IMU nodes, utilizing the ICM-45631 as the primary sensor. Although the hardware provides full 6DOF acquisition (three translational and three rotational channels), the current work focuses exclusively on the three linear-acceleration channels to satisfy the 3DOF methodology requirements. The implementation uses a 32 kHz sampling rate for the accelerometer data and 8 kHz for the gyroscope data.

Data acquisition is executed via SPI and transmitted to the FPGA through LVDS extenders, supporting cable lengths up to 100 m. This configuration ensures high noise immunity for remote sensor deployment. The FPGA performs framing, buffering, and packaging of the multi-channel data stream for host computer transfer. The sensor-side architecture is shown in Figure 3.1.

3.5. Time-Reference Support and CNSS Observables

The independent clock domains of distributed sensor nodes and the master excitation controller necessitate active timing compensation. Even with a common start event, local sensor

time bases diverge from the master clock due to static offset and thermal drift, violating the requirements for MTRIF and RCR analysis [31–33].

To quantify this divergence, the platform injects periodic synchronization markers into each acquisition stream. These markers function as timing observables, captured synchronously with sensor data to estimate accumulated mismatch without modifying the local clocking of the remote nodes. During signal processing, these observables are used to reconstruct all channels into a common master clock domain, ensuring the phase consistency required for valid pointwise waveform comparison of AMR pairs.

The timing studies reported in [31–33] demonstrated picosecond-level synchronization and time-interval compensation capabilities. In the present platform, these results are used as the methodological and engineering basis for CNSS; however, such accuracy is not required for the acceleration-sensing channel considered here. The accelerometer data are acquired at 32 kHz, corresponding to a sampling interval of 31.25 μs. For the retained upper frequency of 16 kHz, the quarter-period timing criterion corresponds to a maximum admissible timing deviation of 15.6 μs, equivalent to approximately 9.0 μs RMS under a uniform-error assumption. A single reconstructed measurement therefore remains close to the admissible timing limit. To obtain a robust timing margin, repeated marker-aligned measurements are averaged, reducing the random timing component as $1/\sqrt{N}$. With four repeated measurements, the effective uncertainty is reduced to approximately 4.5 μs RMS, while the eight repeated measurements used in this work reduce it further to approximately 3.2 μs RMS. Thus, after marker-based reconstruction and averaging, the timing requirement for the present acceleration-sensing channel is satisfied with a clear margin.

3.6. Control Software and User Interface

A dedicated host-PC software suite was developed as part of this work to serve as the operational front end for the platform. The software integrates experiment control, live monitoring, and dataset management within a unified environment, ensuring seamless interaction between the user and the hardware. Key functions of the developed software include:

- Excitation Management: Waveform preparation and multi-channel assignment.
- Hardware Control: Configuration and execution of acquisition cycles.
- Data Processing: Marker-based resynchronization, frame alignment, and real-time visualization.
- Iterative Workflow: Replay signal preparation for MTRIF operation.
- Storage: Multi-channel data recording and export for post-processing.

This integrated approach enables precise experimental control and efficient data handling, directly supporting the methodology described in this thesis.

3.7. Key Specifications of the Platform

The technical characteristics of the platform are summarized in Table 3.1. These parameters define the operational limits for sensing, excitation, synchronization, and data transfer. The timing principles and accuracy margin of the CNSS approach are discussed in Section 3.5 and supported by the studies reported in [31–33].

Table 3.1.

Key platform specifications

Parameter	Specification
Sensor Nodes	Up to 6 × 6DOF IMU (ICM-45631)
Linear Acceleration ODR	32 kHz (used for 3DOF methodology)
Angular Velocity ODR	8 kHz (hardware supported)
Effective Bandwidth	Sensor-limited: ~16 kHz (acceleration)
Accelerometer Range	Programmable: ±2g to ±16g
Accelerometer Noise Density	90 µg/√Hz
Excitation Channels	6 × Class D (up to 100 W peak/channel)
Vibration Actuators	6 × Resonance vibrators (25 W rated)
Remote Sensor Link	SPI over LVDS (up to 100 m)
Host Interface	USB 3.0

CHAPTER 4: DATA COLLECTION

4.1. Baseline Object and Joint Configuration

The baseline validation employed a structural steel stand consisting of two S355 (HEA 100) beams connected by a semi-rigid bolted joint. The connection was secured with a single M16 bolt (strength class 8.8). This configuration was chosen to ensure a repeatable joint condition under progressive stiffness variation and multiaxial measurements. The experimental setup is illustrated in Figure 4.1.



Fig. 4.1. Baseline steel beam stand.



Fig. 4.2. Baseline experimental arrangement.

4.1.1. Sensor Placement

Two 3DOF sensors were mounted on opposite sides of the joint, 30 mm from the centerline on separate beam elements (Figure 4.2a). The Near sensor defines the virtual impact location for MTRIF, while the Far sensor captures the transmitted wavefield.

Sensor axes X, Y, Z were physically aligned during installation to establish the three AMR pairs required for analysis. This placement ensures the virtual coaxial alignment necessary for pointwise signal comparison without additional coordinate transformations.

4.1.2. Actuator Placement

Three resonance actuators were mounted on the Near-side beam to excite the X, Y and Z axes (Figure 4.2b). The actuators were spatially distributed to provide the transfer paths required for MTRIF. This configuration ensures multidimensional activation at the Near-sensor location (virtual impact point) without placing physical transmitters directly at the POI.

4.1.3. Degradation Method

In the baseline validation experiment, progressive joint degradation was emulated by a controlled reduction in the bolt-tightening torque using a torque wrench (Figure 4.2c). This procedure was selected as a repeatable and reversible means of modifying the mechanical coupling and stiffness of the bolted joint without altering the sensor or actuator configuration.

The torque was reduced from 175 N·m to 0 N·m across eight predefined degradation stages. Within this experiment, the torque sequence is treated as a controlled set of joint-integrity states rather than a comprehensive representation of all possible real damage mechanisms. Its purpose is to provide a consistent sequence of altered transmission properties to demonstrate the MTRIF–AMR diagnostic cycle and to evaluate the sensitivity of the axis-matched Near/Far responses to progressive joint-condition changes.

4.2. Measurement Steps

The experimental process was structured as a repeated measurement–degradation cycle. To ensure consistency across degradation states, the same MTRIF procedure was applied at each torque level without modifying the sensor or actuator placement.

The workflow was executed as follows:

1. START: The joint was set to the baseline condition, corresponding to the fully tightened state at 175 N·m.
2. MEASURE: The complete MTRIF procedure described in Section 2.7 was performed for the current joint state.
3. RECORD: The triaxial Near and Far responses obtained during the simultaneous replay phase were stored for the current state.
4. DEGRADE: The joint stiffness was reduced by decreasing the tightening torque of the M16 bolt to the next predefined level.
5. GOTO MEASURE: The measurement–degradation cycle was repeated until the fully loosened state was recorded.

The degradation sequence consisted of eight torque levels:

Stage 1: 175 N·m, baseline tightened condition;

Stage 2- Stage 8: 150 N·m, 125 N·m, 100 N·m, 75 N·m, 50 N·m, 25 N·m, 0 N·m, fully loosened condition.

Completing this loop through all eight stages yielded the final response dataset. For each stage, three linear acceleration components were recorded at both the Near and Far sensors during the simultaneous MTRIF replay.

The complete measurement–degradation sequence was repeated five times without changing the sensor and actuator configuration. Each repetition covered the same eight torque levels from 175 N·m to 0 N·m. Consequently, the repeated dataset contains:

3 channels × 2 sensors × 8 stages × 5 repetitions = 240 response signals,corresponding to:

3 AMR pairs × 8 stages × 5 repetitions = 120 AMR pairs.

This repeated dataset enables both degradation-trend evaluation and repeatability analysis through standard deviations of the per-axis RCR values and the fused MCCM.

CHAPTER 5: SIGNAL PROCESSING AND METRIC EVALUATION

This chapter details the computational procedures for transforming the synchronized Near/Far sensor responses into diagnostic indicators. While Chapter 2 established the conceptual definitions and methodological rationale for the AMR, RCR, and MCCM components, the present chapter specifies the complete processing algorithms as applied to the experimental dataset. The workflow is applied independently to each of the three linear-acceleration AMR pairs: $\mathrm{AMR_x}, \mathrm{AMR_y}, \mathrm{AMR_z}$.

In the proposed methodology, RCR and MCCM provide the per-axis evaluation and multi-axial fusion layers of the diagnostic workflow. Their functional roles remain fixed within the proposed framework, while the specific computational implementation may be adapted depending on the sensing configuration, signal characteristics, and application constraints. The computational procedures presented below are used to quantify the degradation-sensitive response of the MTRIF–AMR framework; the primary scientific novelty lies in the integrated diagnostic methodology rather than in the specific computational formulations.

5.1. Per-Axis RCR Evaluation

- DC Offset Removal: Constant components are suppressed to eliminate gravity-related offsets:

$$\mathrm{s_{dc}} = \mathrm{s} - \bar{\mathrm{s}}. \tag{5.1}$$

- Normalization: Signals in the AMR pair are scaled by their common maximum absolute amplitude A:

$$\mathrm{s_n} = \mathrm{s_{dc}}/\mathrm{A}. \tag{5.2}$$

- Band-Pass Filtering: Signals are restricted to the target frequency range:

$$\mathrm{s_{bpf}} = \mathrm{B}(\mathrm{s_n}). \tag{5.3}$$

- Pointwise Multiplication: An intermediate product signal p is generated:

$$\mathrm{p} = \mathrm{s}_{\mathrm{Near}}^{\mathrm{bpf}} \cdot \mathrm{s}_{\mathrm{Far}}^{\mathrm{bpf}}. \tag{5.4}$$

- RCR Extraction: The final scalar for the axis is the peak-to-RMS ratio of the product signal:

$$\mathrm{RCR} = \max|\mathrm{p}|\,/\mathrm{RMS}(\mathrm{p}). \tag{5.5}$$

where s is the recorded signal, $\bar{\mathrm{s}}$ is the mean signal value, $\mathrm{s_{dc}}$ is the offset-corrected signal, A is the normalization factor, $\mathrm{s_n}$ is the normalized signal, B is the band-pass operator, iss_{bpf} is the filtered signal, p is the pointwise product and RMS is the root mean square operator.

All signals are processed in the reconstructed master clock domain.

5.2. MCCM Computation

After the per-axis RCR values are calculated for the X, Y, and Z AMR pairs, they are combined into the Multiaxial Component Coherence Metric (MCCM). In the present implementation, MCCM is computed as the Euclidean norm of the three per-axis RCR components:

$$MCCM = \sqrt{RCR_x^2 + RCR_y^2 + RCR_z^2}. \tag{5.6}$$

where RCRx, RCRy, and RCRz are the Response Coherence Ratio values obtained from the corresponding X, Y, and Z AMR pairs.

The computation is performed independently for each degradation stage and, in the repeated-measurement dataset, for each measurement cycle. Thus, every torque level is represented by one MCCM value per repetition.

CHAPTER 6: METRIC EVALUATION RESULTS

This chapter presents quantitative results from five repeated measurement–degradation cycles performed across eight torque levels. Joint degradation was emulated by reducing the tightening torque from 175 N·m to 0 N·m. The repeated dataset contained 240 response signals, corresponding to 120 AMR pairs. RCR was computed independently for each axis, torque level, and repetition, and the resulting values were fused into MCCM for each degradation state.

The repeated cycles allow the monotonic degradation trend, metric repeatability, and dispersion to be evaluated. The results are presented as per-axis RCR trends, fused MCCM behavior, and standard-deviation-based stability analysis.

6.1. Per-Axis RCR Repeatability Across Five Measurement Cycles

The per-axis RCR results are shown in Fig. 6.1. All values are normalized to the baseline condition of each repetition, corresponding to 175 N·m. In all cycles, the highest RCR values occur at the baseline condition, while progressive torque reduction causes a clear decrease in coherence across all three AMR pairs.

The repeated cycles show a reproducible degradation pattern, but the X, Y, and Z components differ in slope and dispersion. This reflects anisotropic wave transmission through the joint and direction-dependent sensitivity to bolt loosening. Therefore, single-axis interpretation remains vulnerable to axis-specific variability, whereas retaining all three RCR components provides a more complete representation of the joint condition.

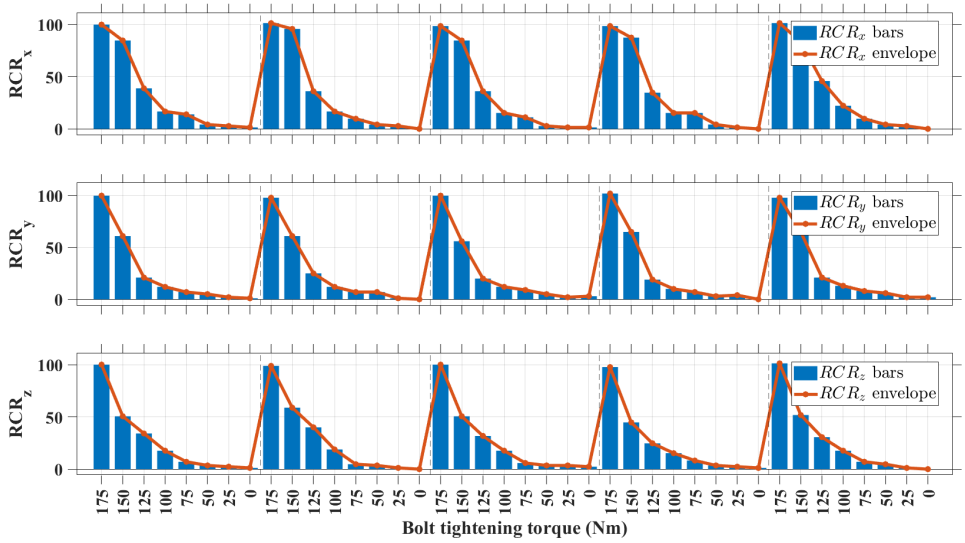


Fig. 6.1. Per-axis RCR values.

6.2. MCCM Repeatability and Degradation Trend

The fused MCCM results are shown in Fig. 6.2. All values are normalized to the initial baseline of each repetition, corresponding to 175 N·m. Compared with the individual RCR components, MCCM provides a more compact and interpretable degradation profile. In all five repeated measurement cycles, MCCM decreases consistently from the baseline condition toward the fully loosened 0 N·m condition.

The repeated MCCM trend confirms that the fused metric preserves the degradation-sensitive information contained in the three AMR pairs while reducing axis-dependent variability. The monotonic or near-monotonic decrease within each repetition supports the use of MCCM as the primary scalar indicator for joint-condition tracking. At the same time, the individual RCR components remain useful for directional interpretation and for identifying which response axes are most affected by the change in joint stiffness.

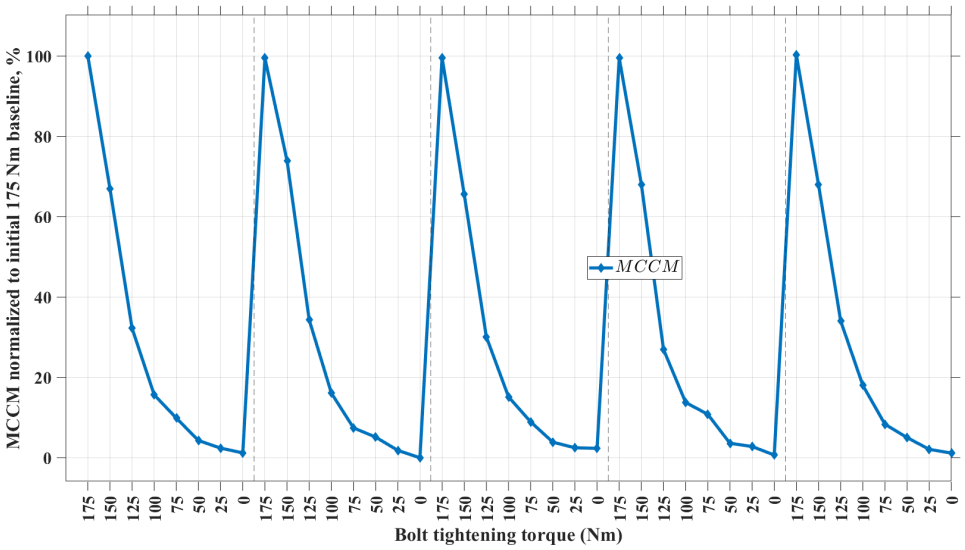


Fig. 6.2. MCCM values.

6.3. Dispersion Analysis of RCR and MCCM

The standard deviations of the per-axis RCR values across the five repetitions are shown in Figure 6.3. The dispersion is low near the fully tightened baseline condition and increases as the tightening torque is reduced. This increase is especially pronounced at low torque levels, where the joint interface becomes mechanically less constrained and more sensitive to small variations in contact state, friction, and local boundary conditions.

The standard deviation of MCCM is shown in Figure 6.4. Although the fused metric also exhibits increasing dispersion toward the loosened condition, its variability remains lower and more compact than the maximum dispersion observed among the individual RCR axes. This confirms that the MCCM fusion procedure suppresses part of the axis-dependent variability while preserving the overall degradation trend.

A direct comparison between mean per-axis dispersion, maximum per-axis dispersion, and MCCM dispersion is presented in Figure 6.5. The fused MCCM standard deviation remains below the maximum individual-axis standard deviation over the degradation sequence, demonstrating that multiaxial fusion improves the stability of the diagnostic indicator. The increase in dispersion at low torque levels should not be interpreted as a failure of the method; rather, it reflects the physically unstable contact condition of a loosened bolted joint, where small changes in interface state can produce larger changes in the measured dynamic response.

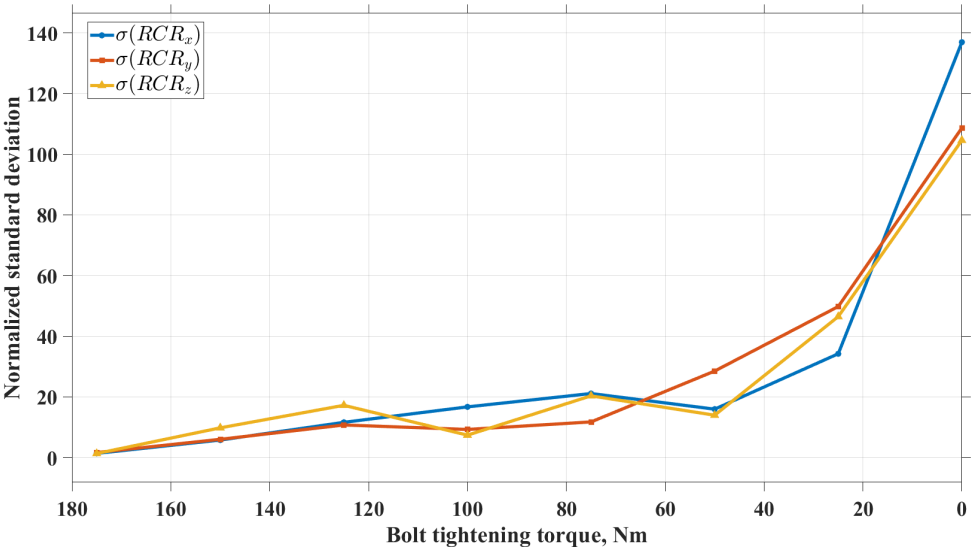


Fig. 6.3. Per-axis RCR standard deviation.

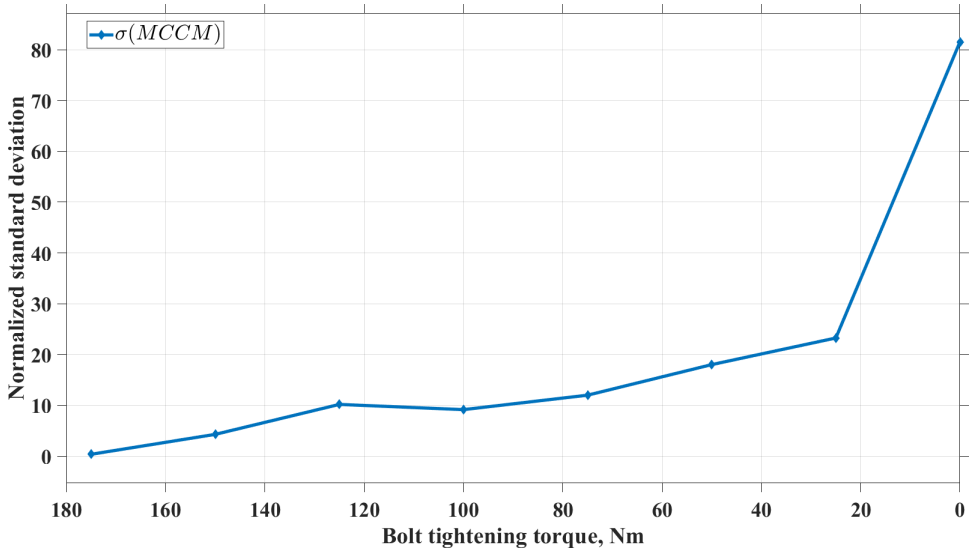


Fig. 6.4. MCCM standard deviation.

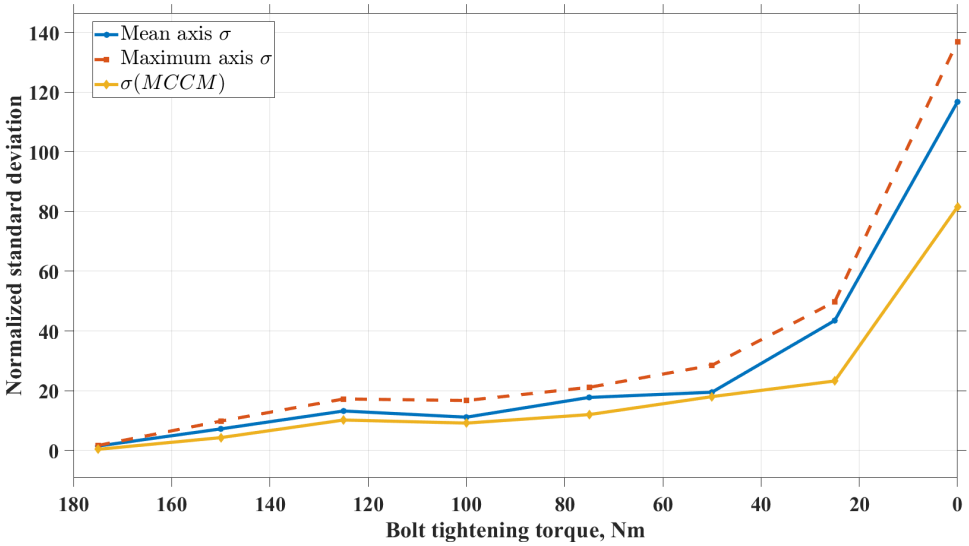


Fig. 6.5. RCR and MCCM dispersion comparison.

CHAPTER 7: FINAL REMARKS

This chapter summarizes the core findings, provides practical implementation guidelines, and outlines future development paths for the diagnostic framework.

7.1. Main Conclusions

This thesis developed and experimentally validated a multidimensional framework for the non-destructive assessment of structural joints. The results support the core premise that reliable joint diagnostics benefit substantially from a multidimensional approach encompassing both controlled excitation and multiaxial response evaluation.

1. 3DOF Sensing and AMR: The results confirm that the three linear-acceleration AMR pairs contain diagnostically relevant coherence information. In the baseline dataset, degradation-related variation was observable across all three pairs, providing a comprehensive view of joint integrity.
2. MTRIF Implementation: The principal contribution is the formulation of MTRIF, which synthesizes a multiaxial excitation condition at the Near-sensor location. This enhances the observability of degradation-related changes across multiple response components compared with conventional single-axis excitation.
3. Metric Performance: At the per-axis level, the RCR effectively quantifies waveform similarity between Near and Far responses. At the fused level, the MCCM provides a stable and interpretable indicator, suppressing axis-dependent variance and exhibiting a monotonic degradation trend. Across five repeated measurement cycles, the MCCM preserved a consistent degradation trend and showed lower dispersion than the most variable individual RCR component, supporting its use as the primary scalar indicator for joint-condition tracking.
4. Synchronization Rationale: The study demonstrates that temporal synchronization is a methodological prerequisite. Since both the MTRIF and pointwise RCR comparisons depend on continuous sample-level alignment, the CNSS principle is mandatory for maintaining a common master clock domain across independent nodes.
5. Integrated Framework: The thesis provides an experimentally grounded methodology integrating multidimensional excitation, paired 3DOF sensing, per-axis coherence evaluation, and metric fusion. This approach advances Structural Health Monitoring toward localized, repeatable, and multiaxial assessment of structural joint integrity. The limitations of the current experimental validation and their implications for generalizability are discussed in Section 7.4.

7.2. Practical Recommendations

- Sensor Alignment: Near and Far sensors must be physically aligned along their corresponding $\mathrm{X}, \mathrm{Y}, \mathrm{Z}$ axes with secure mechanical coupling. This is necessary to preserve the validity of the three linear-acceleration AMR pairs used for pointwise comparison [14].
- Excitation Configuration: Actuator placement should be determined by the required diagnostic coverage. While the three-actuator configuration along X, Y, Z axes is sufficient for triaxial linear sensitivity, alternative configurations or additional actuators may be required if complex rotational coupling is expected.

- Synchronization Continuity: Continuous sample-level alignment across excitation and sensing subsystems is mandatory. Without master-clock consistency, MTRIF focusing and RCR evaluation lose diagnostic reliability [31–33].
- Signal Averaging: Repeated excitation and averaging are recommended to suppress uncorrelated noise and stabilize RCR and MCCM values [14,15,27]. High-rate multiaxial acquisition generates substantial data streams, necessitating robust data handling and labeling.
- Diagnostic Indicators: MCCM should be utilized as the primary scalar indicator for joint condition tracking. Individual RCR values should be retained for directional diagnostic interpretation when detailed analysis of axis-specific degradation is required [12,14,15].

7.3. Further Development

Building on the findings and acknowledging the limitations discussed in Section 7.4, future work should address the following technical areas:

- Automated Axis Alignment: Implementation of orientation-aware coordinate transformations to compensate for physical sensor misalignment mathematically.
- Adaptive MTRIF: Development of real-time transfer-function estimation to optimize the virtual impact focus under varying environmental conditions.
- Decentralized Synchronization: Expansion of the CNSS protocol for large-scale sensor networks using wireless or PTP-based time distribution.
- Non-linear Feature Extraction: Integration of higher-order statistics into the MCCM fusion to improve sensitivity to micro-crack initiation.
- Edge Computing Implementation: Porting the RCR and MCCM algorithms directly to the FPGA for real-time, on-node joint integrity monitoring.

7.4. Limitations of the Current Study

The following limitations of the present work should be acknowledged to provide an accurate assessment of the framework's current state and to guide future development.

Single baseline joint configuration. The integrated framework is validated on a single structural steel joint (HEA 100 beams with one M16 bolt). While earlier experimental objects from the appended publications—including timber joints [15] and alternative steel configurations [12–14]—provide complementary evidence for individual methodological components, the full MTRIF–AMR–CNSS chain is demonstrated for a single joint geometry, material, and connection type. The extent to which the observed MCCM trends generalize to different joint types (riveted, bonded, composite), materials, numbers of fasteners, or real-world boundary conditions remains to be established through a systematic validation campaign that covers multiple joint configurations.

Degradation emulation scope. The degradation sequence consists of controlled bolt-torque reduction that emulates stiffness loss due to loosened fasteners. While this is a widely used and repeatable approach in SHM research, it represents only one mode of degradation. Real-world structural joint degradation includes fatigue cracking, corrosion, delamination, and plastic deformation, each of which modifies the joint’s dynamic behavior in different ways. The extent to which the MCCM responds to these alternative damage mechanisms—and whether the

monotonic trend observed under torque reduction is preserved under other degradation modes—requires targeted experimental investigation.

Statistical characterization scope. The present validation includes five repeated measurement cycles for the same baseline joint configuration, which enables preliminary evaluation of RCR and MCCM repeatability through standard deviations. However, these repetitions were performed on a single specimen and under controlled laboratory conditions.

Therefore, the statistical characterization remains limited with respect to specimen-to-specimen variability, alternative joint geometries, different fastener layouts, and different degradation mechanisms. Future studies should extend the repeated-cycle analysis to multiple specimens and operating conditions and should include confidence intervals and formal monotonicity testing.

Sensitivity to non-ideal conditions. The current validation was performed under controlled laboratory conditions with careful sensor alignment, stable temperature, and no external loading. The sensitivity of the framework to practical deviations—such as sensor misalignment of several degrees, partial actuator failure, environmental temperature variation during measurement, or the presence of external operational loads—has not been systematically characterized. While the $\lambda/4$ criterion (Section 2.3) provides theoretical bounds, an experimental parametric study of robustness under non-ideal conditions would significantly strengthen confidence in the framework's applicability to field deployment.

These limitations do not diminish the methodological contributions of the thesis, which lie in the formalization and initial experimental validation of the integrated MTRIF–AMR–CNSS framework. However, they define a clear agenda for the systematic validation and robustness characterization required before the methodology can be considered ready for practical deployment.

ACKNOWLEDGEMENT

I would like to express my sincere gratitude to all those who contributed to the successful completion of this research project.

First and foremost, I would like to thank my students Aleksandrs Mjakiševs, Aleksis Kurajevs, and Andrejs Macevičs, who actively participated in the experimental work and successfully defended their Master's theses. Their engagement, precision, and technical contributions were essential for the execution of key measurements presented in this thesis.

Special thanks are extended to Dmitrijs Serdjuks, the principal investigator of the Latvian Council of Science project "Method of correlation of coaxial accelerations in 6-D space for quality assessment of structural joints" ("COACCEL**"** (Nr. lzp-2020/1-0240), for his sustained support and encouragement throughout the project.

I am particularly grateful to my supervisors, Jevgenijs Barkanovs, the principal investigator of the ERDF project "An Effectiveness Improvement of Conventional Pultrusion Processes" (project ID No. 1.1.1.1/18/A/053), in which I participated during my doctoral studies, and Aleksejs Tatarinovs, whose encouragement and guidance were instrumental in my decision to resume and complete doctoral studies. Their support opened the door to research opportunities that were both challenging and inspiring.

Most importantly, I wish to thank my family for their unwavering support throughout this journey. To my wife Karina, whose encouragement and understanding kept me moving forward when I was ready to stop. And to my sons, Nikita and Matvejs, who were born during this research and who—perhaps unknowingly—allowed me the time and space to pursue it.

Finally, I am thankful to all the individuals who participated in the experiments and contributed to the progress of this work.

APPENDICES

Serdjuks D., **Kurtenoks V.**, Tatarinovs A., Mironovs V., Lapkovskis V., Buka-Vaivade K., Macevics A., Topcijs K., Vilnitis M.

Method of coaxial accelerations correlation for quality assessment of structural joints.

Procedia Structural Integrity, 2022, 37, 547–554.

https://doi.org/10.1016/j.prostr.2022.01.121

Available online at www.sciencedirect.com

ScienceDirect

Procedia Structural Integrity 37 (2022) 547–554

Structural Integrity Procedia

www.elsevier.com/locate/procedia

ICSI 2021 The 4th International Conference on Structural Integrity

Method of Coaxial Accelerations Correlation for Quality Assessment of Structural Joints

Dmitrijs Serdjuks[a,*], Viktors Kurtenoks[a], Aleksejs Tatarinovs[b], Viktors Mironovs[c], Vjaceslavs Lapkovskis[d], Karina Buka-Vaivade[a], Andrejs Macevics[a], Kirills Topcijs[a], Martins Vilnitis[c]

[a]*Institute of Structural Engineering, Riga Technical University, Riga, LV-1048, Latvia*
[b]*Institute of Electronics and Computer Science, Riga, LV-1006, Latvia*
[c]*Institute of Construction Technology, Riga Technical University, Riga, LV-1048, Latvia*
[d]*Scientific Laboratory of Powder Materials, Riga Technical University, Riga, LV-1048, Latvia*

Abstract

Assessment of the stiffness of joints is important for the joints' design, monitoring the condition of building structures and prognosis of the lifetime and safety of buildings or its elements. Typically, such assessment is done in a non-destructive way using either shock or vibration analysis with a network of accelerometers as sensors. To improve the quality of diagnostics of structural joints and make it more specific, a method and measurement system implementing the principle of correlation of normalized coaxial accelerations measured in 3D space was proposed. The method is based on the mathematical analysis of vibrations of structural joints in 3 spatial directions using 3D accelerometers located at different parts of a joint and orientated coaxially. The correlation method was verified in a laboratory experiment using rigid, semi-rigid and pinned joints of timber beams. Stand with timber beams joined at right angles by steel plates and screws were fabricated and tested by static loading to confirm the present state of the joint. Timber beams with 150X50 mm solid sections made C18 strength class were used for the timber stand. The decrease of the joint's stiffness in the case of probable damages was modelled by the loosening of the steel screws. The stand was subjected to a vibration load provided by electrodynamics actuators fixed on one of the joint elements. This element was excited by a chirp signal in a frequency sweep range from 10 to 500 Hz, where the most prominent resonance of the stand was found. Acceleration responses were recorded by 3D accelerators placed on the loaded and connected beams. Peak values of the cross-correlation function between the responses from the correspondingly orientated pairs of coaxial accelerometers were determined. It was shown that the difference between the peak values of the correlation functions obtained for the rigid, semi-rigid and hinge joints enabled specification of the joints' stiffness.

* Corresponding author. Tel.: +371 26353082.
E-mail address: dmitrijs.serdjuks@rtu.lv

2452-3216 © 2022 The Authors. Published by Elsevier B.V.
This is an open access article under the CC BY-NC-ND license (https://creativecommons.org/licenses/by-nc-nd/4.0)
Peer-review under responsibility of Pedro Miguel Guimaraes Pires Moreira
10.1016/j.prostr.2022.01.121

© 2022 The Authors. Published by Elsevier B.V.
This is an open access article under the CC BY-NC-ND license (https://creativecommons.org/licenses/by-nc-nd/4.0)
Peer-review under responsibility of Pedro Miguel Guimaraes Pires Moreira

Keywords: Structural health monitoring, Vibration analysis; Structural joints; Coaxial accelerations

1. Introduction

As the number of people in the world is growing, achieving a faster construction process is actual. In this situation, a popular choice is using structural members, which are manufactured in plants away from the construction site. After that, they are delivered to the construction site to be erected and joined together.

One of the essential parts of structural analysis and design is the calculation of joints. Joints play an essential role in the behaviour of the building structures and can be classified according to the several criteria:

- Material of the joined structures (timber, steel, precast concrete)
- Loading situation (tension, compression, bending, shear, torsion)
- Stiffness of joint (rigid, semi-rigid, pinned)
- Joint type and/or fastener used (glued connections, carpentry connections, connections with mechanical fasteners, welded joint)

The stiffness of the joints particularly influences the total structural firmness of buildings. The stiffness control of the joints during the building lifetime is essential to ensure that the current situation corresponds to the designed one and that the building is safe. The joint stiffness affects the distribution of internal forces in a structure both in members and joints (ultimate limit state) and deformations (serviceability limit state). The joints are classified according to initial stiffness as:

- Pinned - does not transmit any bending moments
- Semi-rigid - transfers some bending moments, and its behaviour needs to be considered in global analysis
- Rigid - members are rigidly connected and fully transmit bending moments

The moment-rotation curve, which describes rotation deformation by angle as a function of the moment applied to joint, can be used to model the behaviour of the joints (Sagiroglu et al. (2015), Chittiprolu et al. (2014), Faridmehr et al. (2019), Baszeń (2017)). A full-scale experimental test must be performed to obtain the moment–rotation curve. Usually, the joints are assumed to be pinned or entirely rigid to simplify the analysis and design process. However, there are discrepancies between idealized and actual behaviour. No joint is ideally pinned or completely rigid, but there are some classification boundaries. For example, for the steel structures, the classification boundaries were devised to limit the error to 5% for internal forces and 20% for deformations (Šabatka et al. (2019), EN 1993-1-8 (2005)). The changes of internal forces are insignificant in the pinned and rigid region. The load capacity of the beam structures depends on the bending moment, so the ideally pinned connection is generally a conservative solution for the beam design. The object of interest for non-destructive testing methods are rigid joints. If, during the structure's lifetime fasteners that ensure the rigidity of the joint are destroyed, much greater internal forces and deformations will develop in the structure, and it potentially can be dangerous. In addition, as the result of increasing connection flexibility, significant second-order effects are formed in the structures (Faridmehr et al. (2019)). Therefore, checking the joints' current stiffness and comparing it with the initial stiffness is essential.

The structural health of joints is directly related to their stiffness. Structural health monitoring (SHM) methods enable investigation and testing of structural joints behaviour during the whole service life of buildings. Choice of SHM method depends on the material of the joined structural members, its loading case, joints' structure and stiffness. Since the beginning of the 21st century, many SHM methods have been developed to investigate structural behaviour based on shock and vibration analysis. Vibration analysis methods allow determining possible damages of structural joints based on frequency response, modal shape and damping. Methods of vibration analysis are classified into two categories - methods using ready-made mathematical models and methods that do not employ such the models for

vibration analysis (Boscato et al. (2019), Kamgar et al. (2012), Rahgozar (2020), Fang et al. (2020), Masciotta et al. (2017), Maksimenko (2003), EN 1993-1-8 (2005)).

The present study aimed to propose a vibration analysis method for the quality assessment of structural joints based on the correlation of coaxial accelerations from sensors orientated coaxially in space. The method does not employ ready-made mathematical models for vibration analysis. A stand composed of timber beams with a moment joint of variable stiffness was developed and tested using the proposed method to verify the feasibility of the latter.

2. Materials and methods

2.1. Method of coaxial correlations for quality assessment of structural joints

To improve the quality of diagnostics of structural joints and make it more specific, a method and measurement system implementing the principle of correlation of normalized coaxial accelerations measured in 3D space was proposed. The method is based on the mathematical analysis of vibrations of structural joints in 3 spatial directions using 3D accelerometers located at different parts of a joint and orientated coaxially. Analysis of vibration in 3D space enables one to check the stiffness of joints of planar structures, such as a joint of girder and additional beam, considered below for testing the proposed method.

The developed measuring device consisted of an electrodynamic actuator, two 3D accelerometers, a signals amplifier, an Arduino board for signals conversion and transfer, and a computer. The developed measuring device and its major components are shown in Fig.1.

The steps of data collection were as follows:

1. The vibration of the structure applying a sweeping signal in a wide frequency range from 10 to 500 Hz and a duration of 0.5 second
2. Processing the obtained vibration signals by the Fourier transform and determination of the maximum magnitude frequency in the spectrum corresponding to one of the natural frequencies of the structure
3. The vibration of the structure applying a narrow sweeping signal around the resonant frequency and recording 6 vibration signals from two 3D accelerometers
4. Repetition of measurements at each step of stiffness of the joint

Steps of data processing included:

1. Calculation of correlation functions between three coaxial directions of two 3D accelerometers placed on the joined beams
2. Determination of peak values of correlation functions (PVCF) in each coaxial pair of 3D accelerometers
3. Data averaging on several repeated measurements at each step of stiffness of the joint
4. Calculation of normalized peak values of correlation functions (further NPVCF (%)) as the main relative vibration parameter for the analysis, where the maximum PVDF value obtained in any of the coaxial pairs was taken as 100%



Fig. 1. (a) developed measuring device; (b) electrodynamic actuator; (c) Arduino board.

The calculation of PVCF between two data arrays, i.e., vibration signals in the time domain, from the first and second accelerometers F1 and F2, was performed according to the following algorithm:

- Removing the constant component from each signal F1, F2 by subtracting the average value in the entire time window (in our case, 1 sec)
- Addition to each of the signals on the left and right an array of zero values, with a duration of 1 sec
- Calculation of the convolution of the two received signals
- Determination PVCF as the maximum modulo value for the resulting convolution

Thus, vibration signals were collected from 3 coaxial pairs of two accelerometers rigidly placed on the joined elements of the stand and NPVCF parameter was finally determined as the measure of the stage of the joint's stiffness. NPVCF measured at the initial and reliably confirmed the stiff condition of a system or a building is proposed as the reference standard for further monitoring the system or building during its exploitation.

2.2. Timber beam stand

A stand of timber beams was arranged as shown in Fig.2 as a simple model in static loading and vibration test to verify the static diagram of the structure and evaluate the proposed method of coaxial correlations correspondingly. The stand consisted of a girder and an orthogonal beam forming T-connection and made of solid timber of C18 strength class with 150x50 mm cross-sections. The beam was freely supported, one with spans of 2.06 m and two spans of 1.5 m each. The girder and the beam were joined rigidly by steel corners and bolts. Static loading was concentrated vertical forces applied to steel pieces on two suspended platforms P1 and P2 shown in Fig.2. Static diagram of the stand depended on the stiffness of the joint varied by tightening screws and bolts in steel corners. A static test used six deflectometers and six strain gauges to verify the static diagram by 7 grades of the joint stiffness e stand.

Three static diagrams of the stand were considered for three conditions of the joint (Fig.3): rigid (moment) joint; pinned joint of the girder and beams; no connection between girder and beams when all screws and bolt were deleted. To join beams, steel screws of a diameter 4 mm, steel bolts of a diameter 8 mm, angle profiles Arras Construction Furniture OU 105x105x90x3.0 and perforated steel plates Arras Construction Furniture OU 200x50x3.0 were used. Perforated steel corners provided the joint's moment load-carrying capacity (rigidity), shown in Fig.3(a).

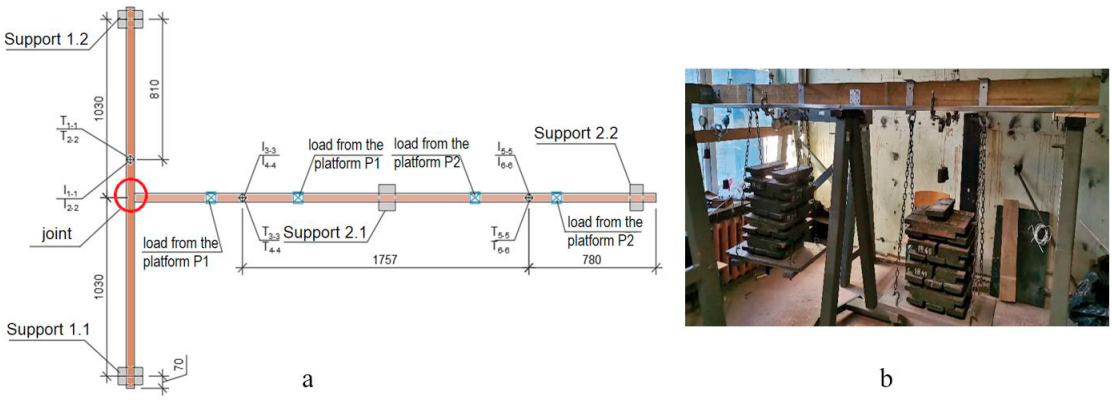


Fig. 2. Stand of timber beams: (a) layout of static load application; (b) view of the timber beams stand loaded by the set of concentrated vertical forces.



Fig. 3. Three variants of beam joints: (a) rigid (moment) joint; (b) pinned joint; (c) no connection.

3. Results and discussion

3.1. Results of a static experiment

The timber beam stand was statically loaded by the concentrated vertical forces system, applied as shown in Fig. 2. Loading steps with intensity 1 kN were applied first to platform P1 and then to platform P2. The maximum intensities of the vertical loads were equal to 4.74 kN for platform P1 and 4.69 kN for platform P2. The loading stages were divided into symmetric and non-symmetric ones. The loadings of the stand were repeated for the rigid and pinned conditions of the joint between the girder and the beam. The loading and unloading regimes coincided with the stages 1-6 and 7-12, correspondingly, and are shown in Fig.4 for symmetric and antisymmetric modes. The elastic modulus of the beam's material was estimated as 9.44 GPa.

The joints stiffness was determined based on the experimentally measured angle of the joint's rotation. The experimental values were compared with the values calculated by the FEM method using the software Axis VM Lite. Variants of the rigid (moment) and pinned joints were considered. The angle of the joint's rotation is shown in Fig. 4 as a function of the applied vertical load. The influence of the maximum vertical displacements of the beam on the angle of the joints rotation was taken into account. The experimentally obtained value of the rigid joint rotation angle was 0.0003 radians, while for the pinned joint, the same values were 0.0025 and 0.0026 radians by FEM and experiment. The maximum rotation angle of 0.018 degrees for the rigid joint was obtained for non-symmetric loading. The maximum rotation angle for the pinned joint was 0.173 degrees in the non-symmetric loading when the vertical loads were 4.74, and 3.75 kN were applied to platforms P1 and P2.

The static loading confirmed that desired conditions of the girder and the beam joints could be considered the rigid and pinned ones.

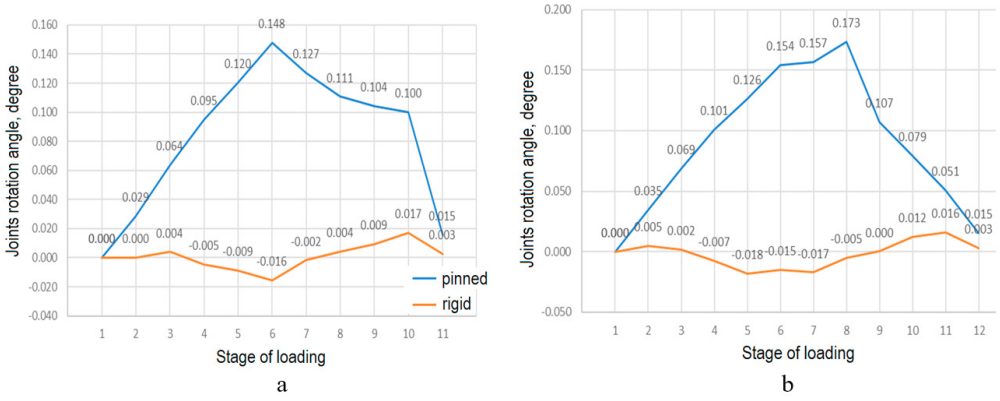


Fig. 4. The angle of the joint's rotation as a function from the applied vertical load for loading stages (a) symmetric; (b) non-symmetric.

3.2. Results of vibration experiment

The vibration test examined the ability of the proposed method of coaxial accelerations correlation to determine the stiffness of the joint in the timber beam stand. The decrease of the rigid joint stiffness was modelled by the gradual removal of screws and bolts in the connecting steel corners. Seven grades of stiffness were considered:

Grade 1 (initial): Rigid joint, all screws and bolts tightened (Fig.3(a))
Grades 2-5: rigid joint with the decreased stiffness with gradually loosened screws and bolts (Fig.5(b))
Grade 6: pinned joint, with only one bolt (Fig.3(b))
Grade 7: absence of the joint between the girder and the beam (Fig.3(c))

The beam was subjected to a vibration load provided by electrodynamics actuators, fixed on the edge of the beam, as shown in Fig. 5 (a). Vibration response signals in both parts of the joint, the girder and the beam, were recorded in 3 spatial directions by two 3D accelerometers fixed respectfully on the girder and the beam (Fig.5) and transferred to the computer. A vibration test was done at all seven grades of the joint.

Differences in the vibration signals were noted in three directions: 0-1, 2-3 and 4-5. The highest values of PVCF were obtained in the direction 4-5. NPVCF values, 5 repeated measurements and average, in 7 grades of joint stiffness are shown in Fig.6. The vibration experiment confirmed that the differences in vibration signals occur due to loss of the joint stiffness and the decrease of NPVCF values calculated from coaxial correlations reflect the grade of stiffness loss in the joint of the timber beams stand.

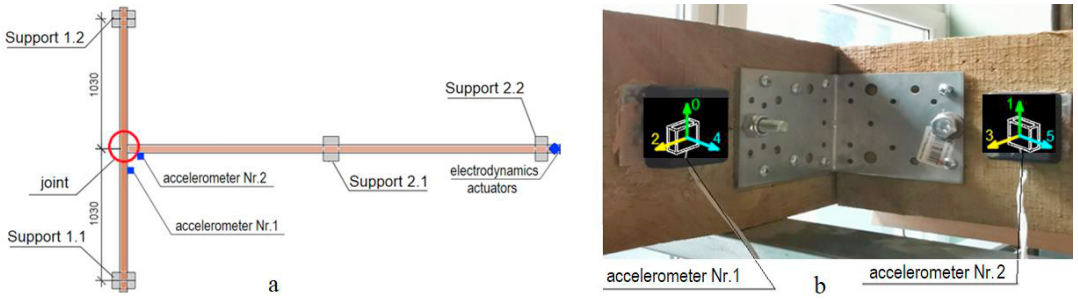


Fig. 5. (a) scheme of the timber beams dynamic loading; (b) accelerometers placement near considered joint with an indication of directions for vibration records fixations.

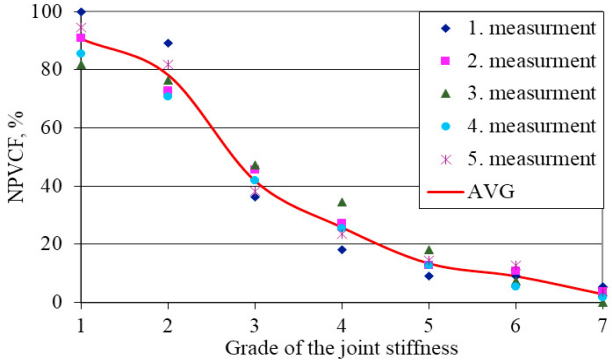


Fig. 6. Normalized peak values of correlation functions, obtained for the five measurements for the seven grades of the joint stiffness and its average values curve.

3.3. Discussion

Shear stiffness of the considered joint for grades 1-7 were analyzed according to the standard EN 1995-1-1 and shown in Fig.7 (a) by the blue line. Shear stiffness of the joint is obtained on the base of the slip modulus, calculated for the screws and the bolt according to EN 1995-1-1 (2004) and EN 26891 (2013). The shear stiffness of the screw with a diameter of 4 mm and the bolt with a diameter of 8 mm were 1.61 and 2.58 N/m. Shear stiffnesses of the joint were 61.8 and 10.3 N/m for the rigid and pinned conditions of the joint, correspondingly. It was shown that shear stiffness for 1-7 grades of the joint stiffness decreased consequently with the grade. NPVCF values reduced to shear stiffness and shown in the identical Fig.7(a) by red line had the same declining trend, but a different character with a sharper decrease between grades 2 and 3. Changes of the experimentally determined rotation stiffness and the respectively reduced NPVCF values by seven grades of the joint stiffness are shown in Fig. 7 (b). The patterns of the changes of the reduced NPVCF and rotation stiffness coincided to a large extent.

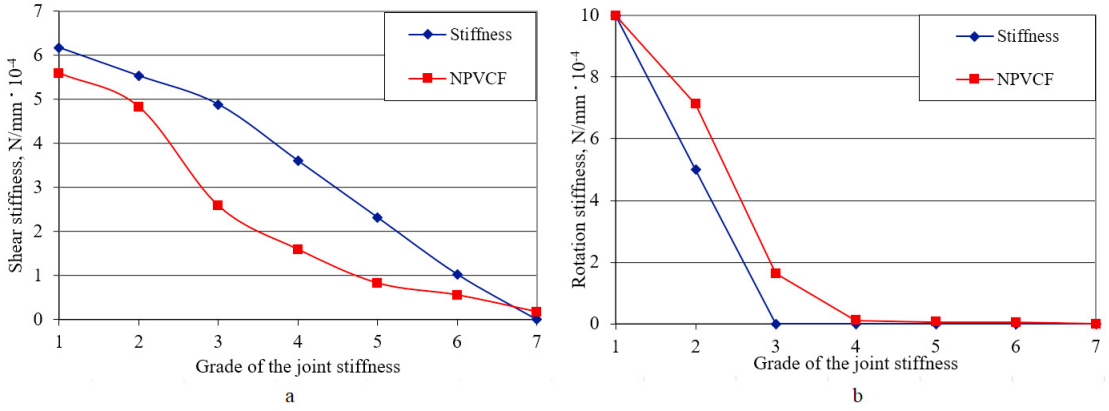


Fig. 7. (a) shear stiffness and corresponding normalized peak values of the correlation function for grades of stiffness 1-7 of the considered joint; (b) rotation stiffness and corresponding normalized peak values of the correlation function for grades of stiffness 1-7 of the considered joint.

The study showed that the differences between NPVSF parameters calculated based on 3D coaxial accelerometers correlation for the rigid, semi-rigid and pinned conditions of the joints enabled quantification and specification of the joint's shear and rotation stiffness. The proposed vibration analysis method of coaxial accelerometers correlation for quality assessment of structural joints was successfully demonstrated for timber beam joints. Analysis of vibration in 3D space enables assessment of the stiffness of joints of planar structures in general cases. For quality assessment of structural joints of spatial structures, the analysis of vibration in 6D space is preferable. It enables the evaluation of shear and rotation stiffness in 6 degrees of freedom.

4. Conclusions

A vibration analysis method of 3D coaxial accelerometers correlation for quality assessment of structural joints in three spatial directions was proposed. The method is based on the mathematical analysis of natural vibrations of structural joints in 3D spatial directions using 3D accelerometers located at different parts of a joint and oriented coaxially. The method enables the evaluation of the changes of the structural joint's shear and rotation stiffness caused by the damaging or degradation of the joint during exploitation.

The proposed method was experimentally tested on the timber T-joint in the rigid, semi-rigid and pinned conditions. It was shown that the difference between the peak values of the normalized correlation functions obtained for the rigid, semi-rigid and pinned joints enabled specification of the joints' shear and rotation stiffness.

Acknowledgements

This research was supported by Latvian Council of Science funded project “Method of correlation of coaxial accelerations in 6-D space for quality assessment of structural joints (COACCEL)” (Nr. lzp-2020/1-0240).

References

Baszeń, M., 2017. Semi-rigid Behavior of Joints in Wood Light-frame Structures. Procedia Engineering 172, 88-95.

Boscato, G., Fragonara, L.Z., Cecchi, A., Reccia, E., Baraldi, D., 2019. Structural Health Monitoring through Vibration-Based Approaches. Shock and Vibration, paper #2380616.

Chittiprolu, R., Ramancharla, P. K., 2014. Seismic Safety of Joints in Precast Buildings. A State-of-the-art Literature Review. Int. Seminar REDECON 2014, 9-13 November 2014, Bangalore, India.

EN 1993-1-8, (2005). Eurocode 3: Design of steel structures - Part 1-8: Design of joints. CEN, Brussels.

EN 1995-1-1, (2004). Eurocode 5: Design of timber structures - Part 1-1: General - Common rules and rules for buildings. CEN, Brussels.

EN 26891, (2013). Timber structures - joints made with mechanical fasteners - general principles for the determination of strength and deformation characteristics. CEN, Brussels.

Fang, L., Zhou, Y., Jiang, Y., Pei, Y., Yi, W., (2020). Vibration-Based Damage Detection of a Steel-Concrete Composite Slab Using Non-Model-Based and Model-Based Methods. Advances in Civil Engineering 2020, paper #8889277.

Faridmehr, I., Tahir, M. Md., Osman, M. H., Razavykia, A., (2019). An overview of the connection classification index. Advanced Steel Construction 15, 145–156.

Kamgar, R., Mehdi, M.S., (2012). A Simple Mathematical Model for Free Vibration Analysis of Combined System Consisting of Framed Tube, Shear Core, Belt Truss and Outrigger System with Geometrical Discontinuities. Applied Mathematical Modelling 36, 4918–4930.

Maksimenko, O., (2003). The diagnosis is “String”. Science and life 6. https://www.nkj.ru/archive/articles/2973/.

Masciotta, M.G., Ramos, L.F., Lourenco, P.B., Vasta, M., (2017.) Spectral Algorithm for Non-Destructive Damage Localization: Application to an Ancient Masonry Arch Model. Mechanical Systems and Signal Processing 84, 286–307.

Rahgozar, P., (2020). Free Vibration of Tall Buildings Using Energy Method and Hamilton’s Principle. Civil Engineering Journal 6, 945–953.

Sagiroglu, M., Aydin, A.C., (2015). Design and analysis of non-linear space frames with Semi-rigid connections. Steel and Composite Structures 18, 1405-1421.

Šabatka, L., Kolaja, D., Vild, M., Wald, F., Kuříková, M.., Kabeláč, J., (2019). Influence of joint stiffness on design of steel members. Advances and Trends in Engineering Sciences and Technologies III. CRC Press.

Serdjuks D., **Kurtenoks V.**, Tatarinovs A., Buka-Vaivade K., Lapkovskis V., Mironovs V., Podkoritovs A., Topcijs K.

Non-model vibration analysis method for health monitoring of structural joints.

Procedia Structural Integrity, 2022, 37, 555–562.

https://doi.org/10.1016/j.prostr.2022.01.122

Available online at www.sciencedirect.com

ScienceDirect

Procedia Structural Integrity 37 (2022) 555–562

Structural Integrity Procedia

www.elsevier.com/locate/procedia

ICSI 2021 The 4th International Conference on Structural Integrity

Non-model vibration analysis method for health monitoring of structural joints

Dmitrijs Serdjuks[a,*], Viktors Kurtenoks[a], Aleksejs Tatarinovs[b], Karina Buka-Vaivade[a], Vjaceslavs Lapkovskis[c], Viktors Mironovs[d], Andrejs Podkoritovs[a], Kirils Topcijs[a]

[a]*Institute of Structural Engineering, Riga Technical University, Riga, LV-1048, Latvia*
[b]*Institute of Electronics and Computer Science, Riga, LV-1006, Latvia*
[c] *Scientific Laboratory of Powder Materials, Riga Technical University, Riga, LV-1048, Latvia*
[d]*Institute of Construction Technology, Riga Technical University, Riga, LV-1048, Latvia*

Abstract

Structural health of joints plays an important role in the behavior of building structures. Structural Health Monitoring (SHM) methods make it possible to investigate and keep under control the behavior of structural joints during the entire service life of buildings. Choice of SHM methods depends on the material of the joined structural members, its loading case, joint's structure and stiffness. Since the beginning of the 21st century, many SHM methods have been developed to investigate the behavior of structures using vibration analysis. Vibration analysis methods can identify possible damages of structures or structural joints due to changes in frequency response, modal shape and damping. Methods based on vibration analysis are classified into two categories - methods using ready-made mathematical models and methods that do not employ models. Current paper discusses various vibration analysis methods for assessing a structural health of joints. Particular attention is paid to non-model based methods, as it avoid the need for complex mathematical representations of models for specific investigation objects. In the context of the development of vibration analysis methods for building structures, the authors propose the concept of a 3D coaxial acceleration correlations to study the joints behavior in three-dimensional space.

© 2022 The Authors. Published by Elsevier B.V.
This is an open access article under the CC BY-NC-ND license (https://creativecommons.org/licenses/by-nc-nd/4.0)
Peer-review under responsibility of Pedro Miguel Guimaraes Pires Moreira

Keywords: Nondestructive examination, Structural Health Monitoring, Joints

* Corresponding author. Tel.: +371 26353082.
E-mail address: dmitrijs.serdjuks@rtu.lv

2452-3216 © 2022 The Authors. Published by Elsevier B.V.
This is an open access article under the CC BY-NC-ND license (https://creativecommons.org/licenses/by-nc-nd/4.0)
Peer-review under responsibility of Pedro Miguel Guimaraes Pires Moreira
10.1016/j.prostr.2022.01.122

1. Introduction

Structural health of the building is determined by the structural health of its separate members and joints. Behavior of structural members and joints should be carried under the control during the whole service life of the building. Distribution of internal forces and deformations in structural members and joints depends on the joint's stiffness. The stiffness is the major parameter, which determines structural health of the joints and influences on the behavior of the whole building. The joints are divided into the following groups according to its initial stiffness: pinned joints, semi-rigid joints and rigid joints. Pinned joint does not transmit any bending moments and joined members have possibility of free rotation in case if the friction forces are neglected. Semi-rigid joint transfers some bending moments by its sub-members and connections and its behavior should be considered in global analysis of the whole buildings structure. Members are rigidly connected to each other and fully transmit bending moments in the rigid joint. The moment-rotation curve (Fig. 1 (a)), which describes rotation deformation by angle θ as a function of the moment M, applied to the joint, must be used to model the joint's behavior (Sagiroglu et al. (2015), Chittiprolu et al. (2014), Faridmehr et al. (2019), Baszeń (2017)).

Joints of steel structures can be divided into the following groups depending on the types of joined steel members (Fig.1 (b)): beams to columns joints (A); beams to beams joints (B); columns to columns joints (C); columns to foundation joints (D).

A full-scale experimental test must be performed to obtain the moment-rotation curve, which describes rotation deformation by angle θ as a function of the moment M, applied to the joint. Relation of the joint to the certain group is determined by the existing classification boundaries. The classification boundaries were devised to limit the error to 5% for internal forces and 20% for deformations for steel structures (Šabatka et al. (2019), EN 1993-1-8 (2005)). The changes of internal forces are insignificant in pinned and rigid region even if the stiffness changes 100 times and changing rapidly in the semi-rigid region.

The object of the interest for non-destructive testing methods are rigid and semi-rigid joints. Increased internal forces and deformations will develop in the structure if fasteners and details that provide the rigidity of the joint are damaged or destroyed during the service life. Significant second order effects are formed in the steel structures as the result of decreased joints stiffness (Faridmehr et al. (2019)). Therefore, the ability to check the stiffness of the joints and to compare it with the initial stiffness is important. Semi-rigid and pinned beams to beams conditions of a joint are investigated in the current study.

Choice of structural health monitoring methods depends on the material of the joined structural members, its loading case, joint structure and stiffness. Vibration analysis methods make it possible to determine possible damages of structures or structural joints due to changes in the frequency response, modal shape and damping. The methods based on vibration analysis are divided into two categories - methods using ready-made mathematical models and methods that do not employ models.

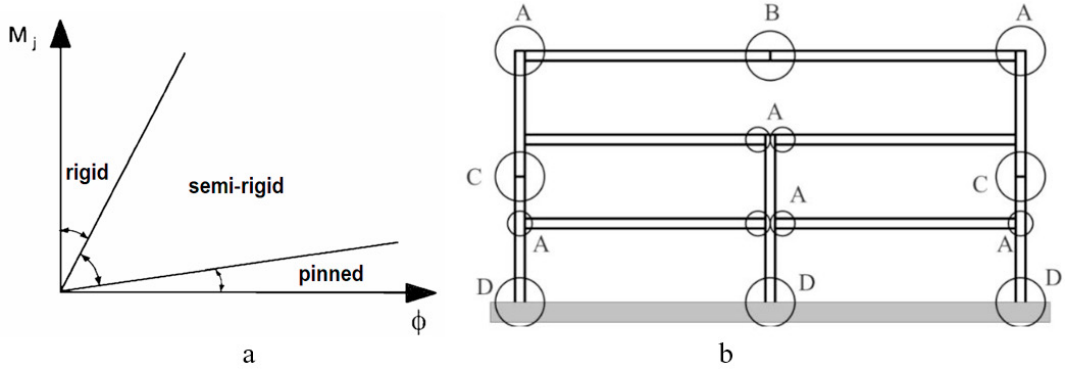


Fig. 1. Groups of structural joints (a) according to its initial stiffness; (b) according to the type of steel members are joined.

The aim of current investigation was to determine a structural joint's stiffness as a function of the vibration parameters of the structure. A non-model vibration analysis method of coaxial accelerations correlation was used. For this, it was necessary to provide a measuring device with a description of its components and the main stages of application of the proposed method. A stand was also developed and tested from steel beams with a semi-rigid connection of variable stiffness was also developed and tested.

2. Methods for health monitoring of structural joints

The application of non-destructive testing (NDT) methods to assessing the quality of structural joints is largely determined by the critical elements of the joints that perform the connecting function. For example, in welded joints, the main determinants of the quality of the joint are the quality and defect-freeness of the weld itself. In bolted joints, the quality of the assembly is determined by the quality of the bolts and the degree of their tightening, whereas in adhesive joints, such an indicator is the quality of adhesion of the elements being fastened. Respectfully, NDT methods in these cases are specific to key elements examined. So welded joints are checked by ultrasonic testing in a pulse-echo mode using either a single-channel device, a phase array system, or the time-of-flight diffraction method (Ahmad et al. (2018)). For NDT of adhesive joints, the echo-pulse method applying the analysis of ringing tones in multiple reflections and the propagation of Lamb waves in plates were found suitable (Zeighami et al. (2009), Heller et al. (2000)).

At the same time, there is a need for holistic methods that allow an integral assessment of the functionality of a structural joint by a non-destructive way without specific addressing to its structural elements. Such methods, traditionally attributed to the field of structural health monitoring (SHM) use mechanical impact on the joint as a whole and recording the responses of the reactions from its structural elements. In this case, the impact levels can be close to those at the operating conditions, including extremal ones, or be significantly lower, taking as an assumption the linear behavior of the system. According to the way of exposure, the methods are subdivided into shock and vibration modes using a short pulse impact or a continuous oscillation, correspondingly, and referring to dynamic testing modalities both (Hanly (2016)). Both shock and vibration testing are historically acknowledged methods with standardized guidelines for the measurement and evaluation of the effects on structures (ISO 4866 (2010)), and dynamic testing procedures for investigation of building structures such as bridges (ISO 14963 (2003)).

Dynamic characteristics of structural systems highly depend on joint properties. Due to the complexity of joints, it is highly difficult to describe dynamic behavior of joints with analytical models only. Reliable models are generally obtained using experimental measurements. Frequency response function (FRF) of structures containing a set of resonant peaks of natural frequencies, damping and mode shape can be obtained analytically or experimentally allowing the calculation of the stiffness of the structure with certain limitations (Tol et al. (2012)).

All types of accelerometers, single and multi-axes electromechanical sensors, transforming energy of motion into an electrical output are used to measure responses on shock and vibration. The advent of low-cost MEMS accelerometers and open-source electronic platforms, such as Arduino, have facilitated the design of low-cost systems suitable for modal identification and measuring natural frequencies and damping ratios in building structures, including multi degree of freedom (DOF) systems (Varanis et al. (2018)). Dynamic behavior of big structures, such as high-rise buildings, assessing its horizontal and vertical displacements and fluctuations is proposed to monitor by differential global positioning systems (GPS) with a reference to a stationary GPS station [A9]. The experimental technique used to determine the dynamic characteristics of buildings is based on records of low intensity oscillations of the building produced by various natural factors, such as micro seismic agitation motions, city traffic, wind etc. (Park et al. (2018)). In another option of vibration testing of building structures, reasonably accurate evaluation can be frequently obtained by a simple technique such as floor response at a single point due to heel drop compared by its testing effect with thorough modal analysis of multiple synchronous measurements with a transducers network (Dobre et al. (2017)).

Application of multi-sensor accelerometer network, particularly two tri-axial accelerometers allowed for the enhancement of damage indicator when the structure is perturbed sensors, laying the basis for the creation of an IoT system for SHM (Nguyen (2020)). It was shown that multi-axis test was more representative of a true operational environment. Thus 6 DOF testing system improved the traditional 1 DOF approach by a more representative stress state in a test article during mechanical shock and vibration (Muttillo et al. (2020)). To monitor the 6-DOFstructural

displacement with high accuracy, a vision-based displacement measurement system was proposed (Hoksbergen (2013)). The system was composed of a uniquely designed marker and a camera, where relative translational and rotational displacement between the marker and the camera was estimated by finding a homograph transformation. Laser vibrometer, in which the natural resonance modes are measured excited by a shaker and measured using a laser interferometer, is routinely performed in 2D for out-of-plane displacement patterns on vibrating structures, and, with greater system complexity, in 3D for in-plane displacement measurements (Jeon et al. (2014)). Combining dynamic SHM methods using ultrasonic guided waves and vibrations with static strain-based sensors and sensors for environmental entities might yield a robust multi-sensor SHM approach based on data fusion (Castellini et al. (2006)).

In order to determine structural damage to structures, mathematical models are often used to help identify structural damage and to help identify the location of the damage and the trends for further failure. However, it is not always possible to use a modelling approach, as the structures being assessed can be complex interacting elements where it is hardly possible to apply mathematical models.

In such cases, an alternative approach based on non-model methods of analysis may be appropriate. In this case, non-model methods are used based on the analysis of experimentally obtained data to determine the correlations between the measured parameters in order to identify patterns inherent in different types and intensities of damage. The non-model approach is based on the use of numerical methods for processing the input data. The result is an empirical model which can be linked to specific scenarios of structural components damage.

Non-model methods for analyzing assemblies and structures include methods for assessing the response of a structure or assemblies exposed to vibration.

Current methods for evaluating vibration monitoring systems by non-model vibration analysis methods are summarised below:

- Non-model-based damage identification using measured mode shapes
- Non-model-based identification using a continuously scanning laser doppler vibrometer system
- Vibration based damage assessment technique based on damage index (DI) method
- Vibration-based damage detection based on combination of multiple reference impact test and finite element model

The next chapter describes a non-model vibration analysis method for correlating coaxial accelerations, a measuring device with a description of its components and the main stages of applying the proposed method.

3. Materials and methods

3.1. Method of coaxial accelerations correlation for quality assessment of structural joints

A non-model vibration analysis method of coaxial accelerations correlation is proposed. The method is based on the mathematical analysis of vibrations of structural joints in 3 spatial directions using 3D accelerometers, located at different parts of a joint and orientated coaxially. Analysis of vibration in 3D space enables to test the stiffness of joints of planar structures, such as a T-joint of the girder and additional beam. The developed measuring device and its major components are shown on the Fig. 2 (a).

The method of verification comprised the following steps of data collection. A frequency sweep audio signal in a wide frequency range from 10 to 500 HZ and a duration of 0.5 second was applied to the tested structure. The obtained vibration record (Fig. 2 (c)) passed the Fourier transform and the maximum magnitude frequency of the spectrum was selected. A new signal of the selected frequency was applied the next. Several measurements were recorded at each condition of the joint stiffness.

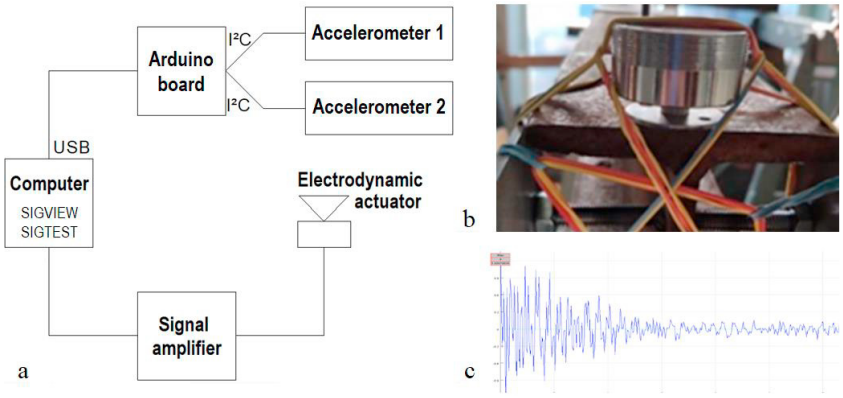


Fig. 2. (a) proposed measuring device with its major components; (b) electrodynamic actuator and it fastening on the steel beam; (c) vibration record.

Vibration records were taken by two 3D accelerometers and the differences of the records were compared for all three directions. Peak values of the cross-correlation function between the responses from the correspondingly orientated pairs of coaxial accelerometers were determined and averaged. The data processing in the following stages: processing of the correlation function between coaxial directions of accelerometers; determination of peak values of correlation functions; averaging of peak values for same stiffness of the joint and directions; and normalization of the values obtained in the previous stage from minimum to maximum in range from 0 to 100 %. SigView software of SigTest (https://sigview.com) was used for processing the vibration signals. Normalized correlation function was calculated as the final measurement outcome. Firstly, the convolution of two signal functions, the responses from accelerometer 1 and accelerometer 2, were calculated. The peak value of the correlation function was determined as the maximum modulo value for the resulting convolution. The peak values in each pair of the coaxial directions were normalized by the maximum value in the experiment.

3.2. Description of investigated steel beams joint

A steel beam stand was used to verify the suggested non-model method of vibration analysis for SHM of structural joints, where stiffness of structural joints was a function of vibration parameters of the structure. The steel beam stand, consisting of the main and additional beams, joined together by the semi-rigid joint of a variable stiffness, was the object of the investigation (Fig.3). Both beams have HEA 100 cross sections. Material was S355 strength class steel. The beams were joined by a SRS bolt with the strength class 8.8 and a diameter of 8 mm. The stand was loaded by a system of concentrated vertical forces that varied within a range from 0 to 10 kN. Each step of loading was equal to 1 kN. The vertical loads were applied by adding of the steel pieces to the loading platforms. Three couples of deflectometers and strain measuring devices were used to determine the experimental values of stresses and maximum vertical displacements. Maximum vertical displacements and stresses were determined in positions I, II and III, which are shown in the Fig. 3.

Two stages of the steel beams joint were considered in course of the statical experiment. Rigid joint was obtained when the bolt was completely fixed by the maximum force added to the nut by torque wrench. The corresponding torque moment was equal to 150 Nm. Pinned joint was created when the nut was deleted (Topcijs (2021)).

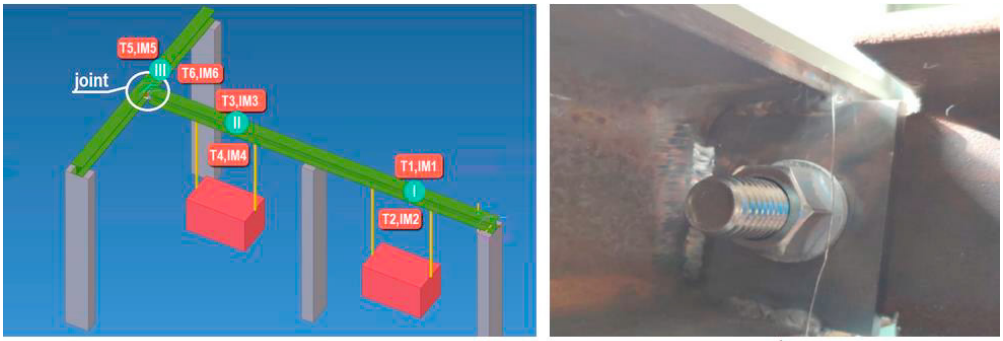


Fig. 3. (a) steel beams stand, consisting of the main and additional beams; (b) semi-rigid joint with variable stiffness of the joint between the main and additional beams; I, II and III are positions, where stresses and vertical displacements were determined.

4. Results and discussion

4.1. Results of static loading

Static test of the steel beam stand was carried out to specify the static diagram of the stand and beams' joint stiffness. Experimentally and analytically obtained values of the maximum vertical displacements and stresses at all loading stages are shown in the diagrams for position III (middle of the span of the girder) in Fig 3a. The values of the maximum vertical displacements and normal stresses when the structure was loaded by the total vertical load of 10 kN are shown in Tables 1 and 2 for positions I, II and III. The values are obtained for the case, when the joint of the steel beams have it maximum stiffness and considered as a rigid one.

Table 1. Comparison of experimental and design values of the maximum vertical displacements.

Position	Experimental maximum vertical displacements, 10^{-2} mm	Design maximum vertical displacements, 10^{-2} mm	Difference Δ, 10^{-2} mm	Difference Δ, %
I	15.25	14.10	1.15	7.54
II	31.00	29.90	1.10	3.55
III	39.50	37.80	1.70	4.30

Table 2. Comparison of experimental and design values of normal stresses.

Position	Experimental normal stresses, MPa	Design normal stresses, MPa	Difference Δ, MPa	Difference Δ, %
I	8.14	7.60	0.54	6.61
II	6.83	6.38	0.45	6.52
III	10.24	10.45	0.21	2.08

Comparison of experimentally and analytically obtained results enabled to conclude that considered joint could be considered as the rigid one when the total value of the vertical load did not exceed 10 kN. The difference between the experimentally and analytically obtained results was 6.61% for stresses and 7.54% for the maximum vertical displacements. Results obtained for the pinned joint also showed high correspondence between the experimentally and theoretically obtained values. The difference between the experimentally and analytically obtained results was 9.06% for stresses and 6.21% for the maximum vertical displacements. It enabled to conclude that considered variant of the beams joint was the rigid one at the applied level of loading (Topcijs (2021)).

4.2. Results of dynamic loading

Dynamic test of the steel beam stand was carried out to determine the structural joint stiffness as a function of the vibration parameters of the structure. The joints stiffness was varied by the force of the nuts warping. The steel beam joints stiffness was numerically valued by the maximum bending moment, which it could take up. The stiffness of the joint corresponded to the values of torque moment varying during the experiment within a range from 0 to 150 Nm. The value of the maximum torque moment equal to 0 Nm corresponded to the pinned joint.

The additional beam was vibrated by an electrodynamic actuator fixed on the edge of the additional beam (Fig.2 (b)). Vibration responses from two parts of the joint were recorded in 3 spatial directions by two 3D accelerometers, accelerometer 1 on the girder and accelerometer 2 on the additional beam as shown in Fig. 4 (a), and transferred to the computer. The differences in the vibration signals were measured in three directions: 0-1; 2-3 and 4-5. Normalized correlation factor was calculated according to the procedure described in 3.1. The maximum correlation factors in three coaxial directions 0-1; 2-3 and 4-5 were indicators of the structural joints stiffnesses. The obtained dependencies of the normalized correlation coefficient on the bending moment are shown in Fig. 5. The obtained dependence is non-linear and the largest increase of the correlation factor was stated for torque moment within a range from 0 and 50 Nm.

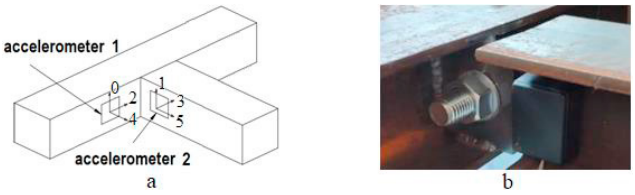


Fig. 4. (a) layout diagram of accelerometers at the investigated joint; (b) accelerometer placement at the joint.

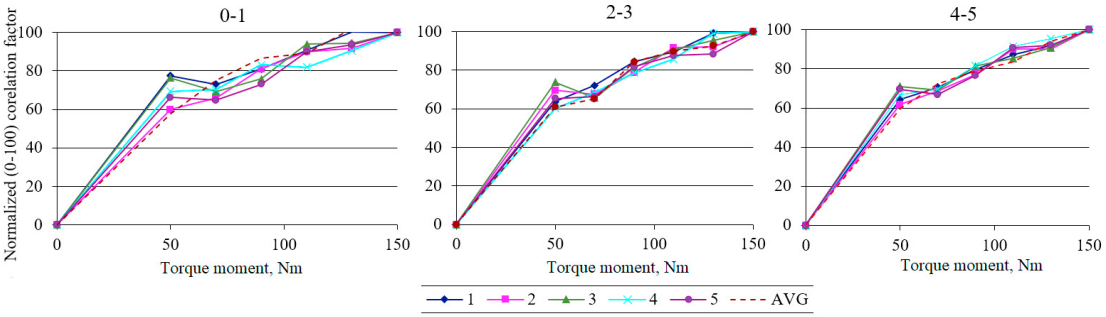


Fig. 5. Torque moment as a function of the maximum coaxial correlation factors in direction 0-1; 2-3; 4-5.

5. Conclusions

Non-model vibration analysis method for health monitoring of structural joints was proposed and experimentally tested using a steel beam stand. The experimental results obtained on the rigid and pinned joints adequately describe the results of analytical calculations.

Structural joint stiffness was determined as a function of the correlation factor determined based on measured natural frequencies. The stiffness of the joint corresponded to the values of torque moment, varying during the experiment within a range from 0 to 150 Nm. The direct relationship was found between the correlation factor and the stiffness of the joint. The higher correlation factor corresponded to the larger stiffness of the joint. The obtained dependence is non-linear, and the largest increase of the correlation factor was stated for torque moment within a range from 0 and 50 Nm.

Acknowledgements

This research was supported by the Latvian Council of Science funded project “Method of correlation of coaxial accelerations in 6-D space for quality assessment of structural joints (COACCEL)” (Nr. lzp-2020/1-0240).

References

Ahmad, A., Bond, L.J., 2018. Fundamentals of ultrasonic inspection. ASM Int. 17, 155–168.
Baszeń, M., 2017. Semi-rigid Behavior of Joints in Wood Light-frame Structures. Procedia Engineering 172, 88-95.
Castellini, P., Martarelli, M., Tomasini, E.P., 2006. Laser doppler vibrometry: development of advanced solutions answering to technology's needs. Mech. Syst. Signal Process. 20 (6), 1265–1285.
Chittiprolu, R., Ramancharla, P. K., 2014. Seismic Safety of Joints in Precast Buildings. A State-of-the-art Literature Review. Int. Seminar REDECON 2014, 9-13 November 2014, Bangalore, India.
Dobre, D., Dragomir, C.S., 2017. Dynamic characteristics of buildings from signal processing of ambient vibration. IOP Conf. Series: Materials Science and Engineering 245, paper #022087.
EN 1993-1-8, 2005. Eurocode 3: Design of steel structures - Part 1-8: Design of joints. CEN, Brussels.
Faridmehr, I., Tahir, M. Md., Osman, M. H., Razavykia, A., (2019). An overview of the connection classification index. Advanced Steel Construction 15, 145–156.
Hanly, S. W., 2016. Shock & Vibration Testing Overview. Engineering ebook, p.69.
Heller, H., Jacobs, L., Qu, J., 2000. Characterization of adhesive bond properties using Lamb waves. NDT & E International 33, 555-563.
Hoksbergen, J., 2013. Advanced high-frequency 6-DOF vibration testing using the Tensor. Sound and Vibration 47(3).
ISO 14963. 2003. Mechanical vibration and shock — Guidelines for dynamic tests and investigations on bridges and viaducts. CEN, Brussels.
ISO 4866, 2010. Mechanical vibration and shock — Vibration of fixed structures — Guidelines for the measurement of vibrations and evaluation of their effects on structures. CEN, Brussels.
Jeon, H., Kim, Y., Lee, D., Myung, H., 2014. Vision-based remote 6-DOF structural displacement monitoring system using a unique marker. Smart Structures and Systems 13(6), 927-942.
Muttillo, M., Stornelli, V., Alaggio, R., Paolucci, R., Di Battista, L., de Rubeis, T., Ferri, G., 2020. Structural Health Monitoring: An IoT Sensor System for Structural Damage Indicator Evaluation. Sensors 20(17), paper #4908.
Nguyen, T.H.A., 2020. Vibration testing for dynamic properties of building floors. IOP Conf. Ser.: Mater. Sci. Eng. 869, paper #052005.
Park, H.S., Oh, B.K., 2018. Real-time structural health monitoring of a supertall building under construction based on visual modal identification strategy. Autom. Constr. 85, 273–289.
Sagiroglu, M., Aydin, A.C., 2015. Design and analysis of non-linear space frames with Semi-rigid connections. Steel and Composite Structures 18, 1405-1421.
Šabatka, L., Kolaja, D., Vild, M., Wald, F., Kuříková, M., Kabeláč, J., 2019. Influence of joint stiffness on design of steel members. Advances and Trends in Engineering Sciences and Technologies III. CRC Press.
Tol Ş., Özgüven, H.N., 2012. Dynamic characterization of structural joints using FRF decoupling. Proceedings of the SEM IMAC XXX Conference 5, 449-460.
Topcijs, K., 2021. Steel structures joints quality analysis with vibration loads. Master thesis. Riga Technical university, Riga, p.105.
Varanis, M., Silva, A.L., Mereles, A.G., 2018. On mechanical vibration analysis of a multi degree of freedom system based on arduino and MEMS accelerometers. Rev. Bras. Ensino Fis. 40, e1304–e1314.
Zeighami, M., Honarvar, M., 2009. New approaches for testing of adhesive joints by ultrasonic C-scan imaging technique. Materials Evaluation 67(8), 935–45.

Buka-Vaivade K., **Kurtenoks V.**, Serdjuks D.

Non-destructive damage detection of structural joint by coaxial correlation method in 6D space.

Buildings, 2023, 13(5), 1151.

https://doi.org/10.3390/buildings13051151

buildings

MDPI

Article

Non-Destructive Damage Detection of Structural Joint by Coaxial Correlation Method in 6D Space

Karina Buka-Vaivade *, Viktors Kurtenoks and Dmitrijs Serdjuks

Institute of Structural Engineering, Riga Technical University, LV-1048 Riga, Latvia; viktors.kurtenoks@rtu.lv (V.K.); dmitrijs.serdjuks@rtu.lv (D.S.)
* Correspondence: karina.buka-vaivade@rtu.lv

Abstract: Failure of joints can lead to structural collapse. It is vital to monitor joint stiffness during operation to prevent such failures. This paper proposes a novel method for the quality assessment of structural joints using coaxial correlation in 6D space. Coaxially placed 6D sensors on either side of the joint implemented by 3D accelerometers and 3D gyroscopes with wide frequency range, automatic synchronisation between the input signal and receivers and response signal averaging are presented. The root mean square (RMS) value from the obtained signals convolution is proposed as a measure of the similarity between two signals for monitoring joint degradation. The method's effectiveness was tested on steel beam splice connection, where it was found that the RMS of convolution signals in 6D space showed a direct correlation between the calculated RMS value in X, Y, GX, and GY axes directions and the stiffness grades of the joint. The paper concludes that the nature of the RMS during the degradation of the joint may change in different axes, and wrongly chosen axes may lead to wrong conclusions regarding the state of the investigated joint, especially in the case of complex joints, so that the measurements in 6D provide higher reliability of the result interpretation.

Keywords: non-destructive test; dynamic response; structural joints; coaxial accelerations; structural health monitoring; splice connection; vibration test; convolution; time domain; moment-resisting joint

check for updates

Citation: Buka-Vaivade, K.; Kurtenoks, V.; Serdjuks, D. Non-Destructive Damage Detection of Structural Joint by Coaxial Correlation Method in 6D Space. *Buildings* **2023**, *13*, 1151. https://doi.org/10.3390/buildings13051151

Academic Editor: Egidio Lofrano

Received: 28 March 2023
Revised: 17 April 2023
Accepted: 19 April 2023
Published: 26 April 2023

Copyright: © 2023 by the authors. Licensee MDPI, Basel, Switzerland. This article is an open access article distributed under the terms and conditions of the Creative Commons Attribution (CC BY) license (https://creativecommons.org/licenses/by/4.0/).

1. Introduction

Structural failures in building structures are often attributable to the failure of the structural components connecting the structural elements. Such failures of the structural units can occur due to a loss of strength or buckling of their elements resulting from decreases in their parameters during operation or design errors [1]. One of the most devastating examples of such structural failures is the collapse of the roof of the Maxima shopping centre in Riga, Latvia, in 2013. The cause of the accident was traced back to the failure of the assembly joint of the bottom chord of a trapezoidal steel truss, which served as the main load-bearing structure for the roof. The consequences of the roof collapse and the fault joint leading to the accident are depicted in Figure 1.

This is just one example of the importance of joints and the global impact on the whole structure. Therefore, it is essential to ensure that the joint stiffness corresponds to the designed level during operation [2,3].

A joint's stiffness directly impacts the distribution of internal forces and deformations within a structure [4]. Joints can be classified as pinned joints, which are a more conservative solution since the beams are designed for higher bending moment values, as the moment is not transmitted through the joint, and moment-resisting joints. Moment-resisting connections are connections between structural members that are designed to transfer bending moment between them. They are commonly used in multi-story buildings, bridges, and industrial facilities where the structure is subject to high horizontal or lateral loads. The design of moment-resisting connections involves ensuring that the connection is strong and stiff enough to transfer the bending moment without excessive deformation or

failure. In steel structures, moment-resisting connections are often achieved through the use of welded or bolted connections.



Figure 1. Deadly store roof collapse due to the failure of the metal joint.

Bolted connections can be designed as moment-resisting connections by using high-strength bolts and plates with sufficient thickness and stiffness to transfer the required bending moment. However, bolted connections generally have lower stiffness and strength compared to welded connections and are more prone to fatigue and failure over time due to cyclic loading [5]. Welded connections, on the other hand, can provide higher stiffness and strength compared to bolted connections, and are often preferred in situations where high loads and bending moments are expected. After the Northridge earthquake in California in 1994, where welded connections showed inadequate performance, bolted connections have been deeply studied [6–8], increasing the popularity of combination of welded and bolted moment connections, such as bolted end-plate connection, extended end-plate connection, flange plate moment connections and others, which can offer high ductility with good ability to dissipate energy, which is essential in the case of seismic or cyclic loading, as well as high quality and prompt assembly [6,9].

The inspection and maintenance during steel structures operation is required for the moment-resisting joints as the redistribution of moments decreases as the joint loses its stiffness, leading to higher internal forces and significant second-order effects [10]. Therefore, the moment-resisting joints are of interest for non-destructive testing (NDT) methods and it is essential to check the existing stiffness of the joint and compare it with the initially designed stiffness.

The vibration method is a commonly used non-destructive technique [11]. Vibration-based techniques for identifying damages in joints is a constantly evolving and advancing field, with new methods and technologies being developed and continuously tested.

Generally, the non-destructive quality control vibration method involves three primary stages [12]. The first stage involves applying vibrations to a specimen using special equipment, such as modal impact hammers or advanced shakers, depending on the desired frequency range or ambient vibrations [13,14]. In the second stage, the vibrational response of the specimen is measured using either contact sensors, such as accelerometers [15], or noncontact sensors, such as laser doppler vibrometers. Several emerging technologies, such as fibre-optic sensing and wireless sensor networks, are also being developed to enable real-time monitoring of joint health and detect any changes in its condition [16–19]. Finally, in the third stage, the obtained data from the second step is processed to identify changes and characterise the system.

There are many different approaches to processing the data obtained. One of the common techniques is the use of frequency response functions (FRFs) to identify changes in the dynamic behaviour of the joint, which can indicate the presence of damage [20–23]. FRF of a linear mechanical system is defined as the Fourier transform of the time domain response divided by the Fourier transform of the time domain input [24]. Other techniques involve using wavelet transform analysis instead of Fourier analysis, which makes it

possible to analyse dynamic behaviour in the signal, so that is a powerful tool for use in artificial intelligence and machine learning algorithms to process vibration signals and identify damage patterns in the joint [25,26]. Another approach involves the estimation of changes in the dynamic properties of the specimen, including vibration frequencies, damping ratios, and modal shapes, by using either experimental modal analysis (EMA) or operational modal analysis (OMA) [22,27–30].

This paper proposes a novel method for assessing the quality of structural joints using coaxial correlation in 6D space, which involves the use of 6D sensors with a wide frequency range, automatic synchronization, and response signal averaging to measure joint stiffness. The proposed method for quality control of moment-resisting structural joints involves exciting the structure with a known input signal and measuring the structure's response by using a pair of coaxially positioned sensors. The sensors are symmetrically placed on either side of the joint, aligned with its axis. The post-processing by correlation of obtained measured responses is made to predict the damages in the joint. The proposed method was verified for bolted splice connection between IPE 80 steel beams. It is a commonly used and easily accessible parallel flange I section that allows focusing on the evaluation of joint degradation using a simple, relatively lightweight, and effective moment joint model for the laboratory test. The chosen joint solution is specifically selected because of its simplicity and the ease of simulating the degradation of a moment-resisting joint in laboratory conditions. This is accomplished by reducing the stiffness of the joint through the loosening of bolts. The verification aimed to determine the relationship between the correlation of measured specimen responses and joint stiffness to verify the proposed method's concept and evaluate its effectiveness for assessing structural moment-resisting joint degradation in steel beams.

2. Materials and Methods

2.1. Improved Coaxial Correlations Method for Structural Joints Quality Evaluation

The proposed method for evaluating the degradation of the structural joint was shown promising results in the case of T-type joints, where two beams are joined at right angles to each other, forming a T-shape, both for timber and steel structures [31,32]. However, the first version of the method for evaluating the quality of structural joints, which involves using an electronic testing system and mathematical analysis of the recorded data, as described in [31,32], also had several shortcomings. For example, there was an insufficient frequency range of the used sensors, the possibility of measurements only in 3D space, inconvenience related to the manual handling of multiple repeated measurements, and the need for strong input signals.

The electronic system's first improvement involves using 6D sensors implemented by MPU-9250, which contains a 3-axis gyroscope and a 3-axis accelerometer. Three-dimensional gyroscopes consist of three independent vibratory MEMS rate gyroscopes, which detect rotation about the X, Y and Z axes. The analog-to-digital converter (ADC) sample rate for 3D gyroscopes is programmable from 8000 samples per second. The ADC sample rate for 3D accelerometers is 4000 samples per second. The 16-bit resolution of the ADC device has been used, which provides that each sample can take one of 2^{16} possible values, ranging from −32,767 to 32,767. The 16-bit resolution of the ADC device allows for a high level of precision in the digital representation of the signal amplitude.

Based on Nyquist theorem [33], also known as the sampling theorem, the sampling frequency must be at least twice the maximum frequency of the original signal to reconstruct an analog signal from its sampled digital representation accurately:

$$f_{\text{sampling}} \geq 2 \times f_{\text{input,max}}, \tag{1}$$

where f_{sampling} is the ADC sample rate, the number of samples per second; $f_{\text{input,max}}$ is the highest frequency component of the sampled signal. Therefore, the frequency range for 3D accelerometers is 0 Hz to 2000 Hz, and for 3D gyroscopes it is 0 Hz to 4000 Hz. It has been hypothesised that 6D sensors can describe the state of the joint more fully, which

would be especially important in the case of complex joints. The second improvement is the introduction of automatic synchronisation between the input signal and the receivers, as well as the use of the averaging method, which made it possible to significantly decrease the influence of the noise in the measurements of the structure's response and made it possible to use even weak excitation signals for measurements. It is suggested to use at least 16 scans for significant (four times) improvement in the signal-to-noise ratio [34]. The improved electronic testing system is shown in Figure 2.

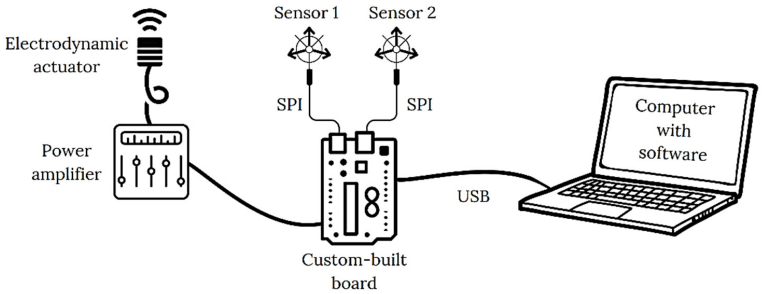


Figure 2. Scheme of the improved proposed electronic system with its major components.

The enhanced system includes 6D sensors with a wider frequency, and a custom-built board instead of the previously used Arduino board. The custom-built board contains the STM32 microcontroller family based on the ARM Cortex-M processor architecture. These microcontrollers combine high performance, low power consumption, and a wide range of integrated peripherals and features, making them suitable for a wide variety of embedded applications. For a signal generation, Pulse Width Modulation (PWM) with a low pass filter is integrated into the custom-built board. In this way, a powerful technique for controlling the parameters of the generated signal is obtained, as it allows for precise and efficient control. A low-pass filter removes the high-frequency components and smooths out the signal. PWM is a method of controlling the power delivered to a load by modulating the width of a pulse of constant amplitude and frequency. By changing the duty cycle of the pulse, the effective voltage or current delivered to the load can be varied [35–37].

An electrodynamic actuator was used to generate an input signal as a short impulse. The electronic system provides measurements taken in six-dimensional space using two 6D sensors, coaxially positioned on the beams on either side of the joint. A crucial aspect in placing the sensors and the electrodynamic actuator is ensuring the sensors' symmetrical positioning on both sides of the joint and aligned with its axis. Electronic system improvements allowed processing response signals from a wider frequency range and simplified the data collecting process. The impulse is sent many times, and the response data F1 and F2 from the first and second sensors are collected and averaged. Averaged data is saved for further post-processing, and the procedure is repeated for the medicated object of investigation.

The signal analysis software package with a wide range of powerful tools and statistics functions, SIGVIEW, is used to post-process collected data. The processing of the collected data F1 and F2 in the time domain includes:

1. Remove the constant offset from F1 and F2 by subtracting the signal's mean value from all the amplitude values. The result is a signal with a mean equal to zero;
2. Make the normalisation of concatenated pairs of responses F1 and F2 to ensure a mutual comparison of the obtained data under the conditions of the experiment with artificial degradation of the connection;
3. Choose the frequency range in which the object's behaviour under study will be observed based on the spectrum analysis;
4. Split the filtered concatenated signal into two signals, F1* and F2*;

5. Convolve the obtained normalised pairs of signals F1* and F2* from both sensors to characterise the degree of similarity between the two signals.;
6. Determine the root mean square (RMS) value from the obtained signals convolution as a measure of the similarity between two signals.

Schematically, the post-processing process is shown in Figure 3.

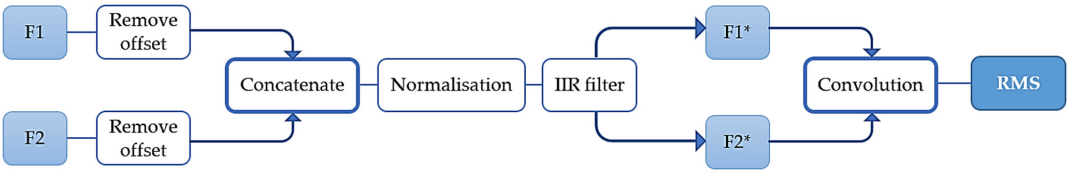


Figure 3. Post-processing scheme of the collected specimen raw response data F1 and F2 from the first and second sensors to the processed specimen response signals F1* and F2* for their further similarity comparison by convolution and RMS.

The obtained step six parameter RMS is proposed for monitoring the system's condition during operation as a reference point using determined parameters at the initial stage, with an approved design stiffness condition of the system.

2.2. Verification Approach

The steel beam specimen with splice connection was prepared (Figure 4) to check the possibility of damage detection of bolted splice connection by coaxial accelerations correlation.

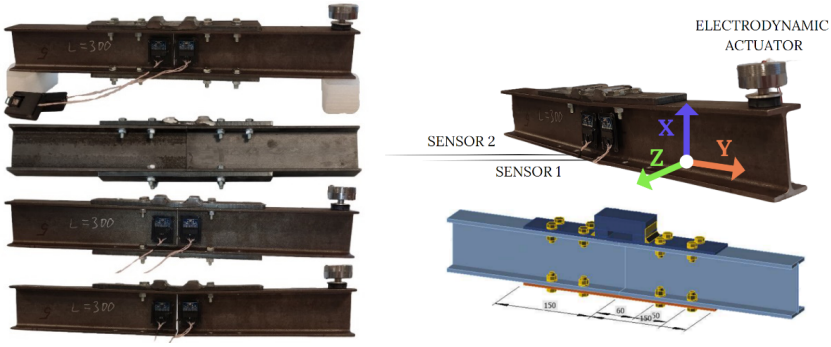


Figure 4. Prepared steel specimens with different numbers of bolts, placement of sensors and electrodynamic actuator, and the axis of the specimen.

The investigated steel specimen consisted of S355 strength class parallel flange I section IPE 80 steel beam elements with dimensions according EN 10365, where the height is 80 mm, the width is 46 mm, the web thickness is 3.8 mm, the flange thickness is 5.2 mm and the root fillet radius is 5.0 mm. A total length of the specimen is 600 mm that had been halved and joined using two metal plates with dimensions of 46 mm × 300 mm and thicknesses of 8 mm. One metal connector plate is positioned on the top face and the other on the bottom face of the specimen. The connection between the steel beam and steel plates was established using 8.8-grade M8 bolts. The positioning of holes for bolts is adopted following the requirements of the Eurocode EN 1993-1-8 of minimum and maximum spacing and end and edge distances for bolts. Since shear resistance of the bolts is decisive, the distance between the bolts is not essential and is not assumed as a variable for this test. The joint was investigated using varying numbers of bolts—16, 12, 8 and 4. In the case of 4 bolts, the bottom metal connector plate was removed. The degradation of a

connection during operation has been artificially characterized by unbolting the bolts and removing the metal connector plate. Structural joint degradation can occur due to factors such as loosening of the bolts and/or corrosion. The order of unbolting was as follows: first, the 4 bottom bolts were unbolted, 2 edge bolts on each side of the joint; second, the 4 top bolts were unbolted, and 2 edge bolts on each side of the joint; finally, the last 4 bottom bolts were unbolted, and the bottom metal plate was removed.

Unbolting bolts allowed adjustments to the joint's stiffness to be made and analysed using the proposed coaxial correlation method. During the experiment, constant support conditions for the specimen are provided: simply supported (roller-roller) on vibration-absorbing supports with a span of 500 mm.

The structural joint model is created using 3D modelling software Tekla Structures in accordance with the European standard EN 1993-1-8, which outlines the general principles and rules for designing joints in steel structures. Once the joint model is prepared, it is exported from Tekla Structures to IDEA StatiCa and analysed using the finite element analysis (FEA) method.

To accurately model the joint, both the webs and flanges of connected members as well as metal connector plates are modelled using 4-node quadrangle shell elements with nodes at each corner. The size of the finite elements varies from 5 to 10 mm, and the meshing is done automatically. Fasteners, such as bolts, are modelled using special FEM components.

The steel joint is analysed using a nonlinear, elastic-plastic material model. After conducting the calculations, the maximum value of the bending moment that the specimen can withstand is determined. In this case, with all 16 bolts, in a three-point bending configuration, the specimen is treated as a simply supported beam with a span of 500 mm. Based on the calculations, the maximum value of the bending moment that the specimen can absorb is determined to be equal to 4.75 kNm.

The vibration load was generated by an electrodynamic actuator mounted on one end of the beam coaxially to the X-axis of the specimen. The structure's response was measured in three directions, namely, X, Y, and Z (see Figure 4), using two 3D accelerometers and around three axes, namely, GX, GY, and GZ, using two 3D gyroscopes, thus providing 6D space measurements. Next, 6D sensors 1 and 2 were coaxially placed on the beams on either side of the beam splice connection. The process of specimen testing is shown in Figure 5. The obtained signals were transmitted to a computer with corresponding software for further processing.

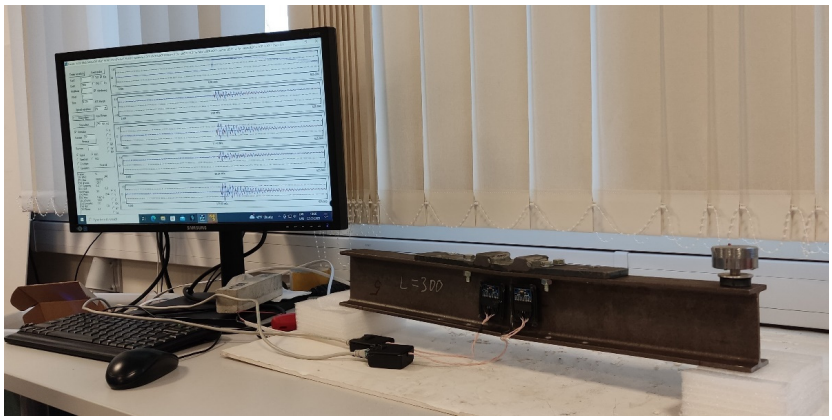


Figure 5. The process of specimen testing.

3. Results and Discussion

The vibration tests were conducted to assess the effectiveness of the coaxial acceleration correlation technique in detecting changes in joint stiffness in steel beam splice connections.

In order to simulate a reduction in joint stiffness, the bolts were gradually unbolted. These tests aimed to confirm whether the technique could accurately identify variations in joint stiffness. The results of the tests provided valuable insights into the method's performance and potential applications in structural joints.

The averaging function was applied to response records from coaxially placed 6D sensors to obtain accurate data. This function helped minimise the effects of external noise or vibration on the measurements. The collected response records in 6 different axes for specimen with 16 bolts are summarised in Figure 6. The values on the y-axis in Figure 6 represent the amplitude of the signal data received from the ADC device. These values are not physical units, but rather arbitrary units used to represent the signal amplitude. The ADC device converts the continuous analog signal into a discrete digital signal by sampling it at specific intervals and assigning numeric values to each sample. Each sample represents the amplitude of the signal at that specific point in time, and the numeric value assigned to it is a measure of the amplitude of the signal. In the case of the sound card, each sample has a value between −32,767 and 32,767, which represents the maximum and minimum amplitude of the signal that can be recorded with 16-bit resolution.

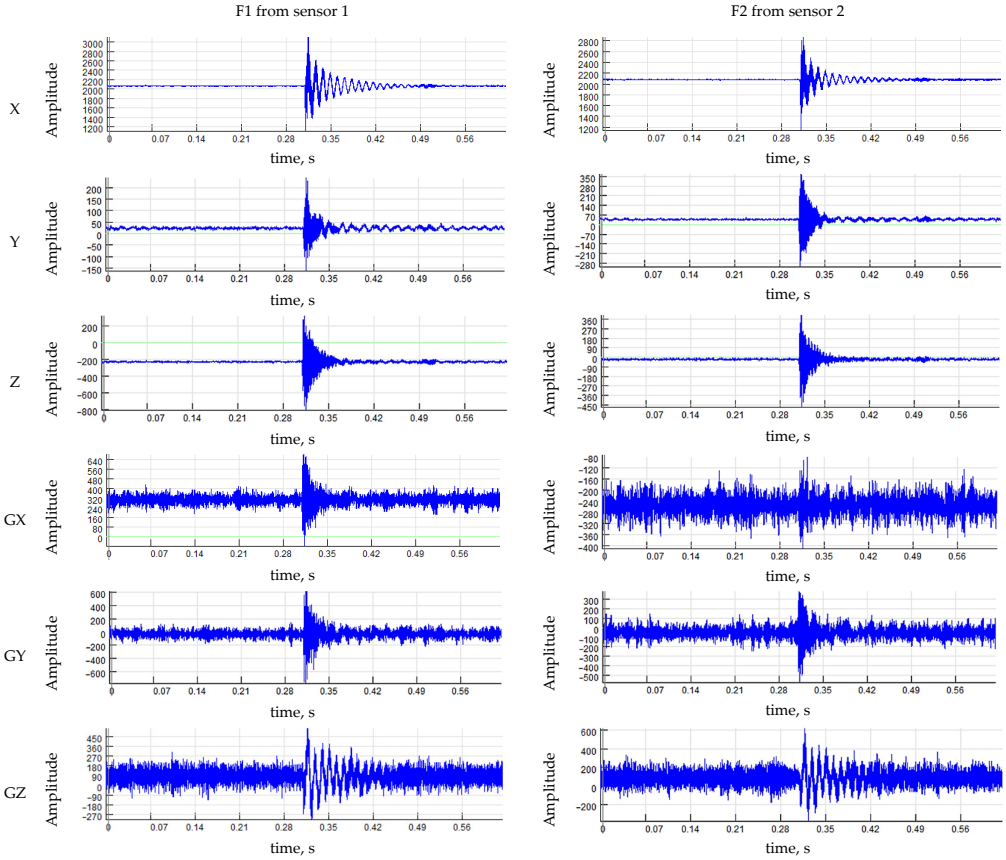


Figure 6. Collected response signals F1 and F2 for the specimen with 16 bolts in 6 axes, where the y-axis represents the amplitude of the signal in the arbitrary units assigned by the ADC device to each sample and x-axis represents the duration of the signal in seconds.

After removing the constant offset from F1 and F2, the signals are concatenated in the new signal and normalised. Based on the spectrum analysis (Figure 7), which represents the amplitude of the signal at each frequency component, the region of second pronounced peak is selected for further analysis. Infinite Impulse Response (IIR) filter with band-pass from 1200 Hz to 1800 Hz is used. The amplitude units on the y-axis of the spectrum are dependent on the units of the original signal recorded by the ADC device. As the original signal was recorded in arbitrary units, then the amplitude units of the spectrum are also in arbitrary units.

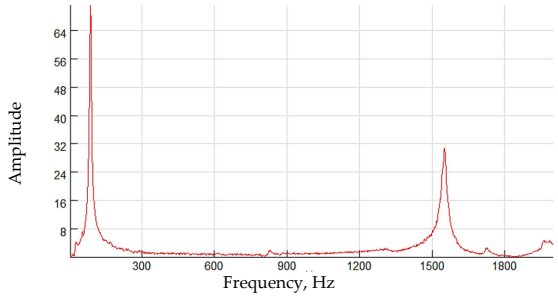


Figure 7. Fast Fourier transform spectrum for specimen with 16 bolts obtained from F1 in X-axis direction, which represents the amplitude of the signal in arbitrary units at each frequency component.

The split signals F1* and F2* after the IIR filter are shown in Figure 8.

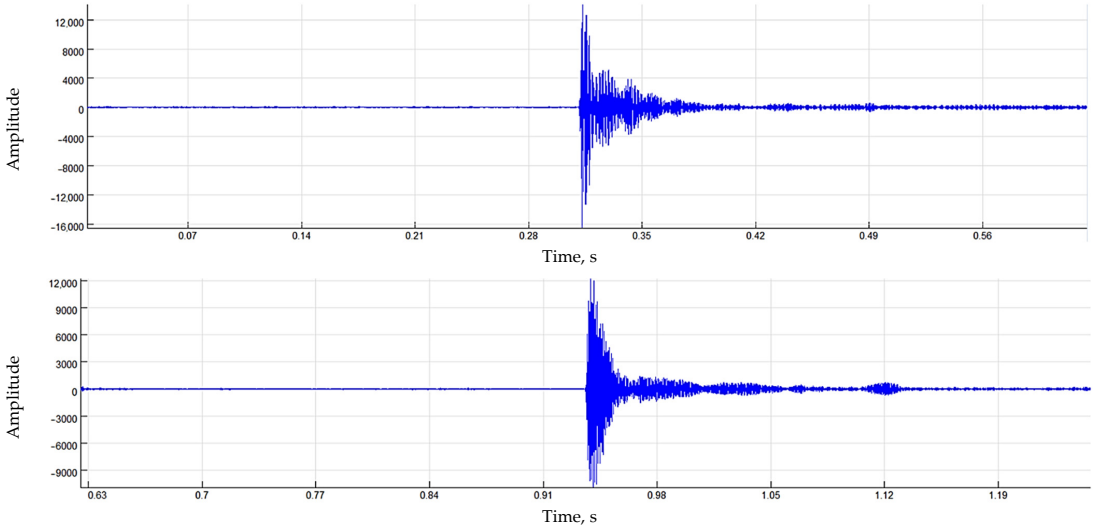


Figure 8. Processed response signals F1* and F2* for the specimen with 4 bolts, where the y-axis represents the amplitude of the signal in the arbitrary units assigned by the ADC device to each sample, after signal pairs normalisation ranging from −32,767 to 32,767 and x-axis represents the duration of the signal in seconds.

Obtained product of convolution in the X-axis direction, which combines the pair of signals from both sensors and characterises the degree of similarity between two signals for four grades of joint stiffness, is shown in Figure 9.

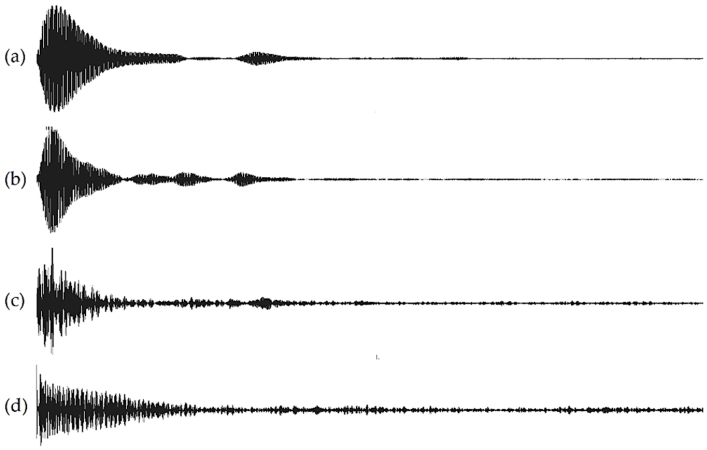


Figure 9. Convolution of two X-axis measured and processed signals F1* and F2* for splice connection: (**a**) with 16 bolts, (**b**) with 12 bolts, (**c**) with 8 bolts, (**d**) with 4 bolts.

As can be seen from Figure 9, as the degree of joint degradation develops, its convolution shape changes. The representation of the convolutional signal becomes noisier as the joint degrades. As a convolution is integral that expresses the amount of overlap of one signal as it is shifted over another signal, it can be argued that as the joint degrades, the similarity of response signals from coaxially placed sensors on each side of the joint decreases. Quantitatively, this change can be expressed by the RMS of the convolution signal. RMS values of signals F1* and F2* and their convolution as a percentage from the corresponding maximal value are summarised in Figure 10.

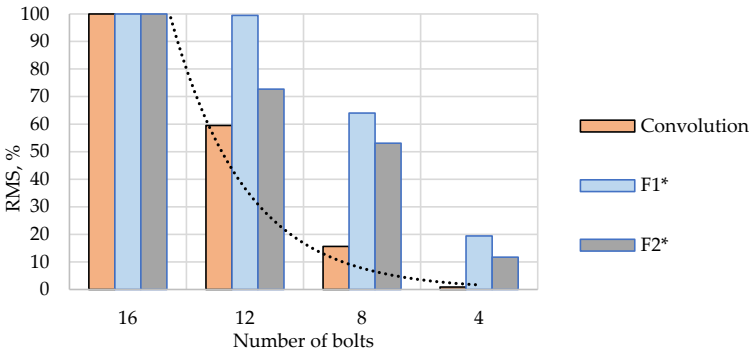


Figure 10. Calculated root mean square (RMS) values for response signals F1* and F2* in the X-axis direction and its convolution for different grades of joint stiffness as a percentage from the RMS maximal value of corresponding signal.

It can be seen from Figure 10 that the RMS of sensors' signals cannot provide a sufficient description of the joint stiffness grade. In the case of sensor 1, the difference between RMS for the joint with 16 bolts and 12 bolts is equal only to 0.6%. In the case of convolution of two coaxially collected signals, the RMS of convolution clearly shows a direct correlation between the calculated RMS value and the stiffness grades of the steel beam splice joint. The sensitivity of this parameter to changes in stiffness is high enough to be safe for a joint stiffness evaluation. These findings suggest that the coaxial correlation method with RMS of convolution signal can be used as indicators of joint stiffness in steel beam splice connections, providing valuable insights into the behaviour of these connections.

Figure 11 summarises the RMS values of convolution signals in 6D space. For the investigated type of splice joint, the RMS of convolution shows a direct correlation between the calculated RMS value and the stiffness grades of the joint in the X, Y and GY axes directions. In the GX axis, the obtained difference in RMS value for joints with 12, 8 and 4 bolts are not so pronounced for convenient and certain evaluation of joint stiffness. In the Z-axis direction, the increased RMS value was reached at a higher degree of joint degradation when the bottom metal plate was removed, and only the top 4 bolts were left. In the GZ axis, direction obtained data is not informative.

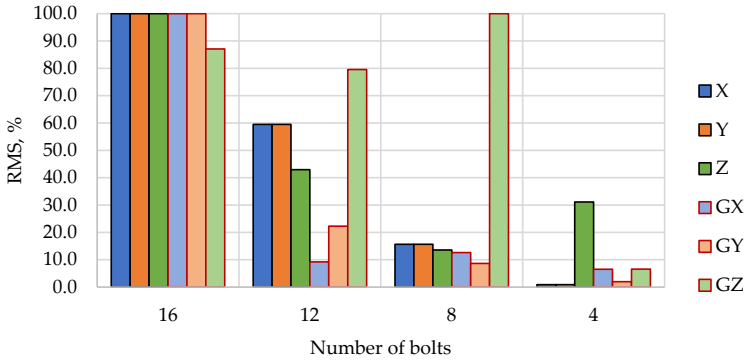


Figure 11. Calculated root mean square (RMS) values for convolution in 6D space for different grades of joint stiffness as a percentage from the RMS maximal value in corresponding axis direction.

So, it can be concluded that the nature of the RMS during the degradation of the joint may change in different axes. If, in the case of simple joints, it is possible to predict which axes are better to investigate, then in the case of complex joints, wrongly chosen axes may lead to wrong conclusions regarding the state of the investigated joint. Therefore, the relationships obtained with the simple splice joint considered in this work confirm the usefulness of 6D measurements and increase the reliability of the interpretation of quality assessment of structural joints.

4. Conclusions

The novel method of coaxial correlation in 6D space for quality assessment of moment-resisting structural joints, including a system response analysis method with coaxially placed 6D sensors on either side of the joint and electronic system, is proposed. The improvements of the initial version of the coaxial correlation method provide the possibilities of:

- Determining linear accelerations and angular velocities, thus providing a measurement option in 6D space;
- Analysing at frequencies higher than 500 Hz, which is essential to ensure the possibility of studying the prototype of the structural joint in laboratory conditions;
- Processing data in the time domain thanks to synchronisation between the input signal and system responses;
- Using even weak input signal thanks to averaging system response.

The developed approach of collected data post-processing using convolution signals from both sensors makes it possible to estimate damage or degradation of the structural joint during its operation both visually by changes in the appearance of the convolution signal and also quantitatively by the suggested RMS value. Measurements in 6D space provide the reliability of the result interpretation. Mostly direct correlation between the calculated RMS values of convolution signals and the stiffness grades of the structural joint is obtained during the verification of the proposed method. It means that as the stiffness of the moment-resisting structural joint decreases, the similarity of the response signals from both sides of the joint also decreases. The results obtained from testing the

proposed method on a simple model with a bolted joint demonstrate that the method can be effectively used to assess the quality of moment-resisting joints. Moreover, this method shows promise as a solution for assessing more complex joints, as well as welded joints.

Author Contributions: Conceptualisation, V.K., K.B.-V. and D.S.; methodology, K.B.-V. and V.K.; software, V.K.; investigation, V.K. and K.B.-V.; data curation, K.B.-V. and V.K.; writing—original draft preparation, K.B.-V. and D.S.; writing—review and editing, K.B.-V., V.K. and D.S.; visualisation, K.B.-V. and D.S.; project administration, D.S. All authors have read and agreed to the published version of the manuscript.

Funding: This research was supported by the Latvian Council of Science funded project "Method of Correlation of Coaxial Accelerations in 6D Space for Quality Assessment of Structural Joints (COACCEL)" (Nr. lzp-2020/1-0240).



Data Availability Statement: The data that support the findings of this study are available from the corresponding author [K.B.-V.] upon request.

Acknowledgments: The authors would like to thank Andrejs Podkoritovs for providing the design of the connection and UPB Group company for manufacturing the specimens.

Conflicts of Interest: The authors declare no conflict of interest.

References

1. Korkmaz, H.H.; Dere, Y.; Özkılıç, Y.O.; Bozkurt, M.B.; Ecemiş, A.S.; Özdoner, N. Excessive Snow Induced Steel Roof Failures in Turkey. *Eng. Fail. Anal.* **2022**, *141*, 106661. [CrossRef]
2. Korkmaz, H.H.; Yakut, A.; Bayraktar, A. Analysis of a Multi-Story Reinforced Concrete Residential Building Damaged under Its Self-Weight. *Eng. Fail. Anal.* **2019**, *98*, 38–48. [CrossRef]
3. Krentowski, J.R.; Knyziak, P.; Mackiewicz, M. Durability of Interlayer Connections in External Walls in Precast Residential Buildings. *Eng. Fail. Anal.* **2021**, *121*, 105059. [CrossRef]
4. Šabatka, L.; Kolaja, D.; Vild, M.; Wald, F.; Kuříková, M.; Kabeláč, J. Influence of Joint Stiffness on Design of Steel Members. In *Advances and Trends in Engineering Sciences and Technologies III*; CRC Press: Boca Raton, FL, USA, 2019; ISBN 978-0-429-02159-6.
5. Ngo, T.; Pham, T.; Hao, H. Ductile and Dry Exterior Joints Using CFRP Bolts for Moment-Resisting Frames. *Structures* **2020**, *28*, 668–684. [CrossRef]
6. Özkılıç, Y.O. Cyclic and Monotonic Performance of Unstiffened Extended End-Plate Connections Having Thin End-Plates and Large-Bolts. *Eng. Struct.* **2023**, *281*, 115794. [CrossRef]
7. Mashaly, E.; El-Heweity, M.; Abou-Elfath, H.; Osman, M. Behavior of Four-Bolt Extended End-Plate Connection Subjected to Lateral Loading. *Alex. Eng. J.* **2011**, *50*, 79–90. [CrossRef]
8. Steneker, P.; Wiebe, L.; Filiatrault, A. Steel Moment Resisting Frames with Sliding Hinge Joint Connections: Seismic Evaluation Using Various Response Indices. In Proceedings of the 12th Canadian Conference on Earthquake Engineering (12CCEE), Quebec City, QC, Canada, 17–20 June 2019; Available online: https://research.iusspavia.it/handle/20.500.12076/5694 (accessed on 12 April 2023).
9. Lemonis, M. Steel Moment Resisting Frames with Both Joint and Beam Dissipation Zones. *J. Constr. Steel Res.* **2018**, *147*, 224–235. [CrossRef]
10. *An Overview of the Connection Classification Index*; The Hong Kong Institute of Steel Construction: Honolulu, HI, USA, 2019.
11. Boscato, G.; Fragonara, L.Z.; Cecchi, A.; Reccia, E.; Baraldi, D. Structural Health Monitoring through Vibration-Based Approaches. *Shock Vib.* **2019**, *2019*, 2380616. [CrossRef]
12. Opazo-Vega, A.; Benedetti, F.; Nuñez-Decap, M.; Maureira-Carsalade, N.; Oyarzo-Vera, C. Non-Destructive Assessment of the Elastic Properties of Low-Grade CLT Panels. *Forests* **2021**, *12*, 1734. [CrossRef]
13. Gaile, L.; Ratnika, L.; Pakrastins, L. RC Medium-Rise Building Damage Sensitivity with SSI Effect. *Materials* **2022**, *15*, 1653. [CrossRef]
14. Park, H.S.; Oh, B.K. Real-Time Structural Health Monitoring of a Supertall Building under Construction Based on Visual Modal Identification Strategy. *Autom. Constr.* **2018**, *85*, 273–289. [CrossRef]
15. Varanis, M.; Silva, A.L.; Mereles, A.G. On Mechanical Vibration Analysis of a Multi Degree of Freedom System Based on Arduino and MEMS Accelerometers. *Rev. Bras. Ensino Física* **2017**, *40*, e1304. [CrossRef]
16. Li, W.; Guo, S.; Liu, Y.; Shen, Z.; Xiong, Y.; Gao, F.; Hughes, D.J.; Lin, J. Structure Health Monitoring of Composites Joint Reinforced by Acoustic Emission Based Smart Composite Fasteners. *Compos. Commun.* **2022**, *33*, 101213. [CrossRef]

17. Zhu, L.; Fu, Y.; Chow, R.; Spencer, B.F.; Park, J.W.; Mechitov, K. Development of a High-Sensitivity Wireless Accelerometer for Structural Health Monitoring. *Sensors* **2018**, *18*, 262. [CrossRef]
18. Wu, T.; Liu, G.; Fu, S.; Xing, F. Recent Progress of Fiber-Optic Sensors for the Structural Health Monitoring of Civil Infrastructure. *Sensors* **2020**, *20*, 4517. [CrossRef]
19. Muttillo, M.; Stornelli, V.; Alaggio, R.; Paolucci, R.; Di Battista, L.; de Rubeis, T.; Ferri, G. Structural Health Monitoring: An IoT Sensor System for Structural Damage Indicator Evaluation. *Sensors* **2020**, *20*, 4908. [CrossRef]
20. Sulaiman, M.S.A.; Yunus, M.A.; Bahari, A.R.; Rani, M.N.A. Identification of Damage Based on Frequency Response Function (FRF) Data. *MATEC Web Conf.* **2017**, *90*, 01025. [CrossRef]
21. Zhan, J.; Zhang, F.; Siahkouhi, M. A Step-by-Step Damage Identification Method Based on Frequency Response Function and Cross Signature Assurance Criterion. *Sensors* **2021**, *21*, 1029. [CrossRef]
22. Buka-Vaivade, K.; Gaile, L.; Serdjuks, D.; Tatarinovs, A.; Pakrastins, L. Non-Destructive Quality Control of the Adhesive Rigid Timber-to-Concrete Connection in TCC Structures. *Buildings* **2022**, *12*, 2151. [CrossRef]
23. Tol, Ş.; O¨zgu¨ven, H.N. Dynamic Characterization of Bolted Joints Using FRF Decoupling and Optimization. *Mech. Syst. Signal Process.* **2015**, *54*, 124–138. [CrossRef]
24. Wang, X. Chapter 1—Analysis of a Single Degree of Freedom Spring-Mass-Dashpot System Using Transfer Function, Integration, State Space, and Frequency Response Methods. In *Frequency Analysis of Vibration Energy Harvesting Systems*; Wang, X., Ed.; Academic Press: Cambridge, MA, USA, 2016; pp. 1–13. ISBN 978-0-12-802321-1.
25. Gomez-Cabrera, A.; Escamilla-Ambrosio, P.J. Review of Machine-Learning Techniques Applied to Structural Health Monitoring Systems for Building and Bridge Structures. *Appl. Sci.* **2022**, *12*, 10754. [CrossRef]
26. Zajam, S.; Joshi, T.; Bhattacharya, B. Application of Wavelet Analysis and Machine Learning on Vibration Data from Gas Pipelines for Structural Health Monitoring. *Procedia Struct. Integr.* **2019**, *14*, 712–719. [CrossRef]
27. Izham, M.H.N.; Sani, M.S.M.; Abdul Rani, M.N.; Yunus, M.A. Damage Assessment on Frame Structure with Bolted Joints Based on Experimental Modal Analysis. *IOP Conf. Ser. Mater. Sci. Eng.* **2019**, *469*, 012102. [CrossRef]
28. Nguyen, K.-D.; Chan, T.H.; Thambiratnam, D.P.; Nguyen, A. Damage Identification in a Complex Truss Structure Using Modal Characteristics Correlation Method and Sensitivity-Weighted Search Space. *Struct. Health Monit.* **2019**, *18*, 49–65. [CrossRef]
29. Nguyen, T.H.A. Vibration Testing for Dynamic Properties of Building Floors. *IOP Conf. Ser. Mater. Sci. Eng.* **2020**, *869*, 052005. [CrossRef]
30. Knak, M.; Wojtczak, E.; Rucka, M. Non-Destructive Diagnostics of Concrete Beams Strengthened with Steel Plates Using Modal Analysis and Wavelet Transform. *Materials* **2021**, *14*, 3014. [CrossRef]
31. Serdjuks, D.; Kurtenoks, V.; Tatarinovs, A.; Mironovs, V.; Lapkovskis, V.; Buka-Vaivade, K.; Macevics, A.; Topcijs, K.; Vilnitis, M. Method of Coaxial Accelerations Correlation for Quality Assessment of Structural Joints. *Procedia Struct. Integr.* **2022**, *37*, 547–554. [CrossRef]
32. Serdjuks, D.; Kurtenoks, V.; Tatarinovs, A.; Buka-Vaivade, K.; Lapkovskis, V.; Mironovs, V.; Podkoritovs, A.; Topcijs, K. Non-Model Vibration Analysis Method for Health Monitoring of Structural Joints. *Procedia Struct. Integr.* **2022**, *37*, 555–562. [CrossRef]
33. Ravanshad, N.; Rezaee-Dehsorkh, H. Chapter 12—Level-Crossing Sampling: Principles, Circuits, and Processing for Healthcare Applications. In *Compressive Sensing in Healthcare*; Khosravy, M., Dey, N., Duque, C.A., Eds.; Advances in Ubiquitous Sensing Applications for Healthcare; Academic Press: Cambridge, MA, USA, 2020; pp. 223–246.
34. Mark, H.; Workman, J. Chapter 102—Calibration Transfer, Part 2: The Instrumentation Aspects. In *Chemometrics in Spectroscopy*, 2nd ed.; Mark, H., Workman, J., Eds.; Academic Press: Cambridge, MA, USA, 2018; pp. 751–764. ISBN 978-0-12-805309-6.
35. Christ, R.D.; Wernli, R.L. Chapter 7—Power and Telemetry. In *The ROV Manual*, 2nd ed.; Christ, R.D., Wernli, R.L., Eds.; Butterworth-Heinemann: Oxford, UK, 2014; pp. 141–161. ISBN 978-0-08-098288-5.
36. Ibrahim, D. Chapter 8—Advanced PIC32 Projects. In *Designing Embedded Systems with 32-Bit PIC Microcontrollers and MikroC*; Ibrahim, D., Ed.; Newnes: Oxford, UK, 2014; pp. 359–442. ISBN 978-0-08-097786-7.
37. Pyeatt, L.D.; Ughetta, W. Chapter 11—Devices. In *ARM 64-Bit Assembly Language*; Pyeatt, L.D., Ughetta, W., Eds.; Newnes: Oxford, UK, 2020; pp. 405–444. ISBN 978-0-12-819221-4.

Disclaimer/Publisher's Note: The statements, opinions and data contained in all publications are solely those of the individual author(s) and contributor(s) and not of MDPI and/or the editor(s). MDPI and/or the editor(s) disclaim responsibility for any injury to people or property resulting from any ideas, methods, instructions or products referred to in the content.

Kurtenoks V., Kurajevs A., Buka-Vaivade K., Serdjuks D., Lapkovskis V., Mironovs V., Podkoritovs A., Vilnitis M.

The quality assessment of timber structural joints using the coaxial correlation method.

Buildings, 2023, 13(8), 1929.

https://doi.org/10.3390/buildings13081929

buildings

MDPI

Article

The Quality Assessment of Timber Structural Joints Using the Coaxial Correlation Method

Viktors Kurtenoks [1], Aleksis Kurajevs [1], Karina Buka-Vaivade [1,*], Dmitrijs Serdjuks [1], Vjaceslavs Lapkovskis [1], Viktors Mironovs [2], Andrejs Podkoritovs [1] and Martins Vilnitis [2]

[1] Institute of Structural Engineering, Riga Technical University, LV-1048 Riga, Latvia; viktors.kurtenoks@rtu.lv (V.K.); aleksis.kurajevs@gmail.com (A.K.); dmitrijs.serdjuks@rtu.lv (D.S.); vjaceslavs.lapkovskis@rtu.lv (V.L.); andrejs.podkoritovs@rtu.lv (A.P.)

[2] Institute of Construction Technology, Riga Technical University, LV-1048 Riga, Latvia; viktors.mironovs@rtu.lv (V.M.); martins.vilnitis@rtu.lv (M.V.)

* Correspondence: karina.buka-vaivade@rtu.lv

Abstract: With the growing popularity of timber structures, the requirement for reliable and non-destructive methods to assess the quality and condition of structural joints becomes increasingly essential. A novel coaxial correlations method is investigated to assess the degradation of panel-to-panel moment joints in timber structures. The method involves analysing the response data obtained from accelerometers placed on both sides of the joint and comparing the readings to evaluate the joint's condition. A specific joint solution to simulate the degradation of the moment joint in laboratory conditions is selected based on its simplicity and the ease with which its degradation can be simulated. The joint consists of angle brackets joined with timber screws and bolts to plywood panels. Gradually unscrewing the timber screws reduces the joint's stiffness to simulate wear and tear over time. The experimental setup includes static loading and finite element modelling (FEM) to determine the rotational stiffness of the investigated joint at each degradation level. A dynamic experiment using vibration loading with sweep signal in the frequency range of 10 Hz to 2000 Hz is conducted to assess the quality of the joint. The conducted research provides valuable insights into the behaviour of timber panel-to-panel connections. The findings highlight the relationship between joint stiffness, vertical displacements, and the proposed dimensionless parameter, volume root mean square value (RMS_{vol}), which offers a more comprehensive assessment of the joint's condition in three spatial directions. As a result of the research, it has been established that, in the case of linear-type connections, unlike point-type joints, there is a possibility of signal scattering, so it is recommended that power comparisons and evaluations of the response signals from both accelerometers at the initial stage of applying the coaxial correlations method are performed.

Keywords: non-destructive test; dynamic response; structural joints; coaxial accelerations; structural health monitoring; timber structures; vibration test; rotational stiffness

check for updates

Citation: Kurtenoks, V.; Kurajevs, A.; Buka-Vaivade, K.; Serdjuks, D.; Lapkovskis, V.; Mironovs, V.; Podkoritovs, A.; Vilnitis, M. The Quality Assessment of Timber Structural Joints Using the Coaxial Correlation Method. *Buildings* **2023**, *13*, 1929. https://doi.org/10.3390/buildings13081929

Academic Editor: Egidio Lofrano

Received: 30 June 2023
Revised: 26 July 2023
Accepted: 27 July 2023
Published: 28 July 2023

Copyright: © 2023 by the authors. Licensee MDPI, Basel, Switzerland. This article is an open access article distributed under the terms and conditions of the Creative Commons Attribution (CC BY) license (https://creativecommons.org/licenses/by/4.0/).

1. Introduction

Timber structures have gained significant attention recently due to their sustainable and environmentally friendly nature [1–3]. Buildings and construction account for approximately 40% of global energy consumption and contribute 33% of greenhouse gas emissions [4]. With the growing interest in sustainable construction practices, timber has emerged as a viable alternative to conventional building materials. Timber offers numerous advantages, such as a low carbon footprint, renewable resource availability, and aesthetic appeal [5,6]. As a result, the use of timber in construction has witnessed a resurgence, with an increasing number of multi-story timber buildings being designed and built [7,8].

However, ensuring timber structures' structural integrity and long-term performance presents unique challenges [9,10]. Timber is susceptible to various degradation mechanisms, including moisture, fungal decay, and mechanical damage, which can compromise strength

and stiffness [11,12]. Therefore, the quality control of timber structures is of the utmost importance to ensure their safety, durability, and reliability throughout their service life.

Traditionally, quality control in timber structures has relied on destructive testing methods, which involve extracting samples or subjecting the structure to load tests until failure. While these methods provide valuable information, they are invasive, time-consuming, and expensive. Moreover, destructive testing is not feasible for in-service structures or those with complex joint configurations.

Non-destructive quality control methods have emerged as a promising alternative to overcome these limitations. Non-destructive testing (NDT) techniques allow for the evaluation of structural conditions without causing damage to the timber elements or the overall structure [13]. NDT methods enable timely and cost-effective assessment of civil engineering structures, facilitating preventive maintenance, timely repairs, structural health monitoring, and the determination of the residual resources of buildings [14,15].

Various techniques have been employed to evaluate timber structures in the field of non-destructive quality control. These techniques include visual inspection, ultrasound testing, infrared thermography, acoustic emission, resistography, moisture-content tests, vibration-based methods, and others [16–20]. Each technique offers unique advantages and limitations, and their effectiveness depends on factors such as the type of defect, accessibility, and the size and configuration of the timber elements.

Among the non-destructive techniques, vibration-based methods have gained prominence due to their sensitivity to changes in stiffness and dynamic characteristics of the structure [14,21–23]. Vibration-based methods involve exciting the structure with a known input signal and analysing the response to extract information about its stiffness, damping, and natural frequencies. By monitoring changes in the structure's dynamic behaviour, it is possible to identify defects, degradation, and changes in the mechanical properties of timber elements.

A growing interest has recently arisen in developing non-destructive quality control methods tailored explicitly for timber structures [24,25]. Researchers have focused on investigating the behaviour of timber connections, which play a critical role in the overall performance and stability of timber structures [8,11,26,27]. The stiffness of a joint directly influences how internal forces and deformations are distributed within a structure [28,29]. The joints in timber structures are typically classified as pinned or moment joints (Figure 1). Understanding the degradation mechanisms and evaluating the condition of timber connections is essential for ensuring the safety and reliability of the entire structure.

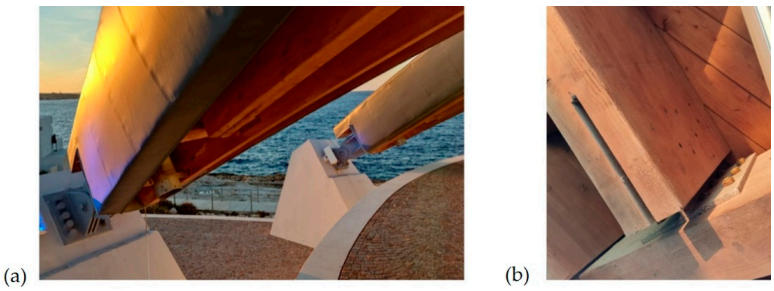


Figure 1. Joints of timber structural members: (**a**) pinned joint, (**b**) moment joint.

This study presents a novel non-destructive evaluation method, the coaxial correlations method, for assessing the degradation of panel-to-panel moment joints in timber structures. By incorporating static loading, finite element modelling (FEM), and dynamic vibration testing, the authors aim to simulate and assess the behaviour of panel-to-panel moment joints under varying degradation levels.

The proposed method offers several advantages over existing techniques, comprehensively assessing the joint's condition in three spatial directions. Using vibration-based

methods combined with numerical modelling enhances the understanding of the joint's stiffness, displacements, and the proposed dimensionless parameter, volume root mean square value (RMS_{vol}). These findings contribute to more accurately evaluating the quality and integrity of panel-to-panel moment joints in timber structures.

Overall, this study contributes to the growing body of research on non-destructive quality control methods for timber structures and provides valuable insights into the behaviour of timber connections. By offering a non-invasive and efficient approach to assess the quality of structural joints, the coaxial correlations method can potentially improve the safety and durability of timber structures, thus promoting their wider adoption in sustainable construction practices.

2. Materials and Methods

2.1. Choice of the Object of Investigation

This study focused on simulating real timber structure connections without destructive testing methods [30]. A panel-to-panel moment joint consisting of steel angles joined with timber screws and bolts to plywood panels was carefully selected as the subject of investigation. This joint solution was chosen for its simplicity and the ease with which the degradation of a moment-resisting connection in timber multi-storey buildings can be replicated under laboratory conditions. By loosening bolts, we can effectively reduce the joint's stiffness and emulate the behaviour during the degradation of a moment-resisting joint, such as the wall-to-floor panel connection in timber multi-storey buildings.

The objective was to create a versatile joint configuration capable of absorbing a wide range of bending moments, allowing for various adjustment possibilities. The experiment involves designing and fabricating a specialised testing stend specifically tailored to simulate the behaviour of multi-storey timber floor structures at various degrees of joint degradation. This stend incorporates the selected adjustable panel-to-panel moment joint (Figure 2). The range of adjustment possibilities allows us to evaluate the joint's performance under various loading conditions, making the findings more applicable to diverse timber construction scenarios. This approach of simulating joint degradation by loosening bolts eliminates the need for destruction and provides a controlled and replicable environment for studying joint behaviour over time.

The stend consists of two Riga Ply plywood panels of grade IV according to EN 635-2 with dimensions of 1250 mm × 400 mm and a thickness of 18 mm and additional timber supports. Riga Ply, produced by Latvijas Finieris Group, comprises 13 cross-bonded birch veneer layers. Additional timber supports play a vital role in ensuring the stability of both the vertical plywood panel and the vertical support under the free-end connection of the horizontal plywood panel. The timber supports provide the possibility to represent investigated connection as analogous to the connection between a wall and floor panel in a larger structure. By incorporating the additional timber supports, the stend is fortified against unwanted movements that may arise due to its relatively small size. These supports effectively minimise potential structural instabilities, making the stend more robust and reliable.

The experimental setup includes two types of connections shown in Figure 2a: a free-end connection (B) and a panel-to-panel moment joint (A). The free-end connection allows for the vertical (Z-axis) and longitudinal (X-axis) movements of the plywood panel while preventing transversal (Y-axis) movements with steel plates on both sides of the connection. The moment joint is made of angle brackets with dimensions 70 mm × 55 mm × 2 mm, and Fortis-produced fasteners—timber screws and bolts following the European standard EN 1995-1-1, which outlines the general principles and rules for designing joints in timber structures. Angle brackets produced by Arras CF are one-piece non-welded three-dimensional nailing plates designed for use in timber-to-timber connections. Used angle brackets are made from pre-galvanised steel DX51D + Z275 according to EN 10346:2015, with a steel yield strength of at least 250 MPa and tensile strength of at least 330 MPa. The angle brackets are placed in two rows at the top and bottom of the horizontal panel, with

6 pieces on each side. M2.5 timber screws with a length of 15 mm are used to fasten each row of angle brackets to the vertical plywood panel. We use 8.8-grade M10 hexagon head bolts with thread up to the head, a tensile strength of at least 800 MPa, and a yield strength of at least 640 MPa to connect the angle brackets and the horizontal plywood panel. The total amount of used fasteners is 9 timber screws per one steel angle row (18 timber screws in total for investigated connection) and 6 bolts.

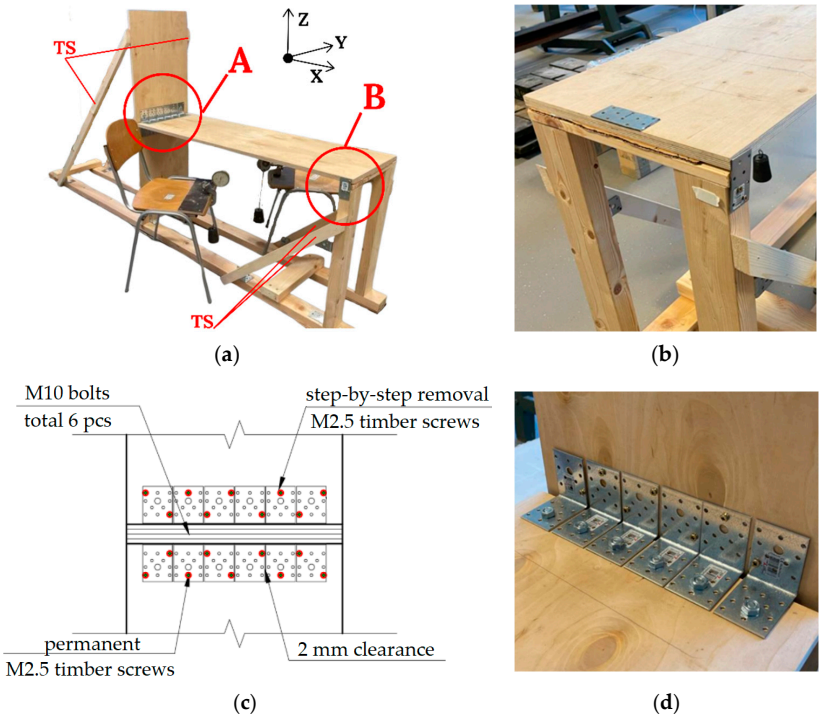


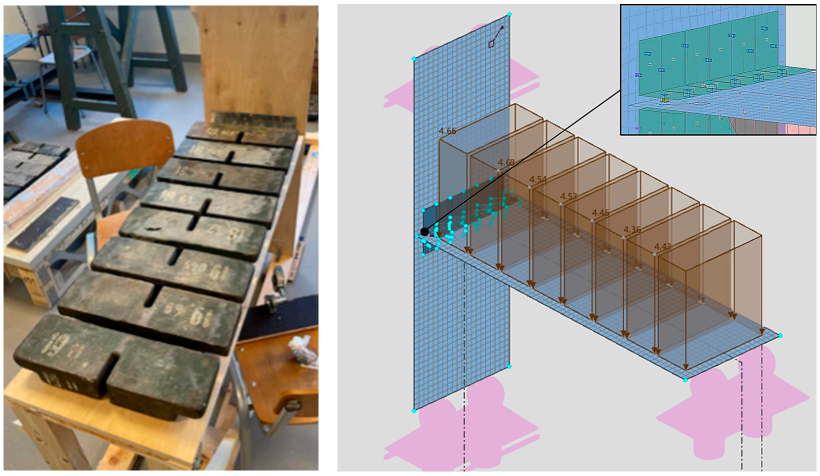
Figure 2. Investigated object: (**a**) stend for modelling semirigid panel-to-panel structural joints of multi-storey buildings, where A is the investigated moment joint of plywood panels, B is a free-end connection of a horizontal plywood panel, and TS are additional timber supports used to ensure stability and reduce unwanted movements of the stend; (**b**) free-end connection of horizontal plywood panel; (**c**,**d**) investigated moment joint of plywood panels.

The structural joint considered during the current study is the moment one which can take up the bending moment. The load-carrying capacities of the considered joint are defined by the parameters of the strengthening details and fasteners by their amounts. The degradation of the connections during the structure's service life is simulated by the unscrewing of timber screws on the top row of steel angles and measurement, thereby simulating the wear and tear of the connection over time. The assumption is that there is a functional relationship between the connection joint's stiffness and the structure's vibrational characteristics.

2.2. Evaluation of Stiffness of Investigated Joint Using Static Loading

To determine the stiffness of the investigated joint at each degradation level, the static loading of the stend and its modelling based on the finite element method are carried out. The panel-to-panel moment joint degradation process was modelled by changing the number of screws in the angle brackets row at the top of the horizontal panel from 9 to 0 under a static load equal to 151.8 kg. Zero timber screws on the top row of angle brackets

represent the case when the investigated connection cannot carry the bending moment, and the horizontal plywood panel is simply supported. The loading was carried out by adding steel pieces with the weight changing within limits from 17 kg to 21 kg. The placement of the steel pieces during loading is shown in Figure 3.



(**a**) (**b**)

Figure 3. (**a**) The placement of the steel pieces during the loading of the stend; (**b**) the numerical model of the panel-to-panel structure with modelled screws.

Numerical models of the investigated joint were developed with the structural analysis program RFEM. This part of the investigation is the determination of the rotation stiffness of the investigated joint at various degrees of joint degradation by calibrating a numerical model to further determine the relationship between the joint's stiffness and the structure's vibrational characteristics. The failure stage of the investigated connection is not of interest. Only the linear behaviour of materials is investigated. The orthotropic elastic material model was used for plywood elements, and the linear elastic material model was used for modelling angle brackets and fasteners.

There were two unknown characteristics of the investigated joint to be determined—the mean elastic modules of the plywood and the joint's rotational stiffness during the modelling, so the two models have been developed differently. The surface type finite element with rectangular mesh and a target length of 0.02 m was used to model the plywood panels for both developed models. This mesh size provided accurate results (reducing the mesh fineness did not change the results significantly) and good calculation speed. During the first modelling approach, angle brackets were modelled using surface-type finite elements and the fasteners were modelled using beam elements as full pipe profiles. The number of fasteners corresponded to the real assembly for each degradation grade. The modulus of elasticity of the plywood was determined via the iterative calibration of the numerical model with laboratory experiment data. The joint degradation was simulated via the step-by-step deletion of timber screws at each new iteration. A total of 10 bolt variations were tested for each load (starting with a non-degraded assembly with 9 timber screws in the top row of the angle brackets to a fully degraded assembly without timber screws in the top row of the angle brackets).

During the second modelling approach, the panel-to-panel connection was modelled using a line hinge function (without modelling fasteners separately) with a defined value of the joint's rotational stiffness. Using the iterative calibration of the developed second approach model with laboratory experiment data, the rotational stiffness of the moment joint was determined for each degradation step.

The maximum vertical displacements of the horizontal panel were determined with laboratory testing using the mechanical deflectometers with a precision of 0.01 mm and numerical models developed in the software RFEM 6 version 6.01.0019.

2.3. Coaxial Correlation Method for Structural Joint Quality Evaluation

The evaluation method proposed for assessing the degradation of structural joints has demonstrated promising results, particularly in the case of two beams joining at right angles both for timber and steel structures [31,32] and steel beam slip connections [33].

A dynamic vibration-based experiment was conducted to evaluate the quality of the timber panel-to-panel moment joint during its degradation. The coaxial correlation method involved generating a signal using specialised software, transmitting the signal through an electrodynamic actuator, capturing the signal with accelerometers placed on both sides of investigated joint, and analysing the differences in the readings to assess the condition of the joint. The experimental setup included an electrodynamic actuator, which produced signals in the frequency range of 10 Hz to 2000 Hz, and two sensors capable of measuring 6D acceleration.

The experimental procedure involved running the sweep-type signals with a duration of 0.5 s in the frequency range of 10 Hz to 2000 Hz applied to the end of the free supported horizontal panel in direction Z according to Figure 4, checking the signals' compatibility with the accelerometer's range, saving the appropriate signals, simulating degradation via the step-by-step removal of timber screws from the upper row of connections, and repeating the experiment until no fasteners remained in the upper row.



(**a**) (**b**) (**c**)

Figure 4. (**a**) The coaxial placement of the accelerometers A1 and A2 on either side of the investigated timber joint; (**b**) the electrodynamic actuator for generating sweep signals; and (**c**) the custom-built board.

The structure's response is measured in three spatial directions: X, Y, and Z, using two 3D accelerometers. The signal is initially detected with an accelerometer A1 affixed to the horizontal element (as a reference point) and subsequently with an accelerometer A2 affixed to the vertical element (Figure 4). The accelerometer readings correspond precisely to an idealised scenario where the joint is perfectly rigid. However, suppose the joint undergoes loss of rigidity during operation. In that case, the accelerometer readings will deviate (indicating energy absorption by the compromised joint), enabling conclusions to be drawn regarding the joint's condition. The obtained signals are transmitted to a computer for further post-processing (Figure 5).

It was concluded in the previous study [33] that the nature of the root mean square (RMS) during the degradation of the joint may change in different axes, and wrongly chosen axes may lead to wrong conclusions regarding the state of the investigated joint, especially in the case of complex joints. During this study, the data post-processing process described in [33] has been enhanced and simplified by introducing one parameter for evaluating joint degradation in three directions at once, thus obtaining a more complete picture of the state of the joint. The proposed dimensionless parameter is obtained using the equation which calculates the volume root square value (RMS_{vol}):

$$RMS_{vol} = \sqrt{RMS_x^2 + RMS_y^2 + RMS_z^2} \quad (1)$$

where RMS_x, RMS_y, and RMS_z are RMS values from the processed signal convolution as a measure of the similarity between two signals in directions X, Y, and Z, correspondingly.

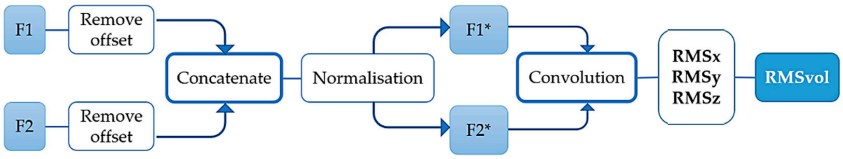


Figure 5. Post-processing scheme of the collected specimen raw response data F1 and F2 from the A1 and A2 accelerometers to the processed specimen response signals F1* and F2* for further similarity comparison using convolution and root mean square (RMS).

In addition to the newly introduced parameter, the evaluation of the joint with the proposed coaxial correlations method was carried out under a loaded stand of 151.8 kg.

3. Results and Discussion

In the framework of static loading with 151.8 kg, ten measurements were made by removing one timber screw from the joint model at each stage. The numerical model, including the modelling of each screw in the investigated joint, was validated with laboratory experiment data. The results obtained for the stend modelling panel-to-panel moment joint are given in Table 1.

Table 1. Vertical displacements and rotational stiffness obtained via static loading and numerical models.

Nr.	Screws Number	Displacement, mm		Difference, %	Rotational Stiffness of the Investigated Joint Obtained by the 2nd Numerical Model, [kNm × rad^{-1} × m^{-1}]
		u_{exp}	$u_{FEM,1}$		
1	9	17.85	18.3	2.46	8.60
2	8	17.83	18.5	3.65	8.30
3	7	18.10	18.6	2.69	8.00
4	6	18.61	18.9	1.56	7.40
5	5	19.30	19.1	1.05	7.00
6	4	19.90	19.7	1.02	6.10
7	3	20.63	20.6	0.15	4.70
8	2	21.73	20.9	3.95	4.30
9	1	22.99	21.4	7.43	3.80
10	0	24.48	23.9	2.43	1.53

The modulus of elasticity of the plywood was estimated at 6800 MPa by comparing the maximum vertical displacements of the stend horizontal panel obtained via the laboratory experiment (u_{exp}) and the first-type numerical model ($u_{FEM,1}$) with modelled fasteners.

The rotational stiffness of the investigated moment joint for the stages differed with the number of screws determined by the second-type numerical model, in which the studied joint is remodelled as a linear support. The rotational stiffness of the linear support is determined iteratively based on the displacements obtained in the laboratory experiment and the modulus of elasticity obtained via validation of the first-type numerical model. The obtained rotational stiffness of the moment joint is used for its quality assessment using the coaxial correlation method.

The post-processing of collected raw response signals F1 and F2 from the A1 and A2 accelerometers includes the removal of offsets. As a result, signals with a mean value of zero are obtained. As a next step, both signals are concatenated to save the scale relationships between two signals in the same axis direction. The concatenated signal pairs'

normalisation is completed to further compare the signal pairs in all three directions. The signal pairs after normalisation in the X, Y, and Z directions are shown in Figure 6.

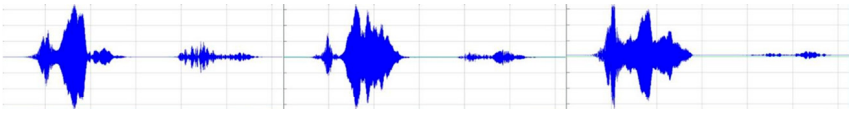


Figure 6. Normalised signal pairs from both accelerometers A1 and A2 in directions X, Y, and Z.

The signal pairs are split after normalisation to the F1* and F2*. The similarity comparison of the obtained signals F1* and F2* is made with the RMS of the signals' convolution in three directions and by determining the proposed dimensionless parameter—volume root mean square value. Obtained volume root square values are given in Table 2.

Table 2. RMS of signals' convolution in three directions and proposed volume root mean square parameter.

Nr.	Screws Number	RMS_x	RMS_y	RMS_z	RMS_{vol}
1	9	1.5739	4.2289	6.0235	7.5262
2	8	2.5188	2.7883	6.3096	7.3437
3	7	3.7834	2.2017	8.3543	9.4316
4	6	1.0254	3.8577	2.9503	4.9636
5	5	0.9018	5.4463	13.9686	15.0199
6	4	2.6823	5.8421	17.5589	18.6986
7	3	4.7522	4.2519	23.3603	24.2150
8	2	0.9565	4.3896	23.1195	23.5519
9	1	2.2475	4.2156	24.4985	24.9599
10	0	7.4473	4.4542	24.5854	26.0720

Figure 7 describes the obtained behaviour of the joint during its degradation. As can be seen, a decrease in moment joint rotational stiffness increases maximal vertical displacements and the proposed parameter—volume root mean square. RMS_{vol} shows the changes in the joint more clearly than maximal vertical displacements. For example, when the joint rotational stiffness decreases by two times, the maximal vertical displacement only increases by 22%, while the RMS_{vol} increases by 213%.

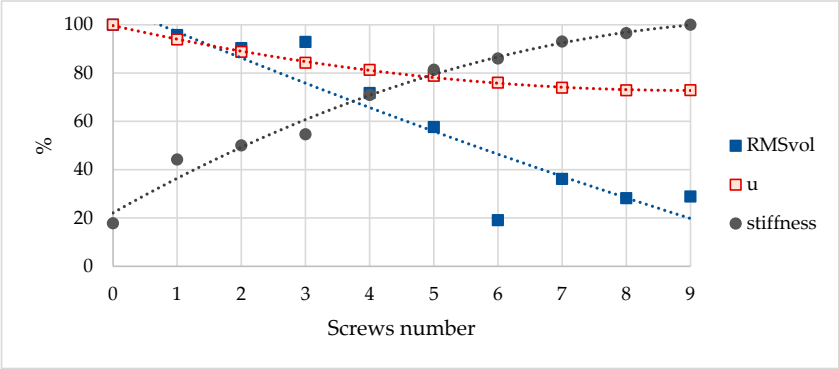


Figure 7. Calculated volume root mean square (RMS_{vol}) and experimental displacements (u) and rotational stiffness of the investigated joint values for various grades of joint degradation as a percentage from the RMS_{vol}, u, and stiffness maximal values.

On the one hand, the dependence between the proposed parameter RMS_{vol} and joint stiffness is obtained. On the other hand, it is the opposite compared to the direct

relationships obtained in the previous research [31–33]. The physic-mechanical clarification of the increased RMS_{vol} with the degradation of the joint stiffness can be explained with the configuration and type of the investigated joint. Figure 6 shows a significant difference in the power of the collected response signals from both accelerometers A1 and A2, indicating signal scattering in this kind of panel-to-panel connection. The transmitted signal is dispersed in multiple directions in the horizontal panel due to various factors, leading to signal degradation in the vertical panel, measured with A2. During the loss of joint stiffness, the horizontal panel becomes more free and can be more exposed to vibrations from the input signal. Based on this, the response signal of the horizontal panel measured with A1 increases in its power and can lead to an overall increase in the RMS of both signals from A1 and A2 convolution.

4. Conclusions

The coaxial correlation method, which includes the processing of response data from coaxially placed accelerometers on either side of the joint, is applied to assess panel-to-panel moment joint degradation in timber structures. The dependence between the proposed new dimensionless parameter, volume root mean square value (RMS_{vol}), and the joint's rotational stiffness is obtained during the research. The following results and conclusions are obtained and made:

- There is a clear relationship between joint stiffness, vertical displacements, and the RMS_{vol} parameter, as well as the RMS_{vol} parameter more sensitively reflecting changes in the joint's condition compared to maximal vertical displacements.
- In the case of the input signal as a sweep signal in the frequency range of 10 Hz to 2000 Hz and the placement of the accelerometer pair symmetrically on either side of the joint, aligned with its axis, an inverse correlation between the calculated RMS_{vol} values of convolution signals and the panel-to-panel moment joint rotational stiffness is obtained.
- The reason for the opposite direction of the relation mentioned above can be signal scattering.
- The changes in the RMS_{vol} parameter can be used for monitoring the system's condition during operation as a reference point using determined parameters at the initial stage, with an approved design stiffness condition. But, it is recommended that, at the stage of the reference measurement, it should be determined whether the input signal is well transferred through the joint by comparing the power of the response signals from both sides of the joint of interest to save a more user-friendly interpretation of the results.

The obtained findings provide valuable insights into the behaviour of timber panel-to-panel connections and offer a non-destructive method for assessing the quality of structural joints. This investigation aims to approve the conception of the existence of the dependence between RMS_{vol} and joint degradation level, and additional research is required to adopt the proposed technique for on-site non-destructive testing.

Author Contributions: Conceptualisation, V.K., A.K., K.B.-V., D.S. and V.L.; methodology, V.K., A.K., K.B.-V., D.S. and V.M.; software, V.K. and V.M.; investigation, V.K., A.K., D.S. and A.P.; data curation, V.K., A.K. and K.B.-V.; writing—original draft preparation, K.B.-V., A.K. and D.S.; writing—review and editing, K.B.-V., V.K., D.S. and V.L.; visualisation, A.K. and K.B.-V.; project administration, D.S., V.L. and M.V. All authors have read and agreed to the published version of the manuscript.

Funding: This research was supported by the Latvian Council of Science's funded project "Method of Correlation of Coaxial Accelerations in 6D Space for Quality Assessment of Structural Joints (COACCEL)" (Nr. lzp-2020/1-0240).



Data Availability Statement: The data supporting this study's findings are available from the second author [A.K.] upon request.

Conflicts of Interest: The authors declare no conflict of interest.

References

1. Basterra, L.-A.; Baño, V.; López, G.; Cabrera, G.; Vallelado-Cordobés, P. Identification and Trend Analysis of Multistorey Timber Buildings in the SUDOE Region. *Buildings* **2023**, *13*, 1501. [CrossRef]
2. Le, S.T.; Nguyen, T.N.; Bui, D.-K.; Ha, Q.P.; Ngo, T.D. Modelling and Multi-Objective Optimisation of Finger Joints: Improving Flexural Performance and Minimising Wood Waste. *Buildings* **2023**, *13*, 1186. [CrossRef]
3. Dobeš, P.; Lokaj, A.; Vavrušová, K. Stiffness and Deformation Analysis of Cross-Laminated Timber (CLT) Panels Made of Nordic Spruce Based on Experimental Testing, Analytical Calculation and Numerical Modeling. *Buildings* **2023**, *13*, 200. [CrossRef]
4. Kiviste, M.; Musakka, S.; Ruus, A.; Vinha, J. A Review of Non-Residential Building Renovation and Improvement of Energy Efficiency: Office Buildings in Finland, Sweden, Norway, Denmark, and Germany. *Energies* **2023**, *16*, 4220. [CrossRef]
5. Tupenaite, L.; Kanapeckiene, L.; Naimaviciene, J.; Kaklauskas, A.; Gecys, T. Timber Construction as a Solution to Climate Change: A Systematic Literature Review. *Buildings* **2023**, *13*, 976. [CrossRef]
6. Brics, A.; Serdjuks, D.; Gravit, M.; Buka-Vaivade, K.; Goremikins, V.; Vatin, N.I.; Podkoritovs, A. The Behaviour of Load-Carrying Members from Cordwood. *Buildings* **2022**, *12*, 1702. [CrossRef]
7. Savolainen, J.M.; Ilgın, H.E.; Oinas, E.; Karjalainen, M. Finnish Multi-Story Timber-Framed Apartment Buildings: Tampere Residents' Perspectives. *Buildings* **2022**, *12*, 1998. [CrossRef]
8. Li, Z.; Tsavdaridis, K.D. Design for Seismic Resilient Cross Laminated Timber (CLT) Structures: A Review of Research, Novel Connections, Challenges and Opportunities. *Buildings* **2023**, *13*, 505. [CrossRef]
9. Kysela, P.; Ponechal, R.; Michálková, D. Airtightness of a Critical Joint in a Timber-Based Building Affected by the Seasonal Climate Change. *Buildings* **2023**, *13*, 698. [CrossRef]
10. Loebjinski, M.; Rug, W.; Pasternak, H. The Influence of Improved Strength Grading In Situ on Modelling Timber Strength Properties. *Buildings* **2020**, *10*, 30. [CrossRef]
11. Yeh, Y.-H.; Yeh, Y.-C.; Wang, T.-C.; Hsu, Y.-C. Comparison of Self-Tapping Screws and Bamboo Nails in Reinforcing the Zuo-Dou Connections in Traditional Oriental Timber Frames of Asia. *Buildings* **2023**, *13*, 709. [CrossRef]
12. Korolkov, D.; Gravit, M.; Aleksandrovskiy, M. Estimation of the Residual Resource of Wooden Structures by Changing Geometric Parameters of the Cross-Section. *E3S Web Conf.* **2021**, *244*, 04010. [CrossRef]
13. Buka-Vaivade, K.; Gaile, L.; Serdjuks, D.; Tatarinovs, A.; Pakrastins, L. Non-Destructive Quality Control of the Adhesive Rigid Timber-to-Concrete Connection in TCC Structures. *Buildings* **2022**, *12*, 2151. [CrossRef]
14. Deng, Z.; Huang, M.; Wan, N.; Zhang, J. The Current Development of Structural Health Monitoring for Bridges: A Review. *Buildings* **2023**, *13*, 1360. [CrossRef]
15. Korolkov, D.I.; Chernykh, A.G.; Kazakevich, T.N.; Mamedov, S.M.; Gravit, M.V. Use of Two-Parameter Distributions for a Joint Assessment of the Residual Resource of Building Structures and Engineering Systems of Buildings and Structures. *IOP Conf. Ser. Mater. Sci. Eng.* **2020**, *775*, 012142. [CrossRef]
16. Josifovski, A.; Todorović, N.; Milošević, J.; Veizović, M.; Pantelić, F.; Aškrabić, M.; Vasov, M.; Rajčić, A. An Approach to In Situ Evaluation of Timber Structures Based on Equalization of Non-Destructive and Mechanical Test Parameters. *Buildings* **2023**, *13*, 1405. [CrossRef]
17. Sola-Caraballo, J.; Rincón-Calderón, J.M.; Rivera-Gómez, C.; López-Martínez, J.A.; Galán-Marín, C. On-Site Risk Assessment Methodology of Historic Timber Structures: The Case Study of Santa Cruz Church. *Buildings* **2022**, *12*, 935. [CrossRef]
18. Jaskowska-Lemańska, J.; Przesmycka, E. Semi-Destructive and Non-Destructive Tests of Timber Structure of Various Moisture Contents. *Materials* **2021**, *14*, 96. [CrossRef]
19. Perković, N.; Stepinac, M.; Rajčić, V.; Barbalić, J. Assessment of Timber Roof Structures before and after Earthquakes. *Buildings* **2021**, *11*, 528. [CrossRef]
20. Han, F.; Zhang, Q.; Wang, C.; Lu, G.; Jiang, J. Structural Health Monitoring of Timber Using Electromechanical Impedance (EMI) Technique. *Adv. Civ. Eng.* **2020**, *2020*, e1906289. [CrossRef]
21. Bakkar, A.R.; Elyamani, A.; El-Attar, A.G.; Bompa, D.V.; Elghazouli, A.Y.; Mourad, S.A. Dynamic Characterisation of a Heritage Structure with Limited Accessibility Using Ambient Vibrations. *Buildings* **2023**, *13*, 192. [CrossRef]
22. Saidin, S.S.; Jamadin, A.; Abdul Kudus, S.; Mohd Amin, N.; Anuar, M.A. An Overview: The Application of Vibration-Based Techniques in Bridge Structural Health Monitoring. *Int. J. Concr. Struct. Mater.* **2022**, *16*, 69. [CrossRef]
23. Morgantini, M.; Betti, R. The Inner Product Vector as an Output-Only Cross-Correlation-Based Feature to Structural Damage Assessment. *J. Vibroeng.* **2020**, *22*, 1373–1398. [CrossRef]
24. Zielińska, M.; Rucka, M. Non-Destructive Testing of Wooden Elements. *IOP Conf. Ser. Mater. Sci. Eng.* **2021**, *1203*, 032058. [CrossRef]
25. Baas, E.J.; Riggio, M.; Barbosa, A.R. A Methodological Approach for Structural Health Monitoring of Mass-Timber Buildings under Construction. *Constr. Build. Mater.* **2021**, *268*, 121153. [CrossRef]

26. Petrović, M.; Pavićević, D.; Ilić, I.; Terzović, J.; Šekularac, N. Elements of a Timber Lamella Structure: Analysis and Systematization of Joints. *Buildings* **2023**, *13*, 885. [CrossRef]
27. Han, F.; Jiang, J.; Xu, K.; Wang, N. Damage Detection of Common Timber Connections Using Piezoceramic Transducers and Active Sensing. *Sensors* **2019**, *19*, 2486. [CrossRef]
28. Dong, L.; Yang, Z.; Wang, Z.; Ding, Y.; Weiqiang, Q. Study on Internal Force of Tunnel Segment by Considering the Influence of Joints. *Adv. Mater. Sci. Eng.* **2020**, *2020*, 1020732. [CrossRef]
29. Hou, Y.; Hu, W.; Wang, X.; Hou, T.; Sun, C. Damage Identification of Ancient Timber Structure Based on Autocorrelation Function. *Adv. Civ. Eng.* **2021**, *2021*, e6683666. [CrossRef]
30. Kurajevs, A. *Quality Assessment of Structural Joints of Timber Structures Using Forced Vibrations*; Riga Technical University: Riga, Latvia, 2023.
31. Serdjuks, D.; Kurtenoks, V.; Tatarinovs, A.; Mironovs, V.; Lapkovskis, V.; Buka-Vaivade, K.; Macevics, A.; Topcijs, K.; Vilnitis, M. Method of Coaxial Accelerations Correlation for Quality Assessment of Structural Joints. *Procedia Struct. Integr.* **2022**, *37*, 547–554. [CrossRef]
32. Serdjuks, D.; Kurtenoks, V.; Tatarinovs, A.; Buka-Vaivade, K.; Lapkovskis, V.; Mironovs, V.; Podkoritovs, A.; Topcijs, K. Non-Model Vibration Analysis Method for Health Monitoring of Structural Joints. *Procedia Struct. Integr.* **2022**, *37*, 555–562. [CrossRef]
33. Buka-Vaivade, K.; Kurtenoks, V.; Serdjuks, D. Non-Destructive Damage Detection of Structural Joint by Coaxial Correlation Method in 6D Space. *Buildings* **2023**, *13*, 1151. [CrossRef]

Disclaimer/Publisher's Note: The statements, opinions and data contained in all publications are solely those of the individual author(s) and contributor(s) and not of MDPI and/or the editor(s). MDPI and/or the editor(s) disclaim responsibility for any injury to people or property resulting from any ideas, methods, instructions or products referred to in the content.

Sutin A., Libbey B., **Kurtenoks V.**, Fenneman D., Sarvazyan A.

Nonlinear detection of land mines using wide bandwidth time-reversal techniques.

Proceedings of SPIE, 2006, 6217, 62171B.

https://doi.org/10.1117/12.673714

Nonlinear detection of land mines using wide band width time-reversal techniques

Alexander Sutin[a, c], Brad Libbey[b], Victor Kurtenoks[a], Douglas Fenneman[b], Armen Sarvazyan[a]

[a] Artann Laboratories, Inc., 1457 Lower Ferry Road, Trenton, NJ 08618
[b] U.S. Army RDECOM CERDEC NVESD, 10221 Burbeck Road, Fort Belvoir, Virginia 22060
[c] Stevens Institute of Technology, Hoboken, NJ 07030

ABSTRACT

Time reversal acoustic (TRA) focusing allows concentration of elastic energy at a location in the soil being investigated to detect landmines. The TRA process is conducted by broadcasting a wide bandwidth signal and recording the surface vibration by a Laser Doppler Vibrometer (LDV). The system impulse response from speaker to the LDV output can then be computed by cross correlating the original and recorded signals for each channel. Each transducer re-radiates the time reversal impulse response. This provides efficient focusing of the seismic wave in both space and time, thus enhancing the nonlinear effects associated with soil and landmine vibrations. Using orthogonal initial signals the suggested TRA procedure can be implemented simultaneously with multiple transmitters to increase the scanning speed. The nonlinear effects were investigated using a phase inversion method where the TRA signal is broadcast a second time with an opposite sign and the two received signals are added in post processing. The summed signal contains mainly the results of nonlinear wave interaction and tends to cancel the linear response. Small scale land mine detection experiments were conducted using a laser Doppler vibrometer and an array of speakers in the frequency band 50-500Hz. They demonstrate that the TRA system provides high concentration of elastic wave energy in the tested area. The measurements of spectral density of the TRA focused signal reveal increased spectral density in the vicinity of mine resonance frequencies. The nonlinear TRA phase inversion method shows higher contrast between mine and no mine than the linear TRA method.

Keywords: land mine detection, Time Reversal Acoustics, nonlinear acoustics

1. INTRODUCTION

Acoustic and seismic waves provide a method to localize landmines in situations where ground penetrating radar, electromagnetic induction, and conventional methods are unsuccessful. This is especially true for plastic mines since the material differences between the soil and landmine is great and the mine is compliant. The mine's compliance causes large surface vibrations in the vicinity of the mine that one can use for mine detection and localization [1-4]. Another localization technique processes surface waves reflected from the mine due to the impedance differences [5-6].

Concentrating seismic wave energy in time and space using principles of Time Reversed Acoustics (TRA) [7-8] can overcome disadvantages of current acoustic and seismic methods [9-13]. Seismic waves, produced by a speaker or shaker propagate outward from the source through a multi-path environment. While airborne sound propagates relatively unencumbered over the ranges of interest, it suffers significant attenuation when coupling into seismic modes. Seismic propagation as body and surface waves is subject to layer effects [14] and attenuation at moderate to high frequency levels. In either case, only a small part of the radiated acoustic or seismic energy reaches a mine. If the source is placed several meters from the mine, the amplitude of the mine vibration could be too small to distinguish a mine using linear methods or to produce nonlinear acoustic effects. Time reversal processing increases the seismic energy in the region under interrogation. The technique creates signals with appropriate delays to ensure that seismic and airborne arrivals from multiple sources are in phase in a soil region at approximately the same time.

Detection and Remediation Technologies for Mines and Minelike Targets XI, edited by J. Thomas Broach, Russell S. Harmon, John H. Holloway, Proc. of SPIE Vol. 6217, 62171B, (2006) · 0277-786X/06/$15 · doi: 10.1117/12.673714

First investigations of application of wide frequency signals for TRA seismic wave excitation were published in [12, 13]. Previous experiments on TRA land mine detection were conducted using tone burst signals that occupy a narrow frequency band. Since the mine resonance depends on the type of mine, soil, and mine burial depth [2-4] fine frequency steps would be required to ensure that the optimal frequency is excited, ultimately resulting in time consuming measurements. TRA is capable of focusing seismic waves with a wide frequency spectrum in order to determine a mine's frequency response. Thus the linear soil surface response indicates the presence of a mine with increased amplitude near the resonant frequency.

Seismic measurements of landmines are often confounded with naturally occurring surface vibration levels due to clutter and inhomogeneous soil. Separation of the landmine response may be possible by taking advantage of the nonlinear elastic characteristics of the mine provided these are distinguished from soil nonlinearities [15-20]. Traditionally, the nonlinear acoustic method utilizes the excitation of two sinusoidal waves at slightly different frequencies. These waves interact with the soil and top surface of the mine, producing different vibration frequencies than the ground near the mine. This method demonstrated the ability to detect plastic antitank and antipersonnel mines.

The time reversal technique is especially effective for nonlinear measurements since it can focus energy in time and space. The nonlinear response near landmines is generally proportional to the linear amplitude squared; therefore one desires high amplitude linear signals to generate the nonlinear components. In the landmine detection scenario we would like to measure the nonlinear response in the vicinity of the mine, but not nonlinearities associated with the loudspeakers or the soil propagation path. Equal amplitude vibration can be generated at the measurement point with lower source drive levels using time reversal than when traditional excitation is used Thus a lower drive signal reduces undesired nonlinear components associated with the propagation path.

This paper presents results of TRA focusing of acoustic and elastic waves on the ground surface for landmine detection. The technique takes advantage of the temporal signal compression to achieve high vibration amplitudes that will excite nonlinear components in the soil.

2. PRINCIPLES OF TIME REVERSAL FOCUSING OF SEISMIC WAVES

The functional elements of the time reversal system include an array of loudspeakers which couple energy into elastic waves in the soil. A vibrometer measures the soil surface at one point and the measured signal is processed using a specially designed system to increase the level of excitation.

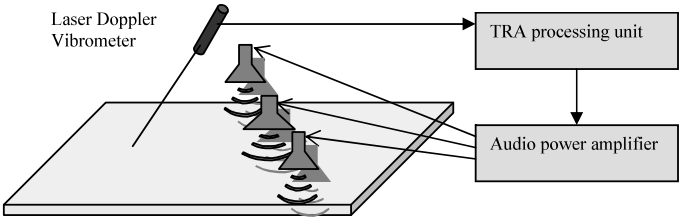


Figure 1. Setup illustrating the TRA focusing of acoustic and seismic waves.

The present work used two different types of excitation signals to measure the system response: linear frequency sweeps that permit channel by channel measurements and orthogonal sets that permit simultaneous measurement of all channels [13, 27]. Both of the signals contain frequencies in a range of 50-500 Hz. The soil vibration measurements from these measurements are used to approximate the impulse response from each loudspeaker to point of measurement on the soil surface. The impulse responses are then time reversed and rebroadcast through the appropriate loudspeaker.

2.1 Wide Band TRA Methodology

The method of time reversal used in this work is essentially a form of match filtering where an approximation of a system impulse response is broadcast through the real system. The impulse is initially flipped in time, so the process of playing the signal through the real system is a physical correlation. The linear system is described here for wide band frequency signals.

Step 1. A wide-bandwidth initial signal $e(t)$ is sent to each speaker sequentially. A variety of wide bandwidth signals can be used for land mine detection and a review of these signals is presented in [21] and further discussed in section 2.2.

Step 2. A laser Doppler vibrometer records surface vibration for each loudspeaker. The measured signal can be represented as

$$v_k(t) = e(t) \otimes h_k(t) \tag{1}$$

Where $h_k(t)$ is the system impulse response between the electrical signal applied to speaker number k and the output of the LDV; and $\otimes$ indicates linear convolution. This direct signal is cross-correlated[1] with the radiated signal resulting in a short pulse, $s_k(t)$.

$$s_k(t) = v_k(t) \otimes e(-t) \tag{2}$$

The signal approximates the system impulse response, $h_k(t)$, but has frequency content scaled by the frequency content of the radiated signal. This can be shown by considering the cross-correlation of the received signal and the source signal in the frequency domain:

$$S_k(\omega) = E(\omega) H_k(\omega) E^*(\omega) \tag{3}$$

Where $E(\omega)$, $H_k(\omega)$, and $S_k(\omega)$ are the Fourier spectra of an initial signal $e(t)$, transfer function $h_k(t)$, and cross correlation of the received signal and radiated signals $s_k(t)$ respectively. For an initial signal with constant spectral density in the frequency band of interest $E(\omega) = E_0$ for $\omega_1 \le \omega \le \omega_2$, the cross correlation of the received signal is proportional to the system impulse response.

$$S_k(\omega) = E_0^2 H_k(\omega) . \tag{4}$$

Thus the system impulse response in a limited frequency band can be approximated in the time domain as $\hat{h}_k(t)$.

$$\hat{h}_k(t) = \frac{s_k(t)}{E_0^2} \tag{5}$$

Step 3. The approximate system impulse is time reversed and normalized, channel by channel for all loudspeakers. The normalization maintains the same peak amplitude for all radiated signals. The prepared signals have the form

$$r_k(t) = \frac{s_k(t_{delay} - t)}{\max[s_k(t)]} \tag{6}$$

Where t_{delay} is an arbitrary delay chosen to ensure causality.

[1] Cross correlation is presented in equations as a linear convolution with a flipped signal, which is an equivalent expression.

Step 4. A second measurement records the surface vibration $p_k(t)$, produced by broadcasting the time reversal signals $r_k(t)$ over all loudspeakers simultaneously. The measured signal associated with loudspeaker k can be expressed as

$$p_k(t) = r_k(t) \otimes h_k(t) \tag{7}$$

Since the TRA signals are applied simultaneously to all loudspeakers the total response is a superposition of the individual responses.

$$p_{tot}(t) = \sum_{k=1}^{N} r_k(t) \otimes h_k(t) \tag{8}$$

The spectrum of the surface vibration is approximately proportional to the square of the impulse function spectra, $P_k(\omega) \approx H_k(\omega)\hat{H}_k(\omega)$. Thus the final response for one channel will have preferentially excited natural resonances of that system and will emphasize the mine resonances. When multiple loudspeakers are utilized the spectral response will be a summation of all channels' spectral responses including the mine's resonances. We expect that the impulse responses will reflect the mine's resonances the same for all speakers.

2.2 TRA focusing with orthogonal signals

Two types of source signals were used to measure the systems' impulse responses. A linear frequency sweep is an obvious choice, but requires that the impulse response be measured sequentially for each loudspeaker. Alternatively, the initial broadcast signals can be radiated from all speakers simultaneously by choosing an orthogonal set of signals, this quickens the measurement time [13]. Folegot describes these signals in detail [27], but they are conceptually presented here without rigorous mathematical detail.

Each source signal consists of a combination of equal amplitude sinusoidal components with random phase. They differ in that each signal has unique frequency content making them orthogonal to all other channels. This is achieved by creating a comb structure of frequency components that does not overlap the other signals being used. The result is a set of K noise-like signals that can be broadcast simultaneously from the sources. The orthogonal signal set, $e_k(t)$ (k=1:K), are broadcast simultaneously through the loudspeakers thus the first vibration measurement is a superposition of all sources.

$$s_{tot} = \sum_{k=1}^{K} e_k(t) \otimes h_k(t) \tag{10}$$

After measurement, the individual impulse responses are separated by cross-correlating the received surface vibration signal with each loudspeaker signal. For example, the impulse response associated with loudspeaker l is the cross-correlation between the measured vibration and the radiated signal $e_l(t)$.

$$s_l(t) = s_{tot} \otimes e_l(-t) = \sum_{k=1}^{K} [e_k(t) \otimes e_l(-t)] \otimes h_k(t) \tag{11}$$

The utility of orthogonal signals is that the cross correlation between different orthogonal signals is close to zero.

$$e_k(t) \otimes e_l(-t) = n(t) \qquad k \neq l \tag{12}$$

Where $n(t)$ is noise that is small in comparison to contribution from the auto-correlation.

$$e_k(t) \otimes e_l(-t) \approx E_0^2 \delta(t_\delta) \qquad k = l \tag{13}$$

Where $\delta(t_\delta)$ is a delta function provided the spectral content is broadband. In practice a finite bandwidth results in a finite width pulse instead of a true delta function. Substitution of (12) and (13) into (11) results in an impulse response similar to (5), that can then be utilized as in steps 3 and 4 in the preceding section.

2.3 The principle of nonlinear phase inversion method

One nonlinear acoustic method of land mine detection utilizes the excitation of two frequency waves, which interact with the top surface of the mine, producing a difference vibration frequency than that of the excitation [15-20]. The disadvantages of this method are connected with limited frequency range of excited waves that may not match the mine's resonance. Sweeping of the excitation frequencies addresses this problem at the cost of extended measurement time.

This paper investigates an alternative method of nonlinear measurement, the phase-inversion method, using a wide frequency band signal [23-26]. This method was initially proposed for ultrasonic imaging of microbubbles (contrast agents) in medical ultrasound. Bubbles have distinguishable resonance and nonlinear properties similar to that of mines. If bubbles are insonified simultaneously at two frequencies, f_1 and f_2, then the backscattered echo will contain spectral content at the sum and difference frequencies, as well as higher order terms [23]. By filtering around the nonlinear components, the backscatter from bubbles can be isolated from tissue backscatter. Since the nonlinear characteristics of bubbles are several orders of magnitude greater than tissue, these methods can be used to enhance contrast between bubbles and tissue.

The idea behind the phase-inversion method is that the linear portion of a signal is cancelled leaving nonlinear terms for analysis. In this implementation two time reversed pulses are sent out in sequence, the first, $r_k(t)$, with a sign opposite that of the second, $-r_k(t-T)$, where T is the period of the signal. The linear vibration response from each of these signals is recorded producing a response $p_{tot}(t)$ and $-p_{tot}(t)$ respectively, as described by (8). As a result the two linear responses at the measurement point will have opposite signs and shifting the second signal back by T and summing will cancel the response.

The nonlinearity of the system leads to distortion of the recorded signal. In the case where quadratic nonlinearities dominate a sign change will not produce cancellation. Thus the actual sum of the two received signals is

$$p_{sum} = \left[p_{tot} + \Phi(e_k(t))\right] + \left[-p_{tot} + \Phi(-e_k(t))\right] \tag{14}$$

where the function $\Phi(e_k(t))$ represents the nonlinear part of the surface vibration. In the absence of nonlinearities, the sum of the received signals is close to zero. In the presence of nonlinearities, the amplitude is proportional to the level of nonlinearity in the tested medium. This method has a higher sensitivity than the conventional methods of nonlinear detection because it takes into account nonlinearities at a variety of frequencies. Additional advantages of this method are that a high amplitude short pulse can be produced at the measurement region of interest while limiting the nonlinear contributions from the propagation path.

3. EXPERIMENTAL SETUP AND SIGNAL ILLUSTRATIONS

At the center of the experimental setup is a prototype Artann Labs TRA system. This component is responsible for the time synchronization of 8 channels of output and 1 channel of input data acquisition. It is controlled via Ethernet from a laptop computer running proprietary software that facilitates the measurements described above. Additional hardware includes: eight channels of audio amplification from commercial surround sound amplifiers, eight Audiobahn 12 inch loudspeakers, a Polytec Laser Doppler Vibrometer CLV-1000, one microphone and preamplifier (Tube Ultragain 100), and a signal generator BNC625 that was used for calibration of the TRA system.

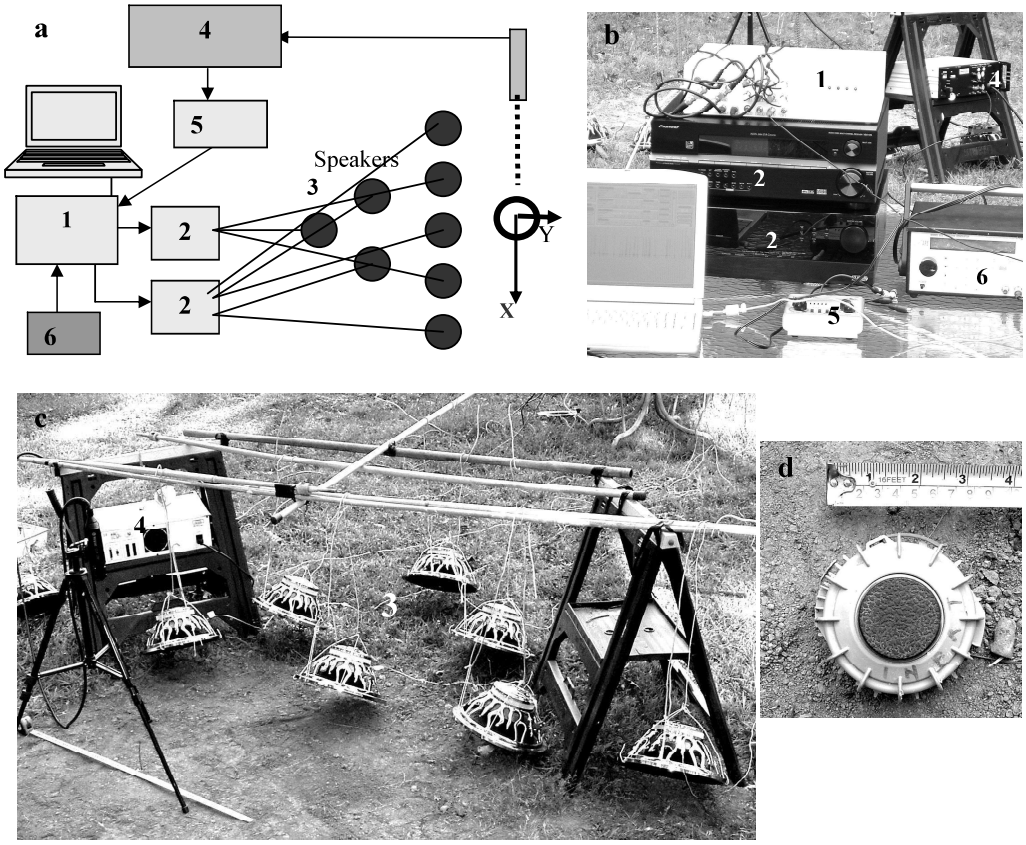


Figure 2. **a)** Block diagram of the system components: 1) TRA system, 2) power amplifiers, 3) speakers, 4) Laser Doppler Vibrometer (LDV), 5) microphone preamplifier, 6) signal generator used for calibration, **b) c)** pictures of the experimental setup for TRA focusing, and **(d)** anti personal landmine used in the experiments presented here.

The experiments were performed in sand and soil containing clay, sand, small rocks, and fine organic matter. A VS-50 antipersonnel mine was buried at a depth of 2 cm unless otherwise stated and surface vibration measurements were taken in positions directly above as well as adjacent to the mine. A mine has little influence on soil surface vibration measurements acquired a diameter of more away from the mine unless a defined effort to excite and process for surface waves in undertaken [5]. Thus when we reference a "no mine" measurement this implies a soil measurement taken at least a diameter distance from the mine.

The tests with linear frequency sweep signal (LFS) were conducted according the sequence of steps described above and examples are given in Fig. 3. A windowed LFS, $e(t)$, is broadcast sequentially from each loudspeaker, Figs. 3a and 3b, and the resultant surface vibration, $v_k(t)$, is measured for each loudspeaker, Fig. 3c. The surface vibration measurement is then cross-correlated with $e(t)$ resulting in an approximation of the system impulse response in the excitation frequency band, 50-500Hz, Fig. 3d. The impulse response is then time flipped and scaled, $r_k(t)$, to maximize the useable dynamic range of the digital to analog converter for subsequent broadcast, Fig. 3e. Finally, the prepared signals are

broadcast from all loudspeakers simultaneously producing a pulse soil vibration response. This response is shown twice in Fig. 3f; the second is a response to the phase inverted broadcast of the TRA signals. Variations of the spectra of the TRA focused signals are presented in later sections for mine and no mine conditions.

3.1 Experiments with linear frequency sweeps

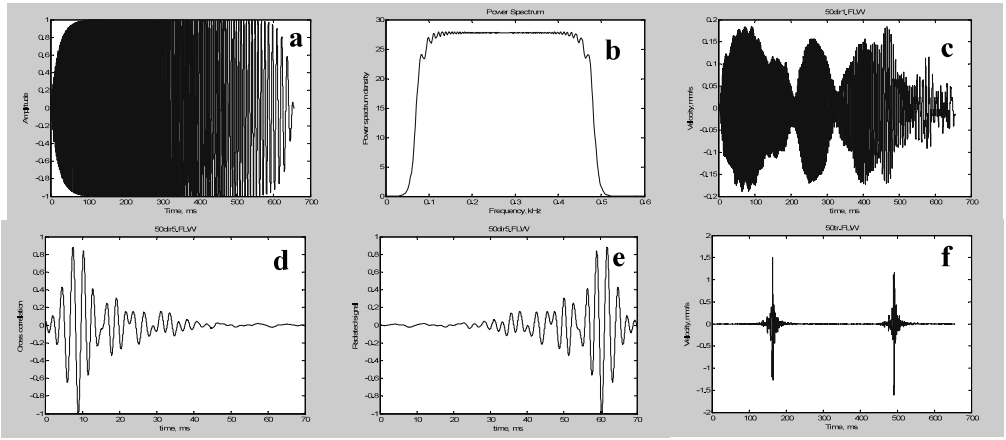


Figure 3. Examples of signals used during the TRA experiments: a) $e(t)$, the initial linear frequency sweep; b) $E(\omega)$, its spectrum; c) $v_k(t)$, surface vibration measurement recorded by the LDV corresponding to speaker k; d) $s_k(t)$, system impulse response estimate based on cross-correlation of $v_k(t)$ and $e(t)$; e) $r_k(t)$, the time reversed signal for subsequent broadcasts; f) $p_{tot}(t)$, two surface vibration measurements resulting from the broadcast of $r_k(t)$ simultaneously from all loudspeakers the second pulse has opposite sign.

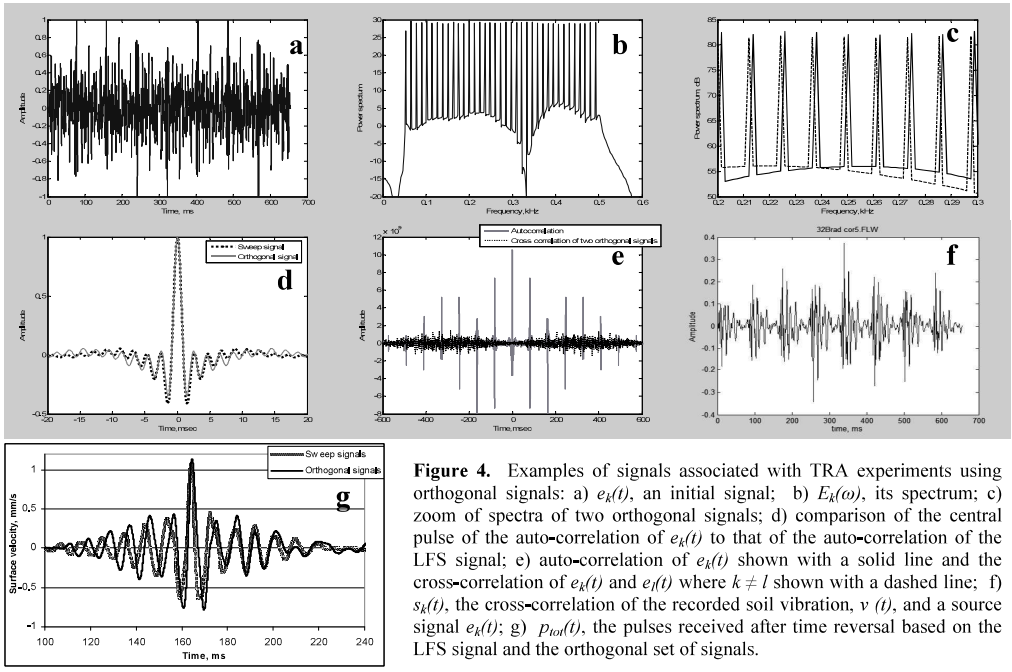


Figure 4. Examples of signals associated with TRA experiments using orthogonal signals: a) $e_k(t)$, an initial signal; b) $E_k(\omega)$, its spectrum; c) zoom of spectra of two orthogonal signals; d) comparison of the central pulse of the auto-correlation of $e_k(t)$ to that of the auto-correlation of the LFS signal; e) auto-correlation of $e_k(t)$ shown with a solid line and the cross-correlation of $e_k(t)$ and $e_l(t)$ where $k \neq l$ shown with a dashed line; f) $s_k(t)$, the cross-correlation of the recorded soil vibration, $v(t)$, and a source signal $e_k(t)$; g) $p_{tot}(t)$, the pulses received after time reversal based on the LFS signal and the orthogonal set of signals.

3.2 Experiments with orthogonal signals

Multiple orthogonal source signals, as opposed to one signal, permit simultaneous measurement of all system impulses simultaneously. The comb frequency structure of two of these signals is illustrated in Fig. 4. A byproduct of correlating these signals is the appearance of multiple pulses outside of the central region of interest. These byproducts will be windowed out during processing of the measured signals leaving only the pulse like nature of the auto-correlation and the low amplitude noise associated with cross-correlation. The auto-correlation function's central pulse is similar to the auto-correlation function of LFS chirp as shown in Fig. 4d, as a result when one of the orthogonal source signals is cross-correlated with the soil response the impulse response estimates, Fig. 4f, are similar to that measured with the LFS signals, previous shown in Fig. 3d, with exception to the byproduct pulses. Experiments then produce results similar to that illustrated in Figs. 3d and 3f.

4. SPECTRAL DENSITY OF TRA FOCUSED SIGNALS DUE TO MINE PRESENCE

It is well known that surface vibrations are higher in the vicinity of a mine than in surrounding soil regions [1-4]. Fig. 5 presents examples of direct LFS signals and two TRA focused signals recorded for positions with and without a mine. This figure illustrates that the amplitude of soil vibration directly above the mine is nearly twice that without the mine.

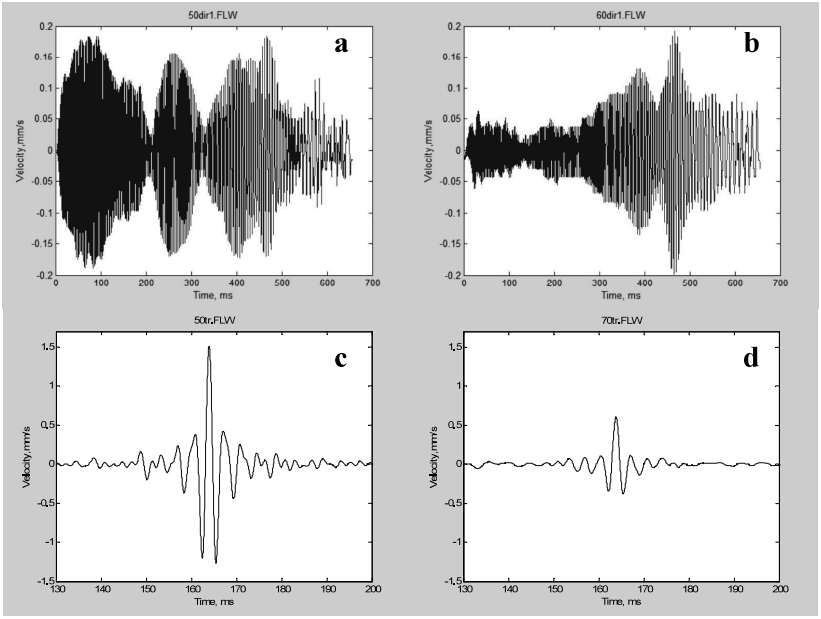


Figure 5. Measurements of the soil vibration for an individual loudspeaker system response using a LFS excitation a) with mine and b) without mine. The system response to the TRA focused signals from all loudspeakers c) with mine and d) without mine.

Spectral density was used as a means of characterizing the energy of the soil vibrations much like its use in underwater acoustics [28]. The soil spectral density of the initial broadcast and TRA focused response (time windowed from 140-190 ms) are presented in Fig. 6.

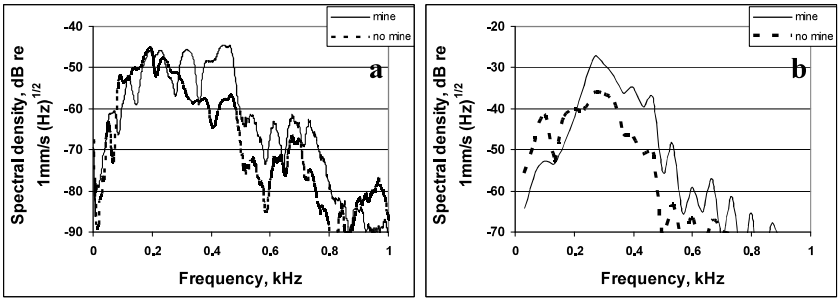


Figure 6. Spectral density of the soil surface with a buried VS-50 mine and without. a) Direct response from one channel of excitation and b) using the TRA focused signals.

5. RESULTS

5.1. Measurements and spatial distributions of linear and nonlinear TRA focused signals

Section 2.3 describes the nonlinear phase inversion method that sums two TRA focused signals broadcast with opposite phases. The linear portions cancel and leave an indication of the quadratic nonlinearities. The examples of summed signals measured above the antipersonnel mine and without a mine are presented in Fig. 7. The normal TRA focused signals for these cases are presented in Figs. 4 and 5. The spectral density of the summed signals shows the largest contrast occurs between 500-800 Hz. This band roughly corresponds to the second harmonics of the radiated signals shown in Fig. 6. The nonlinear spectral differences between the mine and no mine conditions are larger than the linear spectral differences of the TRA focused signal in Fig. 6.

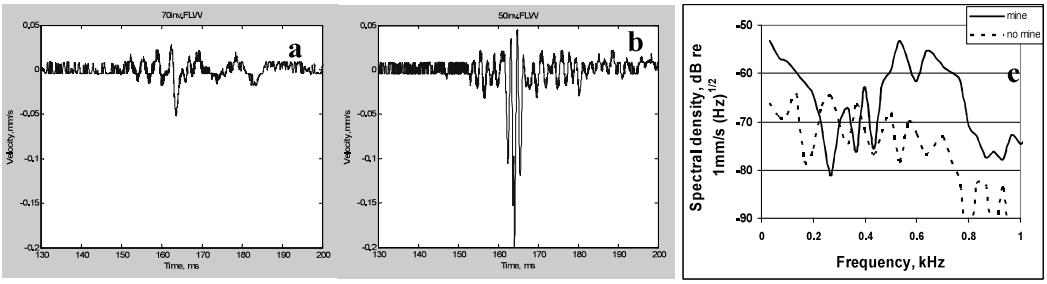


Figure 7. Nonlinear responses generated by summing TRA phase inverted signals a) above the VS-50 mine, b) without the mine, and c) spectral density.

The nonlinear responses to the TRA signals provide a higher contrast comparing mine to no mine than the linear response. Fig. 8 shows the spatial distribution of the linear and nonlinear TRA responses. To generate this data the TRA signals were focused on each measurement point independent of previous measurements. In other words the procedure outline in section 2.1 was repeated along a line passing above the antipersonnel mine.

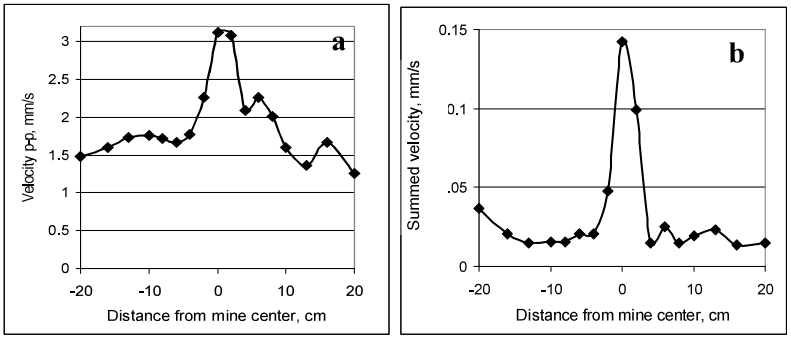


Figure 8. The spatial distribution of soil vibration along a line passing above the antipersonnel mine. a) Linear TRA focused signal and b) nonlinear response of the TRA signal.

5.2 The amplitude dependencies of nonlinear generated signal

The experiments demonstrate that nonlinear TRA response variations due to the presence of a mine are greater than the linear response differences. To investigate the relationship between linear and nonlinear responses the TRA broadcast amplitudes were decreased incrementally to the noise floor. This technique was performed for a variety of mine burial depths at the same physical location and using a new set of TRA focused signals for each depth. The tests were conducted for the antipersonnel mine VS-50 buried in soil and sand.

The dependency of the nonlinear TRA amplitude on the linear amplitude is presented in Fig. 9. The TRA linear amplitude is the peak to peak amplitude of the TRA temporal response. The nonlinear amplitude is calculated by summing the normal and phase-inverted TRA signals, band pass filtering from 500-1100Hz, and selecting the peak to peak amplitude. Fig. 9 shows that the relationship between linear and nonlinear response amplitudes is quadratic once the amplitude of the signals exceeds the noise floor. While this relationship holds for different burial depths and soil types the variations in the offset parameter are not entirely understood and will be investigated in future work.

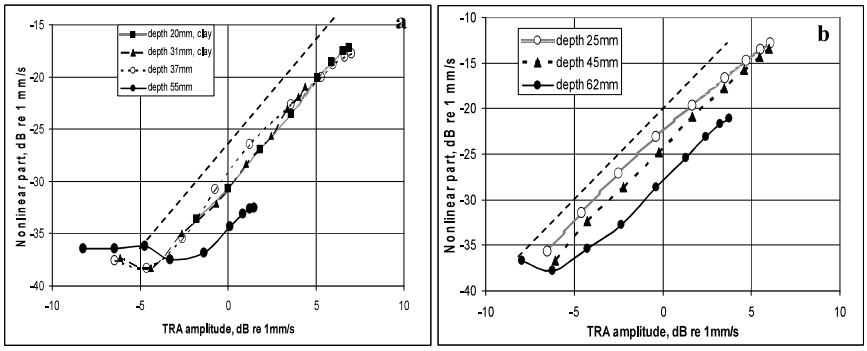


Figure 9. The nonlinear TRA response as a function of the linear TRA response for a VS-50 antipersonnel mine at various depths in a) soil and b) sand. The dotted line shows a quadratic dependence ($A_{non} \sim A_{lin}^2$).

6. CONCLUSION

Land mine detection experiments were conducted using a time reversed acoustic focusing system. This system of hardware and signal processing is capable of focusing wide bandwidth seismic and acoustic energy at a target location in both time and space. By using orthogonal source signals, the system impulse responses between multiple sources and a receiver can be measured simultaneously thus reducing the overall measurement time associated with sequential source broadcasts.

The nonlinear response of the target region can be measured using the TRA method of phase inversion. In this case the linear response cancels in post processing leaving the nonlinear response. This response is predominantly influenced by the large amplitude region where the linear signals are focused making it an ideal tool for measuring the mines nonlinear response as opposed to the nonlinear response of the transmission system. This method provides the higher contrast for mine/no mine comparisons than the linear method.

ACKNOWLEDGEMENTS

Work was supported by U.S. Army RDECOM CERDEC Night Vision and Electronic Sensors Directorate under contract W909MY-05-C-0007.

REFERENCES

1. T. R. Witten, K. Sherbondy, J. Habersat, J. M. Sabatier, "Acoustic technology for land mine detection: Past tests, present requirements, and future concepts." *Proc. SPIE: Detection and Remediation Technologies for Mines and Minelike Targets V*, A. C. Dubey, Ed., **4038,** 781-789, 2000.
2. N. Xiang and J. M. Sabatier, "An experimental study on antipersonnel landmine detection using acoustic-to-seismic coupling." *J. Acoust. Soc. Am*, **113**, (3), 1333-1341, 2003.
3. J. M. Sabatier, "Land mine detection measurements using acoustic-to-seismic coupling". *Proc. SPIE: Detection and Remediation Technologies for Mines and Minelike Targets V*, A. C. Dubey, Ed., **4038,** 645–655, 2000.
4. V. Valeau, J. M. Sabatier, R. D. Costley, N. Xiang, "Development of a time-frequency representation for acoustic detection of buried objects." *J. Acoust. Soc. Am*, **116**, (5), 2984-2995, 2004.
5. A. Behboodian, W. R. Scott, Jr., J. H. McClellan, "Signal processing of elastic surface waves for localizing buried land mines." *Proc. 33rd Assilomar Conf. on Sig., Sys., and Comp*. Assilomar, CA, Oct. 1999.
6. W. R. Scott, Jr., G. D. Larson, J. S. Martin, G. S. McCall II, "Field testing and development of a seismic landmine detection system." *Proc. SPIE*: *Detection and Remediation Technologies for Mines and Minelike Targets VIII,* R. S. Harmon, Ed., **5089**, 643-652, 2003.
7. M. Fink, D. Cassereau, A. Derode, C. Prada, P. Roux, M. Tanter, J. L. Thomas, F. Wu, "Time-reversed acoustics*." Rep. Prog. Phys*., **63**, 1933–1995, 2000.
8. M. Fink, "Time reversed acoustics." *Scientific American* , 91-97, 1999.
9. P. D. Norville, W. R. Scott, Jr., G. D. Larson, "An investigation of time reversal techniques in seismic landmine detection." *Proc. SPIE: Detection and Remediation Technologies for Mines and Minelike Targets IX,* **5415**, 1310–1322, 2004.
10. A. Sutin, P. Johnson, J. TenCate, A. Sarvazyan, "Time reversal acousto-seismic method for land mine detection." *Proc. SPIE: Detection and Remediation Technologies for Mines and Minelike Targets X.* R. S. Harmon, Ed **5794,** 706-716, 2005.
11. P. D. Norville and W. R. Scott, Jr., "Time-reversal focusing of elastic waves in inhomogeneous media: an application to an elastic-wave landmine detection system." *Proc. SPIE: Detection and Remediation Technologies for Mines and Minelike Targets X.* R. S. Harmon, Ed. **5794**, 632-672, 2005.
12. P. D. Norville, W. R. Scott, Jr., "Time-reversal focusing of elastic surface waves." *J Acoust. Soc. Am*., **118**, (2), 735-744, 2005.
13. B. Libbey, D. Fenneman, "Acoustic to seismic ground excitation using time reversal." *Proc. SPIE*: *Detection and Remediation Technologies for Mines and Minelike Targets X,* R. S. Harmon, Ed., **5794,** 643-654**,** 2005.
14. M. S. Fokin, V. N. Fokin, J. M. Sabatier, "Effect of ground variability on clutter and false alarm in landmine detection." *Proc. of SPIE: Detection and Remediation Technologies for Mines and Minelike Targets IX*, R. S. Harmon, Eds., **5415,** 156-166, 2004.

15. D. M. Donskoy, A. Ekimov, N. Sedunov, M. Tsionskiy, "Nonlinear seismo-acoustic land mine detection and discrimination." *J. Acoust. Soc. Am.*, **111**, (6), 2705-2714, 2002.
16. D. M. Donskoy, A. M. Sutin, "Method and apparatus for acoustic detection of mines and other buried man-made objects." *United States Patent* # 5,974,881, Nov. 2, 1999.
17. J. M. Sabatier, M. S. Korman, N. Xiang, "Linear and nonlinear acoustic velocity profiles over buried land mines." *Proc. SPIE*: *Detection and Remediation Technologies for Mines and Minelike Targets VII*, **4742,** 695-700, 2002.
18. G. D. Larson, J. S. Martina, P. H. Rogers, W. R. Scott, Jr., G. S. McCall II, "Impact of nonlinear effects on a high-frequency seismic landmine detection system." *Fifth Int. Symp. "Technology and the Mine Problem"* Naval Postgraduate School, Monterey, CA**,** April 22-25, 2002.
19. M. S. Korman, J. M. Sabatier, "Nonlinear acoustic techniques for landmine detection." *J Acoust. Soc. Am.*, **116**, (6), 3354–3369, 2004.
20. D. M. Donskoy, A. Reznik**,** A. Zagrai, A. Ekimov, "Nonlinear vibrations of buried landmines." *J Acoust. Soc. Am.*, **117**, (2), 690–700, 2005.
21. J. S. Martin, W. R. Scott, Jr., G. D. Larson, P. H. Rogers, G. S. McCall II, "Probing signal design for seismic landmine detection." *Proc. SPIE: Detection and Remediation Technologies for Mines and Minelike Targets IX,* R. S. Harmon, Ed., **5415,** 133-144, 2004.
22. V. Bertaix, J. Garson, J. Quieffin, S. Catheline., J. Derosny, M. Fink, "Time-reversal breaking of acoustic waves in a cavity." *Am. J. Phys*., **72** (10), 1308-1311. 2004.
23. S. Krishnan, M. O'Donnell, "Transmit aperture processing for nonlinear contrast agent imaging." *Ultrasonic Imaging,* **18** (2), 77-105, 1996.
24. J. Janica, S. Wojciech, S. Dolorzycki, J. Polakow, J. Walecki, J. R. Ladny, W. Laszewicz, "Contrast-enhanced, wide-band phase-inversion power Doppler imaging of hepatic focal nodular hyperplasia." *Hepatogastroenterology,* **51** (57), 705-708, 2004.
25. T. Schmidt, C. Hohl, P. Haage, D. Honnef, A. H. Mahnken, G. Krombach, W. Piroth, R. W. Günther, "Phase-inversion tissue harmonic imaging compared to fundamental B-mode ultrasound in the evaluation of the pathology of large and small bowel." *European Radiology*, **15** (9), 2021-2030, 2005
26. A. Bauer, P. Hauff, J. Lazenby, P. Von Behren, M. Zomack, M. Reinhardt, R. Schlief, "Wideband harmonic imaging: A novel contrast ultrasound imaging technique." *European Radiology*, **9, (**3), S364-S367, 1999.
27. T. Folegot, J. de Rosny, C. Prada, M. Fink, "Adaptive instant record signals applied to detection with time reversal operator decomposition." *J. Acoust. Soc. Am*., **117** (6), 3757-3765, 2005.
28. R. J. Urick, *Principles of Underwater Sound.* McGraw-Hill, 1983.

Smetskaja V., Litvinenko A., **Kurtenoks V.**, Stepanovs V., Lapkovskis V., Bespal'ko V.

Study on thermal stability of multi-channel picosecond precise time-tagging system.

2023 IEEE 10th Jubilee Workshop on Advances in Information, Electronic and Electrical Engineering (AIEEE), 2023, 87–90.

https://doi.org/10.1109/AIEEE58915.2023.10134855

Study on Thermal Stability of Multi-channel Picosecond Precise Time-Tagging System

Viktorija Smetskaja
Eventech Ltd. / Riga Technical University
Riga, Latvia
v.smetskaja@gmail.com

Anna Litvinenko
Riga Technical university
Signal Processing and Space Electronics Laboratory
Riga, Latvia
Anna.litvinenko@rtu.lv

Viktors Kurtenoks
Eventech Ltd.
Riga, Latvia
v.kurtenoks@eventechsite.com

Vsevolods Stepanovs
Eventech Ltd.
Riga, Latvia
vsevolods.stepanovs@gmail.com

Vjaceslavs Lapkovskis
Eventech Ltd. / Riga Technical University
Riga, Latvia
vjaceslavs.lapkovskis@rtu.lv

Vladimir Bespal'ko
Eventech Ltd.
Riga, Latvia
bezpvlad@gmail.com

2023 IEEE 10th Jubilee Workshop on Advances in Information, Electronic and Electrical Engineering (AIEEE) | 979-8-3503-1178-5/23/$31.00 ©2023 IEEE | DOI: 10.1109/AIEEE58915.2023.10134855

***Abstract*—This work is devoted to an experimental study of the thermal stability of a multichannel timing system with picosecond precession. The main area of application of the observed multichannel synchronization system is satellite laser ranging (SLR) stations with several pulsed radiation sources. The possibilities of multichannel measurements will significantly increase the accuracy of measurements and open up new opportunities for scientists working in satellite positioning, synchronization, geodesy, etc. The concept of the developed multichannel system, including the proposed synchronisation method, is described. The prototype consists of five independent event timers, an AFG (arbitrary function generator), a reference clock active splitter, and a controllable equal delay multiplexer. The AFG generates a 10 MHz reference clock and an event signal (1 PPS). All five event timers and a controlled delay multiplexer are connected to the PC from which they are controlled. The thermal chamber was used to organize measurements of thermal stability. The temperature in the thermal chamber was changed from 15 to 30°C, and the initial calibration of the system was carried out at a temperature of 22.5°C.**

Keywords—event timer, synchronization methods, multichannel event timing, thermal stability, picosecond precision, satellite laser ranging

I. INTRODUCTION

For Earth-orbiting satellites, laser ranging dates back to 1964, when the first successful experiments were carried out at the Goddard Optical Research Center, now called the Goddard Geophysical and Astronomical Observatory. A team of scientists fired a ruby laser - brand new at the time - at the Explorer 22 spacecraft orbiting high in Earth's atmosphere. The satellite, also known as Beacon Explorer B, was equipped with a set of reflectors designed specifically to send the laser signal back to its point of origin. The researchers measured the distance to the spacecraft at around 966 km and with an accuracy of about 3 meters [1]. From that moment, laser ranging became a technology in everyday use. Nowadays, Satellite Laser Ranging (SLR) Stations are placed worldwide and used for geodesy, geomatics, satellite positioning and synchronization, debris tracking, the basis for special tests of the Theory of General Relativity, climate monitoring, oceanography, etc. One of the core parts of SLR technology is ultra-precise time measurements. The ultra-precise measurement equipment should meet a high requirement on immunity and stability, including thermal stability.

The study of the thermal stability of accurate time-event detection systems is a critical aspect of applying and interpreting the results produced by such systems [2], [3]. Calibrations at different temperatures are performed to determine the effect of temperature conditions on the time delays in the circuits [4].

Time scale shift due to changes in operating temperature can lead to desynchronization of the multichannel timing system, thereby introducing a significant timing error for consecutive events and a discrete series of events requiring a fixed time scale.

The issue addressed in this publication is critical for space applications [5], as well as for ground-based systems that need to consider the temperature effect on the measurement accuracy of time-tagging systems [6].

The study is focused on timing technology, Event Timers with multiple channels for Satellite Laser Ranging (SLR) stations with multiple pulse emission sources. Such a requirement was announced by leading organizations and experts (DIGOS, Pulse Power, DLR) during the last International Laser Ranging Service (ILRS) event organized in Stuttgart on October 21–25, 2019. [7] While the current timing system developed by the Eventech team is recognized as a standard for Satellite Laser Ranging by NASA, and it is used in more than half of the SLR stations and is also applicable for other applications where precise and fast event timing is required (reflectometry, 3-d scanning, gravimetry, etc.).

The paper is organized as follows: the first section is devoted to the introduction, the second section presents the concept of a multi-channel time-tagging system, the third section discusses the setup for experimental studies, and the fourth section analyzes the results of thermal stability tests, last but not least section concludes the study.

II. MULTI-CHANNEL TIME-TAGGING SYSTEM

Multi-channel timing system development mainly aims at Satellite Laser Ranging (SLR) stations with multiple pulse emission sources. This new timing system will allow receiving data about multiple inputs' rising slope, extremum, and falling slope. This information will significantly increase

979-8-3503-1178-5/23/$31.00 ©2023 IEEE

the precision of the measurements and open new opportunities for scientists working in the satellite position field, synchronization, Geodesy, etc.

A. Multi-channel Synchronisation Method

The five event timers' synchronization method examination is based on an experimental study. The prototype with 5 independent channels was made on the Eventech event timers base for study performance.

After the event timer is turned on, its time scale is arbitrary. Therefore, even if several timers are turned on simultaneously, the time-tags of each timer for the same event will still be different. For all the channels to show the same time-tag for one event, it is necessary to synchronize the time scale of each timer with the external time scale.

For the synchronization of five event timers, timescale alignment is used. Before starting the experiment, each timer was measured to calculate the difference Δt between the 1PPS (Pulse per second) time-tag and the course time for each timer. Fot this purpose, 32 × 1 PPS signals are applied to each event timer. Equation (1) was used to calculate the time difference Δt.

$$\Delta t = \frac{1}{N}\sum_{i=1}^{N}\left(t_{PPS_i} - t_{UTC_i}\right), \quad (1)$$

where t_{UTC} is the PC course time (1 sec. resolution); t_{PPS} is the Time-tag of 1PPS signal measured by event timer.

III. Experimental Study Setup

The first prototype of a five-channel system was developed to ensure five-channel synchronisation. The first prototype block diagram is shown in Fig. 1. The principle of the prototype is to ensure that all channels work in the same timescale. The prototype consists of five independent event timers, AFG (Arbitrary Function Generator), reference clock active splitter and managed equal delay multiplexer. AFG generates 10 MHz reference clock and event signals (1 PPS). A clock signal is simultaneously applied to all channels using an active splitter. The event signal is applied to each channel sequentially with a known identical delay using managed equal delay multiplexer. All five event timers and managed delay multiplexers are connected to the PC from which they are controlled.

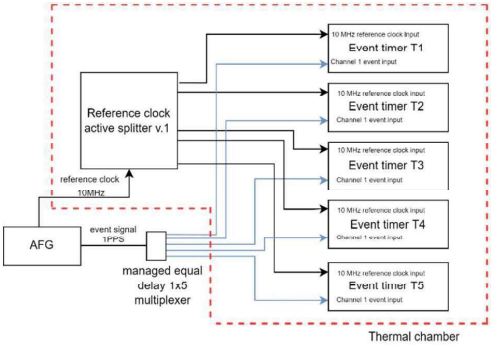


Fig. 1. Experimental setup.

Event timers and reference clock active splitter are placed in the thermal chamber. The temperature in the thermal chamber changed according to the curve in Fig. 2. Temperature changed evenly from 15 to 30 °C within 90 minutes, kept its peak value for 30 minutes, and then changed back to 15 °C within 90 minutes. System initial calibration has been done at the temperature of 22.5 °C.

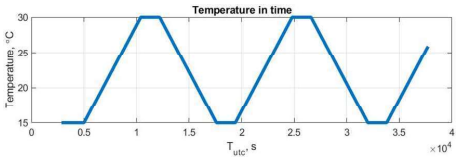


Fig. 2. The curve of temperature in time of the thermal chamber.

IV. Thermal Stability Testing Results

The following parameters were calculated during the experiment: timescale drift was calculated using equation (2), equation (3) is for the timescale difference of each pair of timers, and RMSE (Root-mean-square error) was calculated using equation (4).

$$t_drift = t_{tag_sync} - t_{utc}. \quad (2)$$

$$Dt_{tag_sync} = \Delta t_{tag_sync_n} - \Delta t_{tag_{sync_m}}. \quad (3)$$

$$RMSE = \sqrt{\frac{\sum(Dt_{tag_sync_predicted} - Dt_{tag_sync_actual})^2}{N}}. \quad (4)$$

A. Timescale Drift

Fig. 3 shows the timescale drift of each timer, which means the time measurement result and PC time each second. Each colour represents one of the timers.

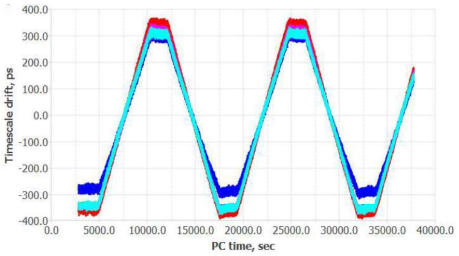


Fig. 3. Timescale drift of all five event timers.

The graphs show that the dynamics of the timescale drift of each of the timers directly corresponds to the temperature change curve. The time scale shifts up to 300 ps at peak temperatures, but within the temperature at which the system was initially calibrated (22.5 °C), the timescale drift value is around 0 s.

B. Timescale Difference

Fig. 4 shows the timescale difference for each pair of timers. The X-axis indicates PC time in seconds; the Y-axis – is the value of the timescale difference of a pair of timers in picoseconds.

According to the results, each pair of timers has its own synchronisation character depending on temperature. In most cases, the nature of the synchronization follows the curve of temperature change. At peak temperatures, the synchronization difference is greatest, and within the temperature at which the system was initially calibrated (22.5°C), the synchronization difference is the smallest.

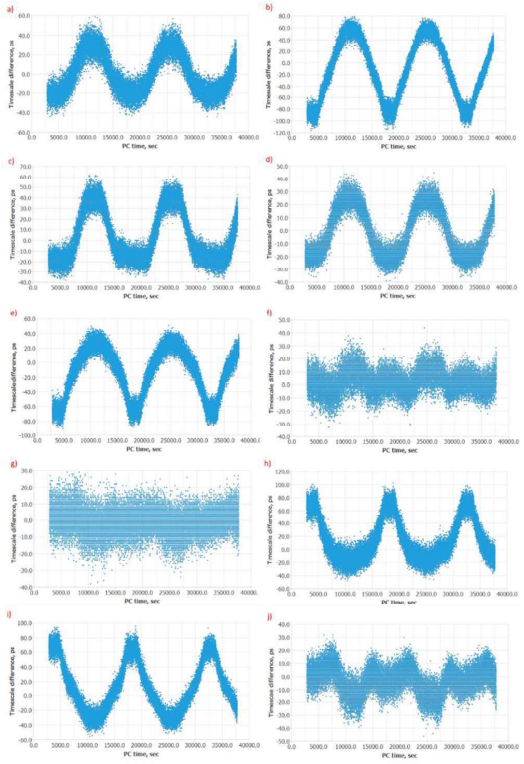


Fig. 4. Timescale difference for each pair of timers.

C. RMSE

Fig. 5 shows a plot of the RMSE value of the timescale difference of each pair of timers. The X-axis shows PC time in seconds. The Y-axis shows the RMSE value in picoseconds. The blue indicates the RMSE value at each point at which the calculation was made; the red is the average value calculated by a sliding window with a step of 100 values.

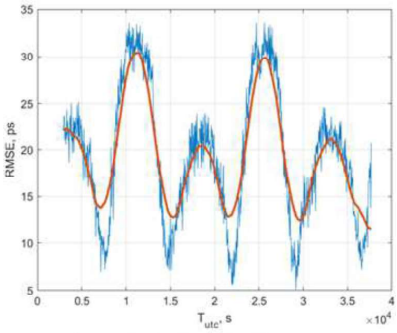


Fig. 5. RMSE plot of one pair of timers.

D. Cross-channel RMSE

Fig. 6 shows the cross-channel RMSE curve. The blue colour shows the RMSE value for each event, and the red line is the average value calculated by sliding the window 800 seconds wide.

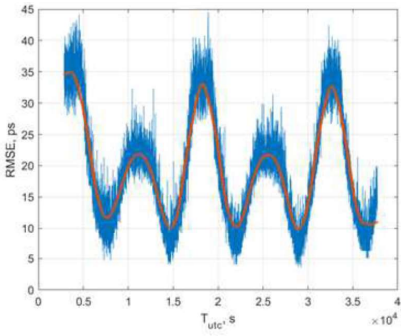


Fig. 6. Cross-channel RMSE.

According to the results, the RMSE parameter has its lowest values at the temperature at which the system has been calibrated.

E. Parameters' Dependence on Temperature

Employing mathematical processing program, graphs of the dependence of the analyzed parameters with temperature were plotted.

The timescale drift-dependence graphs on temperature are shown in Fig. 7. The X-axis indicates the temperature (°C), and the Y-axis shows the value of the time scale shift (ps).

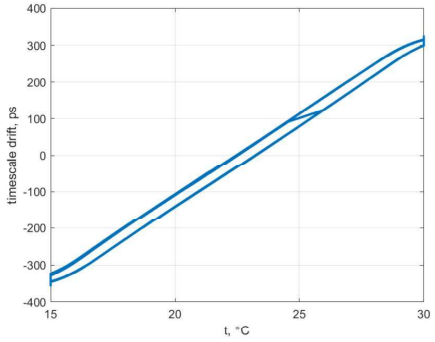


Fig. 7. Timescale drift dependence on temperature.

It is seen that timescale dependence on temperature is linear with a little hysteresis.

Fig. 8 shows a plot of the timescale difference of a pair of timers dependent on temperature for each pair. Temperature (°C) is indicated on the X-axis, and the synchronization difference (ps) value is indicated on the Y-axis.

Fig. 9 shows a plot of the RMSE of each pair of timers dependence on temperature. Temperature (°C) is indicated on the X-axis, RMSE value (ps) is indicated on the Y-axis.

A small hysteresis is visible on the obtained graphs. It may be since the graphs were based on the external temperature readings (the temperature of the thermal chamber). If the graphs were based on the internal temperature (the temperature sensor readings on the timer), the correlation would be better.

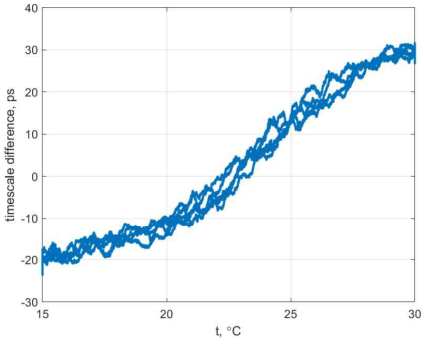


Fig. 8. Timescale difference dependence on temperature.

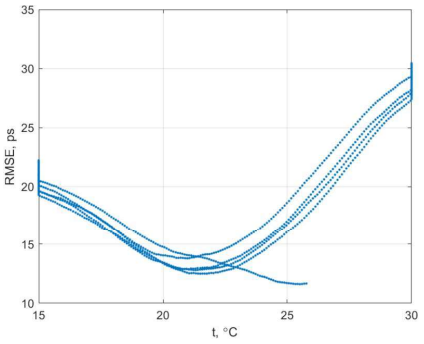


Fig. 9. RMSE dependence on temperature.

V. Conclusion

This research has been devoted to the experimental thermal stability study of a multichannel time-tagging system with picosecond precession. The paper introduces the design of time-tagging systems prototype with five measurement channels and a common timescale. Prototype testing procedures were described and performed. Such parameters as single channel timescale drift, timescale difference and RMSE of each pair of channels were measured and evaluated. After the obtained results analysis, it is evident that:

- The main problem with RMS degradation for multiple measurement channels applying independent timers is that each timer's calibration oscillator and reference PLL are separate. Suppose the calibration oscillator and the PLL are made common. In that case, the problem of deterioration of the RMS will be solved, and the situation with the time scale discrepancy in temperature will be improved.
- An analysis of the noise immunity of the event timer to external influences shows that the timer is unstable to external influences. According to our assumptions, this may be because the timer design is not differential.
- Analysis of the thermal stability of the timer system showed that the timers are insufficiently thermally stable. Based on obtained testing results, to stay within 10 ps RMSE accuracy, the Active Splitter 2.0 system must be recalibrated every 4 degrees of temperature change.

The testing results showed the weaknesses of the system, providing an opportunity for improvement in development and thermal stability enhancement. The future steps include deferential design, the common calibration oscillator and the PLL, thermal calibration procedures development and implementation.

Acknowledgements

This work has been supported by the European Regional Development Fund, project no. 1.1.1.1/20/A/104 "Multi-channel picosecond precision time-tag system with amplitude measurements capability for satellite laser ranging".

References

[1] L. Combrinck "Satellite laser ranging, " in *Sciences of Geodesy-I*, pp. 301–338, springer, 2010.

[2] Y. Cao, L. Zhang, C.-H. Chang, and S. Chen, 'A Low-Power Hybrid RO PUF With Improved Thermal Stability for Lightweight Applications', *IEEE Transactions on Computer-Aided Design of Integrated Circuits and Systems*, vol. 34, no. 7, pp. 1143–1147, Jul. 2015, doi: 10.1109/TCAD.2015.2424955.

[3] A. L. Aita, J. V. De la Cruz, and R. Bashirullah, 'A 0.45V CMOS relaxation oscillator with ±2.5% frequency stability from −55°C to 125°C', in *2015 IEEE International Symposium on Circuits and Systems (ISCAS)*, May 2015, pp. 493–496. doi: 10.1109/ISCAS.2015.7168678.

[4] W. Pan, G. Gong, and J. Li, 'A 20-ps Time-to-Digital Converter (TDC) Implemented in Field-Programmable Gate Array (FPGA) with Automatic Temperature Correction', *IEEE Transactions on Nuclear Science*, vol. 61, no. 3, pp. 1468–1473, Jun. 2014, doi: 10.1109/TNS.2014.2320325.

[5] M. Bachetti *et al.*, 'Timing Calibration of the NuSTAR X-Ray Telescope', *ApJ*, vol. 908, no. 2, p. 184, Feb. 2021, doi: 10.3847/1538-4357/abd1d6.

[6] W. Meng *et al.*, 'High-Precision Single-Photon Laser Time Transfer with Temperature Drift Post-Compensation', *Sensors*, vol. 20, no. 22, p. 6655, Nov. 2020, doi: 10.3390/s20226655.

[7] https://cddis.nasa.gov/2019_Technical_Workshop

[8] Pulkstenis, I., Litviņenko, A., Kurtenoks, V., Lapkovskis, V. Performance Evaluation of Measured Time Stretching Approach for Event Timer. In: 2021 IEEE 9th Workshop on Advances in Information, Electronic and Electrical Engineering (AIEEE 2021), Latvia, Riga, 25-26 November, 2021. Piscataway: IEEE, 2021, pp.46-51. ISBN 978-1-6654-6713-1. e-ISBN 978-1-6654-6712-4. ISSN 2689-7334. e-ISSN 2689-7342. Available from: doi:10.1109/AIEEE54188.2021.9670156

Lapkovskis V., Litvinenko A., **Kurtenoks V.**, Stepanovs V., Smetska V., Bespal'ko V.

Multi-channel synchronization for picosecond time-tagging system.

2023 IEEE 10th Jubilee Workshop on Advances in Information, Electronic and Electrical Engineering (AIEEE), 2023, 81–86.

https://doi.org/10.1109/AIEEE58915.2023.10134773

Multi-channel Synchronization for Picosecond Time-tagging System

Vjaceslavs Lapkovskis
Eventech Ltd. / Riga Technical University
Riga, Latvia
vjaceslavs.lapkovskis@rtu.lv

Anna Litvinenko
Riga Technical university
Signal Processing and Space Electronics Laboratory
Riga, Latvia
Anna.litvinenko@rtu.lv

Viktors Kurtenoks
Eventech Ltd.
Riga, Latvia
v.kurtenoks@eventechsite.com

Vsevolods Stepanovs
Eventech Ltd.
Riga, Latvia
vsevolods.stepanovs@gmail.com

Viktorija Smetska
Eventech Ltd. / Riga Technical University
Riga, Latvia
v.smetskaja@gmail.com

Vladimirs Bespal'ko
Eventech Ltd.
Riga, Latvia
bezpvlad@gmail.com

2023 IEEE 10th Jubilee Workshop on Advances in Information, Electronic and Electrical Engineering (AIEEE) | 979-8-3503-1178-5/23/$31.00 ©2023 IEEE | DOI: 10.1109/AIEEE58915.2023.10134773

***Abstract*—Multichannel Event Timing (ET) systems are scientific instruments digitally processing real-time information from multiple sensors. An experimental study was carried out to investigate the synchronization method of five event timers. Testing is performed on a channel-by-channel basis for events registered separately by each timer channel. The average value of *RMSE* for each timer was computed on the stationary portion, shown on the graphs of each timer from 35000 seconds to the completion of the measurements. The proposed five independent channel synchronization approach analysis is experimentally validated, and the obtained average cross-channel *RMSE* is around 8ps. The temperature stability has not been examined and evaluated, but the observed timescale drift indirectly evidences that thermal compensation approaches should be applied. The experimental studies on the proposed synchronization method will continue to investigate thermal stability and optimize the timer design for 3 ps RMSE precision obtainable.**

Keywords*—Event timer, synchronization methods, Multichannel Event Timing

I. Introduction

Satellite Laser Ranging (SLR) precisely estimates the distance from ground stations to retroreflectors on satellites and the Moon. SLR is an indispensable space geodetic technique for defining the International Terrestrial Reference Frame (ITRF). To better comprehend sea level rise, ocean dynamics, ice mass balance, and terrestrial topography, SLR enables precise orbit determination, instrument calibration, and validation for satellite-based altimeters. It can also investigate lunar dynamics, fundamental constants, and hypotheses.

Multichannel Event Timing (ET) systems are scientific instruments digitally processing real-time information from multiple sensors [1]. In all of these applications, the temporal relationship between events is of the utmost importance and must be preserved and measured precisely.

In multichannel systems, some precautionary measures are required to ensure that the timing relationship between the channels is unaffected by the system's physical configuration or during the A/D conversion of signals from multiple channels.

Acquiring these signals using a common sampling reference is a key technique for maintaining the inherent timing information between channels. All ADCs are simply clocked using the same clock source to accomplish this. The multichannel event timing system simply needs to track when each event set is captured because all signals are digitalized simultaneously. It gives an absolute time reference, which is utilized to derive relative timing information between channels.

Despite being a relatively simple procedure, it can be challenging to execute it accurately, especially when dealing with signals that operate at high frequencies. Even if the event timer ADCs are synchronized from a single clock source, it is still feasible to record signals in which the timing information between channels has been changed during the conversion process. Consider that electrical signals move along the traces of an electronic circuit at a constant, incredibly rapid speed of around 15 cm per nanosecond.

The clock will arrive at ADC #2 six picoseconds after arriving at ADC #1 if there is a one millimeter length difference between the clock traces connected to ADC #1 of the first event timer module and those attached to ADC #2 of the second module.

This is an inaccuracy of twice the event timer's accuracy, which is a substantial amount for an event timer with a 3ps RMS accuracy. Identical signals connected to the first and second timers of a multichannel system would be assumed to have a delay between them when there is none, which means that there isn't much that can be done to eliminate the inherent delay in signals travelling along electrical traces on the surface of a PCB. Trace length matching is a technique that can be used to guarantee that all signals travelling from comparable sources to similar destinations encounter the same delay.

The clock distribution unit makes many identical clock replicas that are all exactly in time with each other. The ADC must receive all signals on the same trace length simultaneously. To maintain the temporal link between these signals, the signal from the input connectors to the ADC inputs must likewise have the same trace length.

Individual measurement channels can no longer rely on their internal clock source in the design of a multi-channel event timer since these clocks are all free-running and asynchronous with respect to each other. ADCs from several modules cannot produce data at the same sampling rate [2].

979-8-3503-1178-5/23/$31.00 ©2023 IEEE

II. Precise Synchronisation Applications

Developers of space and satellite systems must cope with picosecond-scale device synchronization. Unique hardware, algorithms, and software are required to operate at sub-nanosecond or picosecond time intervals and monitor picosecond occurrences. Numerous semiconductor designers investigate picosecond pulse capturing. This paper outlines the construction of a 0.38 ps-accurate high-speed wireless time synchronization chip [3]. The effect of temperature on the precision of information and space systems can result in time delays of up to 20 picoseconds per degree. The approach proposed by Meng et al. [4] can enhance timing precision to 2 picoseconds every 80-second interval. In numerous domains of contemporary science, the precision of calculating time intervals in a few seconds is crucial. For instance, in the case of Very Long Baseline Interferometry, photomultipliers or avalanche diodes are utilized to detect single-photon-level returns. Event timers measure the propagation delay within a few picoseconds [5]. SLR stations with various geographic coordinates also employ time synchronization [6]. The European Union Agency has developed a document on time and synchronization requirements primarily for GNSS applications as part of the Space Programme to clarify the requirements of various businesses for GNSS services [7].

An overview of synchronization methods is presented in the following table

III. Multi-channel Time-tagging Synchronization Method

Event timer metrology is a type of metrology that focuses on the precise measurement and analysis of events that occur within a specified or known time interval. It is utilized in numerous applications, including telecommunications, time-of-flight measurements, precise timing in scientific operations, and time and frequency metrology.

Event timing refers to recording event occurrences with a discrete time scale. The conversion result is the event moment code (time-tagged, time-stamped). Utilizing event timing to examine temporal correlations in event streams. The primary nodes of the event timer are the sensor that detects the event, the periodic clock generator that sets the timescale, and the memory (Figure 1). Typically, there is also a mechanism for synchronizing the event timer's scale with an external (more precise) timescale.

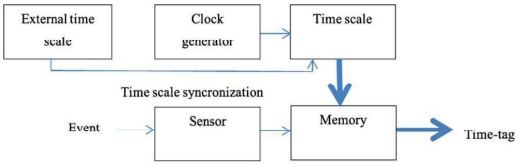


Fig. 1. Event timer nodes.

An experimental investigation examined the synchronization technique of five event timers. Based on Eventech event timers, a prototype with five separate channels has been developed for the performance of the study.

The event timer's time scale is in an arbitrary state when it is turned on. Therefore, even if multiple timers are activated simultaneously, each timer will have a distinct time scale for the same event. Figure 2 demonstrates one example. The time scale of each timer must be synchronized with the external time scale to have identical time tags for the same occurrence.

The review of synchronisation methods in Table I is presented.

TABLE I. Review of Synchronisation Methods

Authors, Reference	Method	Application area	Precision achieved
Kanno et al. [8]	Semiconductor integrated circuit and control method for clock signal synchronisation	Synchronisation control is provided to synchronise clocks and ensures operation so that a phase of two clocks to be compared fits in a range of design values while the power-supply voltage for the first circuit is changed.	5-30 ps
Mari Shridhar et al. [9]	Partial timing synchronisation function (TSF) synchronisation in fine timing measurement (FTM) protocol	Synchronisation between wireless devices	N/A
Reyes et al. [10]	Picosecond clock synchronisation technique for communication and navigation platform equipment	Sensors communication synchronisation	10 ps
Danian Zh., Dong H. [11]	Free-space Synchronisation with Sub-nanosecond Resolution Using Atmospheric Optical Time Transfer	Data transfer and synchronisation	10 ps (of 10 s integral time period)
Vyhlidal D., Cech M. [12, p. 1]	Time-to-Digital Converter With 2.1-ps RMS Single-Shot Precision and Subpicosecond Long-Term and Temperature Stability	SLR systems	2.5-3.4 ps (RMS)
Batysta F. et al. [13]	Picosecond and sub-picosecond laser pulse timing synchronisation by means of a feedback loop based on the measurement of the relative delay in the pulses of a pump and signal laser beams, using their interaction in a nonlinear media.	Laser technologies	N/A
Retterath J.E. et al. [14]	Methods and apparatus for increased precision and improved range in a multiple detector LiDAR arrays	LIDAR (synchronisation clocking methods)	N/A

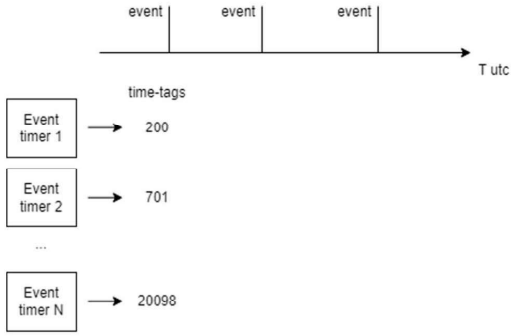


Fig. 2. Time tags of unsynchronised timers.

IV. Experimental Tests and Verification

Testing is performed channel-by-channel for events registered separately by each timer channel. The testing methodology does not differ from the methodology for a one-channel timer.

To test the accuracy of a multichannel timer by measuring the time intervals between events registered by different channels of the timer, it is not necessary to use a precision generator. Applying an input signal to each channel simultaneously or one after the other is sufficient in a known time window (Figure 3). The difference C of the registration results (time tag) of each pair of channels of the event timer is determined. The array of differences $[C]$ is accumulated.

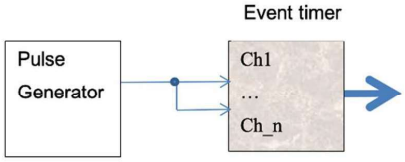


Fig. 3. Pulse generator use for multicannel event time testing.

The variance $D[C]$ for the array of differences $[C]$ makes it possible to estimate the precision of the timer:

$$\sigma = RMS(\text{Single short}) = \sqrt{D[C]}. \quad (1)$$

Timescale alignment is used to synchronize the five event timers. Before starting the experiment, a test measurement was made for each timer. The difference Δt between the 1 PPS (pulse per second) time tag and the running time for each timer was calculated. This is done by applying 32 x 1 PPS signals to each event timer. Considering that the pulse generator's output is insufficient to supply five channels simultaneously with input signals of sufficient voltage, a splitter with equal delay was used. This splitter sequentially applied a signal to each of the timers at the known time interval.

Therefore, the same event will be applied to each timer with a known delay. The events will be pseudo-simultaneous in the following experiment description.

$$\Delta t = \frac{1}{N}\sum_{i=1}^{N}\left(t_{PPS_i} - t_{UTC_i}\right), \quad (2)$$

where t_{UTC} is the PC course time (1 sec. resolution); t_{PPS} is the time-tag of 1 PPS signal measured by event timer.

The Δt value obtained for each timer corrects the time scale. Thus, all timers begin to work on the same time scale, making it possible to verify the experiment setup and test the synchronization method.

A. Five Event Timers Synchronization Method Testing Parameters

During testing, a 1 PPS signal was sent sequentially with a known equal time delay to five timers and the time-tag array of each timer was accumulated.

These parameters of the first multi-channel prototype were tested. The timescale drift of each timer was calculated using this formula:

$$Timescale\ drift\ = t_{tag_{sync}} - t_{utc}, \quad (3)$$

where $t_{tag_{sync}} = t_{tag} - \Delta t$; t_{tag} is the time-tag measured by event timer; $t_{tag_{sync}}$ is the time-tag the corrected with time scale; Δt is the difference between PC course time and 1PPS time tag (described in the previous chapter).

Timescale difference between each pair of event timers. The difference between the time tags of two timers at each event moment was calculated using a mathematical processing software according to the formula:

$$\Delta t_{tag_{sync}} = \Delta t_{tag_{sync_n}} - \Delta t_{tag_{sync_m}}, \quad (4)$$

where n, m is the event timers index number.

RMSE of each pair of event timers were calculated according to the equation:

$$RMSE = \sqrt{\frac{\sum\left(\Delta t_{tag_{sync_{predicted}}} - \Delta t_{tag_{sync_{actual}}}\right)^2}{N}}, \quad (5)$$

where $\Delta t_{tag_{sync_{predicted}}}$ is a predicted value of timescale difference (equals 0); $\Delta t_{tag_{sync_{actual}}}$ is the actual value of timescale difference.

Cross-channel *RMSE* was calculated between all five event timers for each event by the equation:

$$RMSE = \sqrt{\frac{\sum\left(\Delta t_{tag_{sync_{avg}}} - \Delta t_{tag_{sync_n}}\right)^2}{N}}, \quad (6)$$

where $\Delta t_{tag_{sync_{avg}}}$ is the average time-tag (with corrected time scale) of each event timer; $\Delta t_{tag_{sync_n}}$ is the time-tag the corrected with a time scale of each event timer; n is the event timer index number; N is the number of event timers.

To identify each of the timers, the numbering T1… T5 was used, and each pair of timers is designated by a letter and is given in the Table II.

TABLE II. EVENT TIMERS PAIR INDEXES

Index of a pair	a	b	c	d	e	f	g	h	i	j
Pair of timers	T1 - T2	T1 - T3	T1 - T4	T1 - T5	T2 - T3	T2 - T4	T2 - T5	T3 - T4	T3 - T5	T4 - T5

B. Five Event Timers Synchronization Experiment

Five event timer synchronization setup is shown in (Fig. 4). Five V1 timers, an active signal splitter, a frequency generator, and a managed equal delay splitter were used in the experiment.

Before starting the experiment, each timer was measured to calculate the difference Δt between the 1 PPS time tag and the PC course time for each event timer. The calculation of Δt is described in the section above. The Δt value obtained for each timer was used to correct the time scale of the timer.

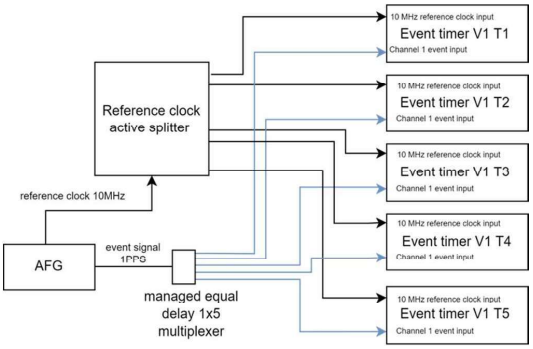


Fig. 4. Experimental setup.

The course of the experiment: 1 PPS signal was applied to five timers through a managed manual splitter 45000 times. Five timers read the PPS signals, and measurement results were registered by the PC and compared with an external time scale (course time). Using the necessary software, the difference between the course time and the measurement result and the synchronization difference between the timers and the *RMSE* parameter were calculated and displayed graphically.

C. Timescale Drift

The time scale drift for a single timer (Timer No 1 is used as an example) (Fig. 5) and for all 5 timers (Fig. 6). The x-axis shows the course time (PC time) in seconds. The y-axis shows the timescale drift value in picoseconds.

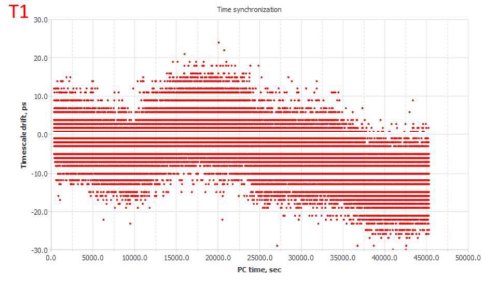


Fig. 5. An example of the time-scale drift for the 1-st timer.

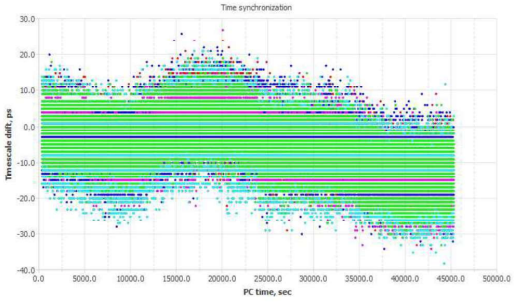


Fig. 6. The time-scale difference of 5 event timers.

It is evident that the timer measurement results' average value almost precisely matches the experiment's initial 10000 seconds of running time. After this period, all three timers deviate by 20 ps. Figure 6 shows that the time difference between the timers remains constant, which indicates that they run synchronously.

The average value of *RMSE* for each timer was computed on the stationary portion, shown on the graphs of each timer from 35000 seconds to the completion of the measurements. The Table III provides a summary of the results.

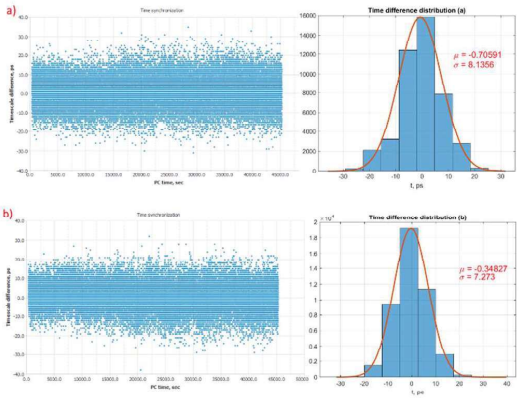


Fig. 7. An example of timescale difference and distribution histogram for two pairs of timers.

TABLE III. EVENT TIMERS AVERAGE *RMSE*

Timer	**T1**	**T2**	**T3**	**T4**	**T5**
RMSE, ps	5.18	5.26	5.91	6.68	5.19

The timescale difference of each pair of event timers has been evaluated during the experimental investigation.

Below is an illustration of the timescale difference between the two timers $\left(\Delta t_{tag_{sync}}\right)$ and a histogram of the distribution of the resulting values (Fig. 7). The generated graphs depict the difference between the two timers' readings at each measurement point. The Y-axis depicts the synchronization difference between the two timers in picoseconds. Each graph bears a symbol corresponding to the index number of a pair of timers. A comparison is made between the distribution histogram for each case and a

standard distribution curve based on the case-specific factors. Histograms display the parameters of the normal distribution curve (μ is the mean value and σ is the standard deviation).

The timing discrepancy between the two timers does not exceed 40 picoseconds, and the average value for all examples approaches zero. Yet, in some instances, the difference between the timers' readings is less than 10 ps, which may imply that they were linked to the same channel. In every instance, the distribution of findings follows the normal distribution.

Despite the timescale drift of each timer during the experiment, the time scales between the timers remain nearly unchanged, which may indicate that the delays have similar characteristics and compensate for one another.

The statistical information about the experimental results is summarised in Table IV.

TABLE IV. STATISTICAL DATA ABOUT THE TIMESCALE

Pair index	Min, ps	Average, ps	Max, ps
a	0	0,706	36
b	0	0,348	40
c	0	2,166	32
d	0	2,256	36
e	0	-0,36	34
f	0	1,45	34
g	0	1,85	40
h	0	1,82	40
i	0	2,21	32
j	0	0,39	32

The *RMSE* value between timers was calculated using the equation:

$$RMSE = \sqrt{\frac{\sum \left(\Delta t_{tag_{sync_{predicted}}} - \Delta t_{tag_{sync_{actual}}} \right)^2}{N}}. \qquad (7)$$

The timescale difference $\left(\Delta t_{tag_{sync}} \right)$ of each pair of timers was used in the calculation. 32 values were used to calculate each *RMSE* point.

The diagram below (Fig. 8) illustrates the *RMSE* for an example pair of timers. The X-axis denotes the course duration in seconds, while the Y-axis represents the *RMSE* in picoseconds.

According to the gathered results, the *RMSE* value between two timers ranges between 7 and 10 ps. Table V summarises the statistical data of the *RMSE* results.

TABLE V. *RMSE* STATISTICAL DATA OF TIMER PAIRS

Pair index	Min, ps	Average, ps	Max, ps
a	4.58	8.05	12.86
b	4.28	7.18	11.29
c	4.83	7.66	11.25
d	2.66	5.8	8.95
e	5.24	8.53	12.14
f	4.80	7.77	11.31
g	3.94	7.69	12.73
h	6.75	10.76	16.4
i	3.84	7.63	12.10
j	4.18	7.35	11.14

Figure 9 below depicts cross-channel *RMSE*. The blue colour represents the *RMSE* value for each occurrence, while the red line represents the average value determined by a 1500-second sliding window. The diagram's right side displays the distribution histogram for cross-channel *RMSE* (Fig. 9).

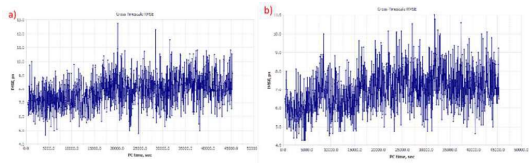


Fig. 8. RMSE of an example pair of event timers.

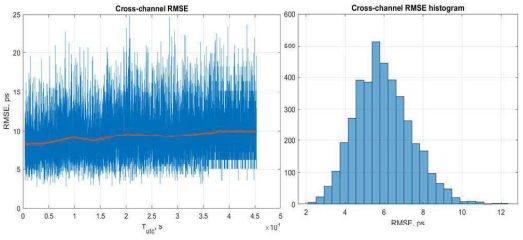


Fig. 9. Cross-channel RMSE and distribution diagrammes.

The average *RMSE* across all channels is 8.26 ps. Although the *RMSE* for some pairings of timers is nonstationary with time, the cross-*RMSE* can be constant.

V. CONCLUSIONS

Increasing the precision of time event synchronization has proven as an incentive for advancing research during the past few decades. Today, picosecond precision for event recording is a frequently utilized time recording method in many scientific disciplines. However, work in the picosecond region necessitates unique techniques at both the hardware and mathematical processing levels. Different implementations of the event registration system for diverse applications in the fields of data transmission, laser technology, identifying the location of celestial bodies and positioning satellites, and exact synchronization of device functioning are examined in this article. The achievable precision ranges are from 2 to 10 ps.

Although investigating the Eventech event timer's present technological solution and its ability to serve as the foundation for a multi-channel event timer has revealed adequately high operational performance, there is still room for improvement. The investigation of the proposed five independent channel synchronization methods is empirically confirmed. The average cross-channel *RMSE* found is around 8ps. This indicates that the technological solution must be optimized. In addition, the temperature stability has not been tested and evaluated, but the observed timeframe drift suggests that thermal compensation strategies should be used. Consequently, experimental research on the suggested synchronization mechanism will be pursued to study thermal stability and refine the timer design to attain a 3 ps *RMSE* accuracy.

ACKNOWLEDGEMENT

This work has been supported by the European Regional Development Fund, project no. 1.1.1.1/20/A/"4 " Multi-channel picosecond precision time-tag system with amplitude measurements capability for satellite laser ranging".

REFERENCES

[1] J. S. Lapington *et al.*, 'Investigating microchannel plate PMTs with TOFPET2 multichannel picosecond timing electronics', *Nuclear Instruments and Methods in Physics Research Section A: Accelerators, Spectrometers, Detectors and Associated Equipment*, vol. 958, p. 162758, Apr. 2020, doi: 10.1016/j.nima.2019.162758.

[2] N. M. Freris, V. S. Borkar, and P. R. Kumar, 'A model-based approach to clock synchronization', in *Proceedings of the 48h IEEE Conference on Decision and Control (CDC) held jointly with 2009 28th Chinese Control Conference*, Dec. 2009, pp. 5744–5749. doi: 10.1109/CDC.2009.5399516.

[3] B. Jamali and A. Babakhani, 'A Self-Mixing Picosecond Impulse Receiver With an On-Chip Antenna for High-Speed Wireless Clock Synchronization', *IEEE Transactions on Microwave Theory and Techniques*, 2018, doi: 10.1109/TMTT.2018.2799843.

[4] W. Meng *et al.*, 'High-Precision Single-Photon Laser Time Transfer with Temperature Drift Post-Compensation', *Sensors*, vol. 20, no. 22, p. 6655, Nov. 2020, doi: 10.3390/s20226655.

[5] W. Schlüter, 'Time and frequency requirements for geodetic space techniques', in *Proceedings of the 20th European Frequency and Time Forum*, Mar. 2006, pp. 405–411.

[6] M. V. Baryshnikov, A. S. Zhabin, S. A. Martynov, M. A. Sadovníkov, A. A. Chubykin, and V. D. Shargorodskiy, 'Test data on high-precision laser equipment for synchronization of the time scales of distributed SLR-stations and GLONASS satellite', in *2016 International Conference Laser Optics (LO)*, Jun. 2016, pp. R6-6-R6-6. doi: 10.1109/LO.2016.7549808.

[7] EU Agency for the Space Programme, 'Report on Time & Synchronisation User Needs and Requirements'. EUSPA, 2021. Accessed: Mar. 11, 2022. [Online]. Available: https://www.gsc-europa.eu/sites/default/files/sites/all/files/Report_on_User_Needs_and_Requirements_Timing_Synchronisation.pdf

[8] Y. Kanno, 'Semiconductor integrated circuit and control method for clock signal synchronization', US8183899B2, May 22, 2012 Accessed: Nov. 25, 2021. [Online]. Available: https://patents.google.com/patent/US8183899B2

[9] C. H. Aldana, 'Partial timing synchronization function (TSF) synchronization in fine timing meas urement (FTM) protocol', AU2016307332B2, Mar. 14, 2019 Accessed: Nov. 25, 2021. [Online]. Available: https://patents.google.com/patent/AU2016307332B2

[10] G. M. Reyes, J. H. Timmerman, J. H. Doty, P. Y. Hwang, G. Peng, and G. A. McGraw, 'Picosecond clock synchronization technique for communication and navigation platform equipment', US9596073B1, Mar. 14, 2017 Accessed: Oct. 29, 2021. [Online]. Available: https://patents.google.com/patent/US9596073B1/en

[11] D. Zhang and D. Hou, 'Free-space Synchronization with Sub-nanosecond Resolution Using Atmospheric Optical Time Transfer', in *2018 IEEE 18th International Conference on Communication Technology (ICCT)*, Oct. 2018, pp. 316–320. doi: 10.1109/ICCT.2018.8600256.

[12] D. Vyhlidal and M. Cech, 'Time-to-Digital Converter With 2.1-ps RMS Single-Shot Precision and Subpicosecond Long-Term and Temperature Stability', *IEEE Transactions on Instrumentation and Measurement*, vol. 65, no. 2, pp. 328–335, Feb. 2016, doi: 10.1109/TIM.2015.2490418.

[13] F. Batysta, R. Antipenkov, J. A. Naylon, J. T. Green, P. Bakule, and J. Novák, 'Method and device for time synchronization of picosecond and subpicosecond laser pulses', EP2899816A1, Jul. 29, 2015 Accessed: Mar. 11, 2022. [Online]. Available: https://patents.google.com/patent/EP2899816A1/en

[14] J. E. Retterath and R. A. Laumeyer, 'Methods and apparatus for increased precision and improved range in a multiple detector LiDAR array', US11226398B2, Jan. 18, 2022 Accessed: Mar. 11, 2022. [Online]. Available: https://patents.google.com/patent/US11226398B2/en?q=picosecond+event+synchronisation&oq=picosecond+event+synchronisation

[15] G. Satat, M. Tancik, and R. Raskar, 'Lensless Imaging With Compressive Ultrafast Sensing', *IEEE Transactions on Computational Imaging*, vol. 3, no. 3, pp. 398–407, Sep. 2017, doi: 10.1109/TCI.2017.2684624.

[16] H. Yang *et al.*, 'Picosecond-precision optical two-way time transfer in free space using flexible binary offset carrier modulation', *OSA Continuum, OSAC*, vol. 3, no. 5, pp. 1264–1273, May 2020, doi: 10.1364/OSAC.384721.

Bespal'ko V., Litvinenko A., Stepanovs V., **Kurtenoks V.**, Smetska V., Lapkovskis V.

Compensation of Accuracy Error for Time Interval Measurements.

Latvian Journal of Physics and Technical Sciences, 2024, 61(1), 43–51.

https://doi.org/10.2478/lpts-2024-0005

sciendo

LATVIAN JOURNAL OF PHYSICS
AND TECHNICAL SCIENCES
2024, N 1

DOI: 10.2478/lpts-2024-0005

COMPENSATION OF ACCURACY ERROR FOR TIME INTERVAL MEASUREMENTS

V. Bespal'ko[1], A. Litvinenko[2], V. Stepanovs[1],
V. Kurtenoks[1], V. Smetska[1,2], V. Lapkovskis[1,2]*

[1]Eventech Ltd.,
3 Pulka Str., Riga, LV-1007, LATVIA
[2]Riga Technical University, Institute of Radio Electronics,
12 Azenes Str., Riga, LV-1048 LATVIA
*e-mail: vjaceslavs.lapkovskis@rtu.lv

A method of accuracy error compensation for the time interval is examined, allowing to decrease the dependence of accuracy error on the duration of measured intervals and minimising the influence of destabilising factors – ambient temperature changes and the initial deviation of the meter clock generator frequency from the nominal value. The compensation method is based on a calibration procedure that measures precise time intervals under conditions of changing ambient temperature. Then the dependence of the accuracy error on temperature for a particular meter is recorded. Based on these data, a correction table is compiled containing correction factors and temperature values at which these factors were determined. Under real measurement conditions, the correction factor corresponding to the current temperature is determined from the table for measured result correction. The table with correction factor values could be stored in the memory of the meter or processing computer. Experimental verification of the method showed that applying a correction for a meter with a standard XO class clock generator (certificated instability of ±50 ppm) could obtain an equivalent clock generator instability of ±0.15 ppm. The application of the method is efficient in cases where the use of high-end clocking to ensure the required measurement accuracy is not economically feasible.

Keywords: *Accuracy error compensation, clock generator, correction of measurement results, measurement of time intervals.*

1. INTRODUCTION

Time measurements (time-to-digital conversion) [1]–[4] have always belonged to the class of the most demanded measurements since it is reasonable to reduce measurements of many heterogeneous physical quantities to time measurements. As modern methods and instruments for measuring time provide very high accuracy [5], these technologies are in demand in a wide range of fields and industries [6], [7]. The most commonly used time measurements are measurements of time intervals (TI) between the start and stop input signals [8], [9]. For a significant part of the experiments, the object of investigation is the time relations between initialising and secondary events [10], [11].

In the analysis of measurement errors of time intervals, we assume that the result A_i of the i-th measurement is, in general, a random variable and can be represented as a sum of the measured quantity T_i and the absolute error of its measurement a_i:

$$A_i = T_i + a_i .$$

The absolute measurement error a_i can, in turn, be represented as the sum of the random Δ_{ir}, accuracy Δ_{is} and offset Δ_c components of the total error [12], therefore:

$$A_i = T_i + a_i = T_i + \Delta_{ir} + \Delta_{is} + \Delta_c. \quad (1)$$

The random error (or precision error) Δ_{ir} has an unpredictable value and represents the scatter of the measurement results due to the influence of noise of different origin.

The accuracy error is determined by the repeatability of its value from measurement to measurement. However, the value of this error Δ_{is} itself depends on several parameters. The characteristic of the accuracy error in TI measurement is its multiplicative character, i.e., the value of Δ_{is} is proportional to the duration of the measured TI.

The offset error is determined by the difference between the delays of the start and stop channels and is additive. Its value Δ_c is offset for a particular meter. The offset error can be determined and used to correct the measurement results accordingly.

Let us suppose that the task is to test a meter. In that case, the value of T_i in (1) is generally unknown since the source (generator) of input signals possesses its errors (Accuracy, Offset, Jitter). Ti can be represented as the sum of the generator set value T_g, generator accuracy error Δ_{isg}, generator constant error Δ_{cg} and jitter of the TI generator Δ_{irg}. Therefore, the general equation of the measurement result is as follows:

$$A_i = T_i + a_i = T_g + \Delta_{irg} + \Delta_{isg} + \Delta_{cg} + \Delta_{ir} + \Delta_{is} + \Delta_c. \quad (2)$$

A graphical interpretation of the generation and measurement errors is illustrated in Fig. 1.

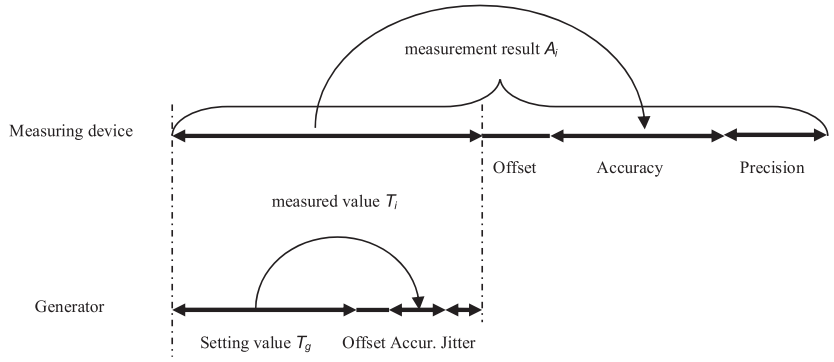


Fig. 1. Graphical interpretation of the generation and measurement errors of the time intervals.

The accuracy error Δ_{is} in the TI measurement is determined by the stability level of the clock generator (CG) of the meter and is caused by the fact that the period F of the CG differs from the nominal value F_0 by τ. The value of τ is not constant and depends on four factors: changes in ambient temperature, the value of the initial deviation from F_0, variations in the generator supply voltage and ageing of its components.

In the specifications of a CG, the maximum value of its relative stability is K_{max}, defined as ratio $K_{max}=\pm\tau_{max}/F_0$, where τ_{max} takes into account all destabilising factors. According to the methods of minimising the influence of destabilising factors, CGs are divided into stability classes [13], [14]: standard XO (Crystal Oscillator), thermo-compensated TCXO (Temperature Compensated Crystal Oscillators), thermo-stated OCXO (Oven Controlled Crystal Oscillators), microprocessor-corrected MCXO (Microprocessor Corrected Crystal Oscillator), and atomic standards.

Reducing the accuracy error is relatively easy to achieve by using high-end CG in the meter. However, for specific applications (e.g., space electronics), such a solution is not always feasible due to the high cost of high-class CGs, as the main cost component of space-level CGs is the testing procedure. In this paper, the problem of significant reduction of the accuracy error without increasing the CG class of the TI meter is solved.

2. ESTIMATION OF ACCURACY ERROR

When measuring time intervals, the result of measurement A_i is proportional to the period of CG F, which determines the multiplicative nature of the accuracy error, and its value Δ_s increases proportionally to the duration of measured TI. The maximum value of accuracy error Δ_{smax} is usually the parameter of the meter, which can be estimated based on the certificate value K_{max} for the applied CG and A_{max} value, corresponding to the upper limit of the range of measured TI durations: $\Delta_{smax} = K_{max} \cdot A_{max}$.

The experience shows that the K_{max} value of a particular CG for the specific temperature conditions of its application can be much less than the value taken from its specification data. Respectively, the real value of Δ_{smax} can also be several times less.

Therefore, the first step in reducing the accuracy error is to estimate the Δ_{smax} value of a particular CG meter.

Evaluation of Δ_{smax} of a particular TI meter is based on measurement and accumulation of an array *[A]* of *n* results of the TI measurement (Fig. 2) for the case of measuring input TI of maximum duration T_{gmax} when the ambient temperature $t°$ changes in the operating temperature range of the meter. Based on (2), it can be assumed that the average value of the array of measurement results at temperature $t°$ will be:

$$\bar{A}_{t^\circ max} = T_{g\,max} + \Delta_{cg} + \Delta_{cg} + \Delta_{t^\circ s} + \Delta_c . \quad (3)$$

In this case, we assume zero values of the meter's random error and the TI oscillator's jitter. The influence of the accuracy error of the generator Δ_{sg} included in this expression can be neglected if the stability of its CG is 1–2 classes higher than the CG stability of the TI meter under study. Thus, Fig. 2 shows the use of an external OCXO (reference oscillator). In this case, Expression (3) is simplified:

$$\bar{A}_{t^\circ max} = T_{g\,max} + \Delta_{cg} + \Delta_{t^\circ s} + \Delta_c . \quad (4)$$

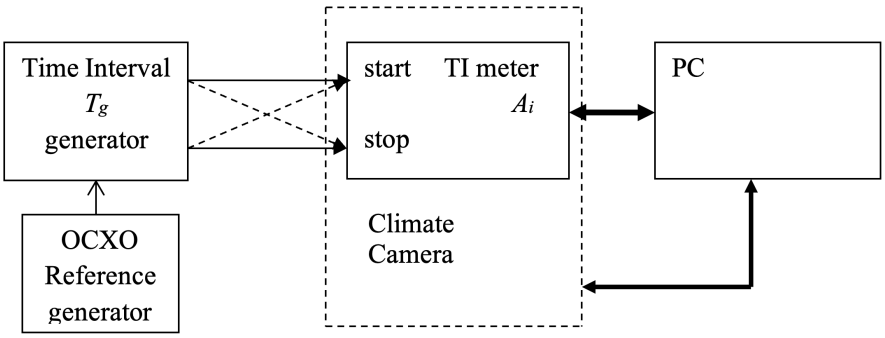


Fig. 2. Flow chart of the systematic and constant error estimation of the TI meter.

Equation (4) used to evaluate the accuracy error $\Delta_{t^\circ c}$ is complicated due to the presence of unknown error constants Δ_{cg} and Δ_c in the expression. The value of Δ_c is determined by the difference in delays for the start and stop inputs of the TI meter. In turn, Δ_{cg} is determined by the difference in delays in the TI meter start and stop signal generation circuitry and the difference in the lengths of the connection wires.

It is possible to estimate the values of Δ_{cg} and Δ_c when two conditions are met. Firstly, the TI must be measured with a minimum duration of T_{gmin}, which allows for omitting the accuracy errors of the generator Δ_{sg} and the measurer Δ_s, then:

$$\bar{A}_{min} = T_{g\,min} + \Delta_{cg} + \Delta_c .$$

Secondly, additional measurements are required when the wires are cross-connected to the meter inputs (shown in dashed in Fig. 2), and the sign of inter-channel delay of the TI generator is changed. In this case, a system of equations can be formulated:

$$\bar{A}_{1\,min} = 2T_{g\,min} + \Delta_{cg} + \Delta_c ;$$

$$\bar{A}_{2\,min} = 2T_{g\,min} - \Delta_{cg} + \Delta_c .$$

This implies that:

$$\Delta_{cg} = \frac{\bar{A}_{1max} - \bar{A}_{2max}}{2};$$

$$\Delta_c = \frac{\bar{A}_{1max} + \bar{A}_{2max} - 2T_{g\,min}}{2}.$$

Estimation of the error constant of the meter relative to its inputs Δ_c is an independent value, but, at the same time, it provides the capability for estimation of $\Delta_{t^\circ s}$:

$$\Delta_{t^\circ s} = \bar{A} - \left(T_{g\,max} + \Delta_{cg} + \Delta_c\right) = \frac{1}{n}\sum_{i=1}^{n} A_{t^\circ i} - \left(T_{g\,max} + \Delta_{cg} + \Delta_c\right). \quad (5)$$

While testing the meter in a climate chamber within the meter's operating temperature range (Fig. 2), a dependence of $\Delta_{t^\circ s}$ on ambient temperature changes $t°$ can be derived by TI measurement of maximum duration T_{gmax}. The graphical representation provides a capability to estimate the value of Δ_{smax} for a particular TI meter and the actual stability of its clock generator $K_{max}=\pm\Delta_{smax}/T_{gmax}$.

Figure 3 shows an example of the plot of change of Δ_s as a function of temperature for a TI meter with a standard XO class clock generator (according to its specification $K_{max}=\pm 50$ ppm). The dependence character in the operating temperature range of the meter (- 40 °C ÷ +60 °C) is of a pronounced non-linear nature and corresponds to the frequency-temperature characteristics of quartz AT-slice plates.

Based on Fig. 3, Δ_{smax}=740 ps and T_{gmax}=134 μs; hence, the estimate of $K_{max}=\pm 740\cdot 10^{-12}/134\cdot 10^{-6}= 5.5\cdot 10^{-6}=\pm 5.5$ ppm. The estimation of K_{max} obtained in this way is underestimated since it does not take into account the influence of instability of the generator supply voltage and the ageing of its components. Nevertheless, the difference between the specification listed and the actual component's parameter values is sufficient.

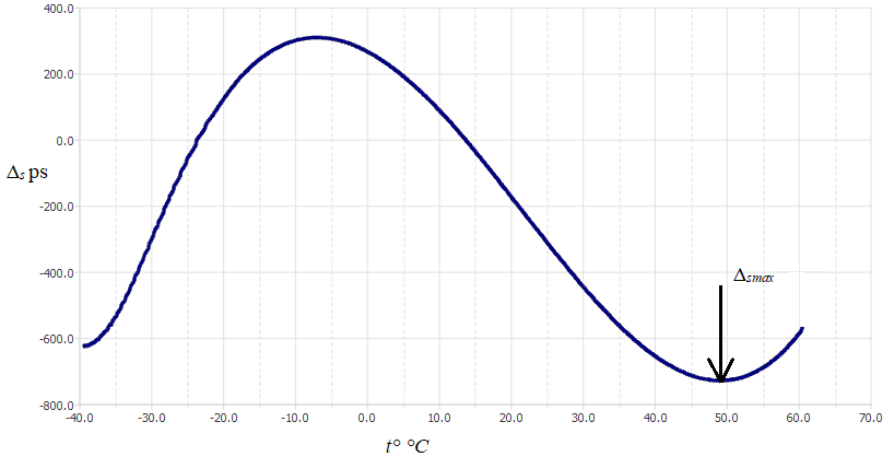


Fig. 3. The temperature dependence Δ_s for an XO standard class TI meter when measuring TI with a duration of T_{gmax}=134 μs.

3. COMPENSATION FOR ACCURACY ERROR

The investigation of the dependence of the accuracy error value Δ_s on the temperature for a particular CG provides the capability to perform a procedure for offsetting the influence of the accuracy error on the measurement result.

The compensation procedure is based on a special calibration, during which a series of high-precision TI measurements are carried out under changing ambient temperature $t°$. This is done by determining the average values of the TI measurement $\bar{A}_{t°}$ and the accuracy error $\Delta_{t°s}$ for the current temperature $t°$ according to (5). The correction factors $K_{t°}=\Delta_{t°s}/\bar{A}_{t°}$ and the corresponding temperature calculated from these data are recorded as a table of $K_{t°}$ and $t°$ values in the memory of the meter or processing computer.

Considering the non-linear nature of the relationship between the accuracy error and temperature (Fig. 3), the choice of a table to record the relationship between the correction factors and temperature is the simplest method, although it requires memory resources.

Several conditions have to be met during calibration: the CG class of the TI generator must be higher than the CG class of the measured (compensated) meter, the results of the calibration measurements must be averaged to increase the accuracy of the table, and the T_{gmax} value must correspond to the maximum working range of the TI durations to be measured.

In general, calibration should be carried out under the real conditions of the meter's use or its equivalent. For example, if we are talking about space applications, then calibration must be carried out under thermovacuum conditions.

To implement the procedure for compensating for the accuracy error under actual measurement conditions, it is essential to monitor the current temperature $t°$. The algorithm for compensation of the i-th measurement result consists of extracting from the table the $K_{t°}$ coefficient corresponding to the temperature $t°$ at the time of measurement and calculating the compensated measurement result $A_{t°i}$: $com A_{t°i}=A_{t°i}(1-K_{t°})$.

In a general case, the measurement result $A_{t°i}$ contains both an accuracy error and a constant error Δ_c, so $com A_{t°i}=(A_{t°i}-\Delta_c)(1-K_{t°})$. Figure 4 represents the dependence of the accuracy error Δ_s on the temperature after the compensation of the accuracy error shown in Fig. 3. The value of Δ_{smax} decreased from 740 ps to 20 ps, and the equivalent stability of CG, in this case, reached a value of ±0.15 ppm.

The compensation procedure also has its limitations since it does not consider the influence of instability of CG supply voltage and the ageing of its components.

As in the proposed solution, a variant of accuracy error minimisation implying a pre-calibration procedure is presented in [15]. This option is based not on the correction of measurement results but on microprocessor correction of frequency of VCXO class CG, the frequency of which is controlled by DAC voltage.

The microprocessor performs the calibration by the user. As a result of this procedure, the coefficients of the 4th-degree polynomial are determined and stored. These coefficients are used to calculate the DAC codes, which compensate the VCXO frequency deviation for the current temperature value $t°$. The CGs based on this principle belong to the CCXO (Coefficient Corrected Oscillator) class and can

ensure the stability of the CG at the level of 0.1÷0.3 ppb. In its application, there is no need to manually correct measurement results, but the cost of such CGs is high, and at this time, it is not manufactured for the space-level ready version.

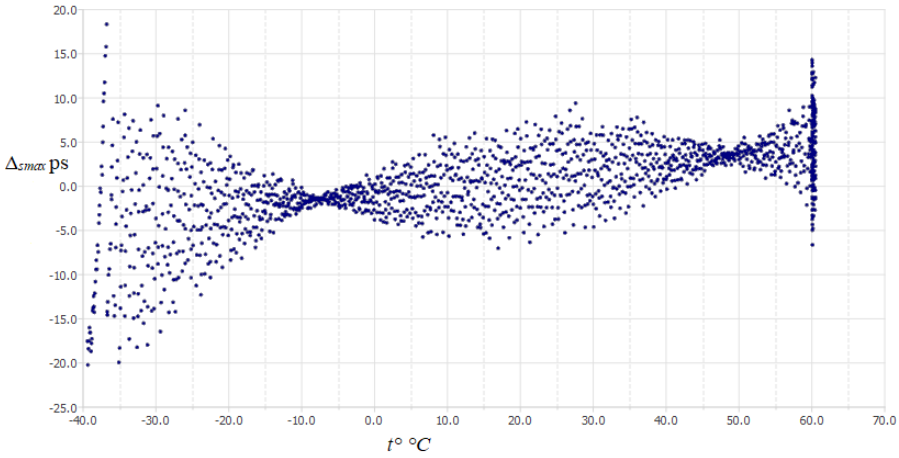


Fig. 4. Dependence of the accuracy error value Δs to the temperature after compensation.

4. CONCLUSIONS

The accuracy error at measuring time intervals (TI) is determined by the relative stability of the clock generator (CG) used in a meter and the duration of the measured time interval. The discussed method of accuracy error compensation eliminates the dependence of accuracy error on the duration of measured TI. It reduces to a minimum the influence of such destabilising factors as changes in ambient temperature and initial deviation of the clock frequency from its nominal value.

To implement the compensation method, three procedures have been developed: a procedure for registering an accuracy error, a calibration procedure in which a correction table is generated, and a procedure for correcting measurement results in real conditions of the meter's application. The main expenditures of implementing the method consist primarily in correctly conducting the meter's calibration, and hardware support for temperature monitoring and performing relatively straightforward computational operations is also required. The main costs of the method implementation primarily consider the correct calibration of the meter, as well as the required hardware support for temperature monitoring and relatively simple computational operation performance.

Experimental validation of the method demonstrated that an equivalent instability of ±0.15 ppm could be achieved for a standard class XO meter (specification instability of ±50 ppm), which reduced the accuracy error to the equivalent degree. The accuracy error compensation procedure has its limitations related to the replicability of the field conditions in which the calibration

procedure has been performed.

Implementation of the described method of systematic error compensation has limited feasibility in terrestrial applications, when a given level of systematic error in time interval measurement can be obtained without much cost by simple selection of the required clock class. In space electronics, replacement of a complex high class clock by a simple standard XO class clock not only reduces significantly the cost of electronics, but in combination with simple computational operations, performed by an on-board computer, it also increases manifold the reliability of the CG. Modern capabilities for resetting the onboard computer increase another important parameter for space electronics – the survivability of the CG.

Systematic error compensation procedure has its limitations related to reproducing real conditions of instrument application during the calibration procedure. However, the pre-flight preparation of the electronics includes a mandatory TVC (Thermal Vacuum Cycle) procedure, during which calibration is possible. Also, space electronics are equipped with obligatory hardware support to monitor temperature, voltage and power supply levels to ensure reliability of measurement results. The above considerations make it possible to achieve a good balance between the cost of the method and its effectiveness.

ACKNOWLEDGEMENTS

The research has been supported by the European Regional Development Fund, project no. 1.1.1.1/20/A/104 “Multichannel Picosecond Precision Time-Tag System with Amplitude Measurements Capability for Satellite Laser Ranging”.

REFERENCES

1. Maichen, W. (2006). *Digital Timing Measurements: From Scopes and Probes to Timing and Jitter* (vol. 33). Springer US. https://doi.org/10.1007/978-0-387-31419-8
2. Alahdab, S., Mäntyniemi, A., & Kostamovaara, J. (2013). Review of a Time-to-Digital Converter (TDC) Based on Cyclic Time Domain Successive Approximation Interpolator Method with sub-ps-level Resolution. *2013 IEEE Nordic-Mediterranean Workshop on Time-to-Digital Converters (NoMe TDC)*, 1–5. https://doi.org/10.1109/NoMeTDC.2013.6658237
3. Tancock, S., Rarity, J., & Dahnoun, N. (2021). Developments in Time-to-Digital Converters during 2020. *2021 7th International Conference on Event-Based Control, Communication, and Signal Processing (EBCCSP)*, 1–5. https://doi.org/10.1109/EBCCSP53293.2021.9502397
4. El-Hadbi, A., Elissati, O., & Fesquet, L. (2019). Time-to-Digital Converters: A Literature Review and New Perspectives. *2019 5th International Conference on Event-Based Control, Communication, and Signal Processing (EBCCSP)*, 1–8. https://doi.org/10.1109/EBCCSP.2019.8836857
5. Johansson, S. (2021). Parallel, Multi-Channel Frequency & Time Measurements, with Picosecond Resolution. *Sensors & Transducers*, *254* (7), 1–9.
6. Gan, Q., Wang, W., Liu, Y., & Liu, W. (2022). Study on the High Precision Time-Interval Measurement System Based on FPGA and TDC_GP22. *9th International Symposium on Test Automation & Instrumentation (ISTAI 2022)*, 380–382. https://doi.org/10.1049/icp.2022.3253

7. Li, X. (2011). The Application Research Based on High-Precision's Measurement Method of Time Interval. *2011 International Conference on Multimedia Technology*, 3713–3715. https://doi.org/10.1109/ICMT.2011.6002696
8. Szplet, R., Kwiatkowski, P., Jachna, Z., & Różyc, K. (2016). An Eight-Channel 4.5-ps Precision Timestamps-Based Time Interval Counter in FPGA Chip. *IEEE Transactions on Instrumentation and Measurement*, *65* (9), 2088–2100. https://doi.org/10.1109/TIM.2016.2564038
9. Zhao, J., Zhao, Z., & Fu, L. (2017). Research on the High Resolution Precision Time-interval Measurement Methods. *Procedia Engineering*, *174*, 1257–1261. https://doi.org/10.1016/j.proeng.2017.01.298
10. Raina, H., Sankannawar, P., Sawant, V., & More, J. (2022). Implementation of Multi-Channel Time-to-Digital Converter using FPGA. *2022 2nd International Conference on Intelligent Technologies (CONIT)*, 1–6. https://doi.org/10.1109/CONIT55038.2022.9847891
11. Nissinen, J., Nissinen, I., & Kostamovaara, J. (2009). Integrated Receiver Including Both Receiver Channel and TDC for a Pulsed Time-of-Flight Laser Rangefinder with cm-Level Accuracy. *IEEE Journal of Solid-State Circuits*, *44* (5), 1486–1497. https://doi.org/10.1109/JSSC.2009.2017006
12. Crowder, S., Delker, C., Forrest, E., & Martin, N. (2020). *Introduction to Statistics in Metrology*. Springer Nature.
13. Rutkowski, R. (n.d.). *Crystal Oscillators: The Beginners Guide (OCXO, TCXO, VCXO, Clocks)*. Available at https://blog.bliley.com/quartz-crystal-oscillators-guide-ocxo-tcxo-vcxo-clocks
14. *Quartz Crystal Cuts: AT, BT, SC, CT. Electronics Notes*. (n.d.). Available at https://www.electronics-notes.com/articles/electronic_components/quartz-crystal-xtal/crystal-resonator-cuts-at-bt-sc-ct.php
15. Vectron International. (2014). *Application Note. Coefficient Corrected Oscillator—CCXO.* Available at https://www.vectron.com/products/literature_library/Coefficient_Corrected_Oscillator_Application_Note.pdf

Tatarinovs A., Serdjuks D., Buka-Vaivade K., **Kurtenoks V.,** Mironovs V.

Method for non-destructive testing of building structures.

Patent LV15647B, 2022.

https://databases.lrpv.gov.lv/patents/LVP2021000034

LATVIJAS REPUBLIKA

PATENTS

Patentu valde apliecina, ka šajā patentā ietvertais izgudrojums ir iekļauts Patentu reģistrā ar

Nr. 15647

Patents ir spēkā Latvijas Republikā 20 gadu no 01.06.2021., ja šis termiņš Patentu likumā paredzētajā gadījumā nebeidzas agrāk

Rīga
20.09.2022.

Patentu valdes direktors
Agris Batalauskis

LV 15647

(19) LATVIJAS REPUBLIKAS
PATENTU VALDE

(11) LV 15647 B1

(51) Starpt.pat.kl. E04B 1/92
H05K 9/00

Latvijas patents izgudrojumam
2007g. 15.februāra Latvijas Republikas likums

(12) Īsziņas

(21) Pieteikuma numurs: LVP2021000034

(22) Pieteikuma datums: 01.06.2021

(43) Pieteikuma publikācijas datums: 20.06.2022

(45) Patenta publikācijas datums: 20.09.2022

(71) Īpašnieks(i):
RĪGAS TEHNISKĀ UNIVERSITĀTE,Kaļķu iela 1,Rīga,LV

(72) Izgudrotājs(i):
Aleksejs TATARINOVS (LV)
Dmitrijs SERDJUKS (LV)
Karīna BUKA-VAIVADE (LV)
Viktors KURTENOKS (LV)
Viktors MIRONOVS (LV)

(54) Izgudrojuma nosaukums: METODE BŪVKONSTRUKCIJU NESAGRAUJOŠAI KONTROLEI
METHOD FOR NON-DESTRUCTIVE TESTING OF BUILDING STRUCTURES

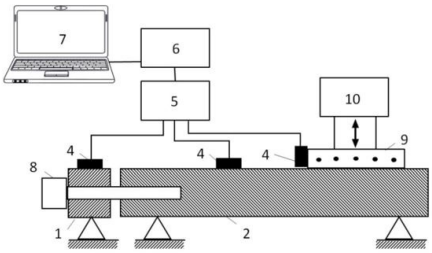
(57) Kopsavilkums:

Izgudrojums attiecas uz būvražošanas jomu, uz metodēm ēku konstrukciju nesagraujošai kontrolei. Izgudrojums var tikt izmantots arī mašīnbūvē, aviācijā un citās nozarēs.

Izgudrojuma mērķis ir izstrādāt metodi būvkonstrukciju savienojošo mezglu nesagraujošai kontrolei, kas nodrošinās pieliekamās trieciena—vibrācijas slodzes paplašinātu parametru diapazonu, kā arī nodrošinās vienlaicīgu atbildes signālu fiksāciju, izmantojot tam vairākus lineāros un leņķiskos akselerometrus (4).

Būvkonstrukciju savienojošo mezglu nesagraujošas kontroles metodes shēma ietver šādas sastāvdaļas: trieciena ierīci (3) vai induktoru (9) un impulsa ģeneratoru (10), akselerometru (4), impulsa uztvērēju (5), signāla analizatoru (6) un datoru (7). Izgudrojuma metode paredz iegūto datu (atbildes signālu) turpmāko analīzi, kontrolējot korelācijas funkciju no koaksiālajiem trīs lineārajiem un trīs leņķiskajiem paātrinājumiem, kurus mēra akselerometri (4), tādā veidā raksturojot būvkonstrukcijas elementu (1) un (2) savienojuma mezglu ar sešiem paātrinājumiem attiecībā pret slodzes pielikšanas vietu.

Lai nodrošinātu metodes augstu efektivitāti un pieliekamas slodzes plaša diapazona parametru regulēšanu, būvkonstrukcijas slogošanai izmanto impulsa elektromagnētisko lauku ar intensitāti 10–100 MA/m, un iespēju regulēt impulsa amplitūdu un frekvenci, kā arī slogošanas ātrumu. Slogošanu var veikt ar vienu impulsu vai vairākiem secīgiem impulsiem ar frekvenci no 1 līdz 30 impulsiem minūtē.



IZGUDROJUMA APRAKSTS

[001] Izgudrojums attiecas uz būvražošanas jomu, uz metodēm ēku konstrukciju nesagraujošai kontrolei. Izgudrojums var tikt izmantots arī mašīnbūvē, aviācijā un citās nozarēs.

Zināmais tehnikas līmenis

[002] Ir zināma eksperimentālā metode būvkonstrukciju stāvokļa novērtēšanai, slogojot būvkonstrukcijas ar statisko slodzi. Metodes pamatā ir būvkonstrukcijas slogošana ar pakāpeniski pieaugošo nekustīgo slodzi un attiecīgi iegūto deformāciju novērtēšana [1]. Šo metodi izmanto būvkonstrukcijas tehniskā stāvokļa novērtēšanai gadījumos, kad ar citām zināmām metodēm to nav iespējams izdarīt, jo šī metode ir laika un darbietilpīga, mazinformatīva un dažos gadījumos ir pat bīstama, jo būvkonstrukcija slogošanas rezultātā var tikt sagrauta vai neatgriezeniski bojāta.

[003] Ir zināmas nesagraujošas kontroles metodes, kas ļauj atklāt defektus būvkonstrukciju elementos, iedarbojoties uz būvkonstrukciju ar impulsa slodzi. Betona un citu līdzīgu būvmateriālu kvalitātes kontrolei izmanto sklerometrus (Šmita āmurus). Šmita āmuru darbības princips balstās uz trieciena impulsa noteikšanu, kas rodas pēc impulsa slodzes pielikšanas. Trieciena enerģija betona spiedes stiprības pārbaudei ir 2,207 Nm. Ir zināmi Šmita āmuri ar samazinātu trieciena enerģiju citiem materiāliem vai plānsienu konstrukcijām [2]. Betona stiprību nosaka pēc Šmita āmura stieņa atsitiena augstuma, izmantojot noteiktās kalibrēšanas līknes. Sklerometriskā testa pamatā ir korelācija starp betona spiedes stiprību un tā virsmas cietību [3]. Ja Šmita āmura trieciena enerģija ir pietiekama, to var izmantot impulsa slodzes veidošanai uz būvkonstrukcijām, lai veiktu būvkonstrukciju frekvences reakcijas testēšanu jeb modālo analīzi, vai arī šim nolūkam izmantot trieciena āmurus [4]. Būvkonstrukciju tehniskā stāvokļa novērtēšanai impulsu izraisošu iekārtu izmanto kopā ar akselerometriem, kas fiksē būvkonstrukciju reakciju uz impulsa slodzi. Katram trieciena āmuram ir sava trieciena enerģija, tāpēc to izmantošanas trūkums ir šāds: nav iespējams ar vienu trieciena āmuru veikt pārbaudes dažāda izmēra pētāmajiem objektiem.

[004] Ir zināmas dinamiskās būvju un konstrukciju stāvokļa novērtēšanas metodes, kas ietver svārstību izraisīšanu gruntī ar speciālajam ierīcēm (pneimatiskais āmurs, vibrators) [5, 6]. Sākumā grunts svārstības izraisa būves pamatu svārstības, vēlāk arī visas būves svārstības.

Sensorus stiprina pie konstrukciju elementiem un fiksē svārstību frekvences. Jo stingāks ir konstrukcijas mezgls, jo augstāka ir atstarotā svārstību frekvence sensorā un otrādāk. Metodes trūkums ir slodžu parametru ierobežojumi un potenciālā iespēja bojāt konstrukciju vai tās daļu.

[005] Ir zināmas akustiskas nesagraujošas kontroles metodes materiāla defektu un struktūras izmaiņu novērtēšanai. Viena no plašāk izmantojamajām kontroles metodēm ir ultraskaņas metode [7], saskaņā ar kuru raidītājs nosūta ultraskaņas impulsu materiālā, kur, sastopot defektus, ultraskaņas vilnis daļēji atstarojas, tad uztvērējs ultraskaņu svārstības pārveido elektriskajās un atveido informāciju uz ultraskaņas defektoskopa ekrāna [8]. Metodes trūkums – nav iespējams izmantot šādu konstrukciju mezglu izmaiņu novērtējumam kā, piemēram, spēles palielināšana skrūvsavienojumā.

[006] Ir zināmas nesagraujošas būvkonstrukciju stāvokļa kontroles metodes, kas balstās uz elektromagnētisko svārstību novērtējumu, kas rodas dinamiskas slodzes ietekmē [9]. Metodes trūkums – var izmantot tikai metāla būvkonstrukcijām, kurām piemīt magnētiskās īpašības.

[007] Ir zināma kontroles metode, kas balstās uz lineāro paātrinājumu, kas rodas būvkonstrukcijas mezglos dinamiskas slodzes ietekmē, analīzi. Paātrinājumi tiek reģistrēti ar akselerometru palīdzību [10]. Mērījumu augstas precizitātes nodrošināšanai lieto platjoslas vibrācijas pārveidotājus – pjezoelektriskos sensorus. Dinamiskā slodze tiek izraisīta, izmantojot mākslīgus vibrācijas avotus, piemēram, uz būvkonstrukciju no noteiktā augstuma uzmetot objektu ar noteiktu masu. Šī metode tiek plaši izmantota zemestrīču seku noteikšanai, kā arī būvkonstrukciju kontrolei. Metodes trūkums – nav iespējams pilnvērtīgi novērtēt būvkonstrukciju stāvokli, it īpaši būvkonstrukciju mezglus, jo pieliktās vibrācijas slodzes frekvence un trieciena enerģija ir relatīvi zemas: 0,1–150,0 Hz un 200–250 J attiecīgi. Turklāt būvkonstrukciju mezglu pilnvērtīgu kontroli ierobežo tikai lineāro akselerometru izmantošana, ko paredz šī metode [9], kas ir pieņemta par izgudrojuma prototipu.

Izgudrojuma mērķis un būtība

[008] Izgudrojuma mērķis ir izstrādāt metodi būvkonstrukciju savienojošo mezglu nesagraujošai kontrolei, kas nodrošinās pieliekamas trieciena-vibrācijas slodzes paplašinātu parametru diapazonu (trieciena impulsa frekvenci no 50 līdz $5x10^4$ Hz, slodzes pielikšanas ātrumu no 5 līdz 50 m/s un trieciena enerģiju diapazonā no 0,1 līdz 10,0 kJ), kā arī nodrošinās

vienlaicīgu atbildes signālu fiksāciju, izmantojot tam vairākus lineāros un leņķiskos akselerometrus (4) (1. zīm. un 2. zīm.).

[009] Izgudrojuma būvkonstrukcijas savienojošo mezglu nesagraujošas kontroles metodes shēma ir parādīta 1. zīmējumā. Lai realizētu izgudrojuma metodi, ir nepieciešama trieciena ierīce (3) (vai induktors (9) un impulsa ģenerators (10), kā parādīts 2. zīmējumā), akselerometri (4), impulsa uztvērējs (5), signāla analizators (6) un darbstacija (datu apstrādes sistēma) (7). Signālu reģistrēšanu ar akselerometriem (4) vienlaicīgi veic trijos telpiski atdalītos punktos: vietā, kur pielikta slodze, un abās pusēs attiecībā pret pētāmo būvkonstrukcijas elementu savienojuma mezglu (mezgla tuvumā). Turklāt izgudrojuma metode paredz iegūto datu turpmāko analīzi, kontrolējot korelācijas funkcijas no koaksiālajiem trīs lineārajiem un trīs leņķiskajiem paātrinājumiem, kurus mēra katrs no akselerometriem (4). Saskaņā ar vispārzināmo metodiku [11] integrēto diagnostikas parametru aprēķina, pamatojoties uz sākotnējiem signāliem, kas saņemti no sensoriem (akselerometriem (4)), un matemātiski apstrādātiem signāliem, kas izturējuši frekvences filtrēšanu. Šādā veidā būvkonstrukcijas elementu savienojuma mezglu stāvokli raksturo ar sešiem paātrinājumiem attiecībā pret slodzes pielikšanas vietu.

[010] Konstruējot savstarpējās korelācijas funkcijas starp lineāro un leņķisko sensoru (akselerometru (4)) koaksiālajiem pāriem un aprēķinot savstarpējās korelācijas funkciju nosaka integrālos diagnostikas parametrus. Integrālais diagnostikas parametrs ietver savstarpējas korelācijas funkciju neatkarīgu parametru algebrisko izteiksmi, piemēram, funkcijas maksimālo vērtību, funkcijas apgabala integrālo daļu un tās kvalitātes koeficientu (Q koeficientu). Integrēto diagnostikas parametru var aprēķināt gan no sākotnējiem signāliem, kas saņemti no sensoriem (akselerometriem (4)), gan no matemātiski apstrādātiem signāliem, jo īpaši no tiem, kuri ir izturējuši frekvences filtrēšanu. Ar frekvences filtrēšanu sākotnējie signāli tiek ievesti interesējošajā frekvenču diapazonā, kam raksturīgs lielākais informācijas apjoms par pārbaudāmā mezgla stāvokli, jo īpaši sistēmas svārstību dabisko frekvenču zonā.

[011] Pieliekamas slodzes parametru diapazona paplašināšana, kā arī akselerometru (4) atbilžu signālu matemātiskā apstrāde (izmanto lineārās un leņķisko sensoru koaksiālo pāru savstarpējās korelācijas funkciju konstruēšanas metodi un savstarpējās korelācijas funkciju integrālo diagnostikas parametru aprēķinu) ļauj veikt pilnvērtīgāku būvkonstrukciju stāvokļa analīzi

salīdzinājuma ar prototipa metodi, jo signāla amplitūdas un citu parametru izmaiņas norādīs uz būvkonstrukciju elementu savienojuma bojājumiem, proti, uz mezgla stinguma izmaiņām.

[012] Lai nodrošinātu metodes augstu efektivitāti un pieliekamas slodzes plaša diapazona parametru regulēšanu, būvkonstrukcijas slogošanai izmanto impulsa elektromagnētisko lauku ar intensitāti 10–100 MA/m un iespēju regulēt impulsa amplitūdu un frekvenci, kā arī slogošanas ātrumu. Slogošanu var veikt ar vienu impulsu vai vairākiem secīgiem impulsiem ar frekvenci no 1 līdz 30 impulsiem minūtē. Metāla būvkonstrukciju nesagraujošas kontroles metodes shēma ir parādīta 2. zīmējumā.

[013] Izgudrojuma metode ietver šādus secīgus soļus (1. zīm. un 2. zīm.):

i) apseko būvkonstrukciju ar mērķi noteikt tās statisko shēmu;

ii) nosaka būvkonstrukciju elementu savienojumu mezglus, kuriem ir vislielākā ietekme uz būvkonstrukcijas darbību;

iii) izvēlās pētāmo būvkonstrukciju elementu (1) un (2) savienojuma mezglu;

iv) izvēlās dinamiskās slodzes (trieciena vai vibrācijas) pielikšanas vietu;

v) izvieto akselerometrus (4) trijos telpiski atdalītos punktos: vietā, kur pielikta slodze, un abās pusēs attiecībā pret pētāmo būvkonstrukcijas elementu (1) un (2) savienojuma mezglu (mezgla tuvumā), lai kontrolētu paātrinājumu koaksiālitāti virzienos, kas atbilst pētāmā būvkonstrukciju elementu (1) un (2) savienojuma mezgla brīvības pakāpēm;

vi) savieno akselerometrus (4) ar kopējo signāla analizatoru (6), kuru savukārt savieno ar darbstaciju (7);

vii) pieliek dinamisko slodzi ar trieciena ierīci (3) vai induktoru (9) būvkonstrukcijas elementam (1) vai (2);

viii) veic akselerometru (4) rādītāju (atbilžu signālu) salīdzinājuma rezultātu matemātisko apstrādi (izmanto lineārās un leņķisko sensoru koaksiālo pāru savstarpējās korelācijas funkciju konstruēšanas metodi un savstarpējās korelācijas funkciju integrālo diagnostikas parametru aprēķinu – saskaņā ar vispārzināmo metodiku [11]);

ix) analīzē iegūtus rezultātus;

x) secina par būvkonstrukcijas elementu (1) un (2) savienojuma mezgla stāvokli.

[014] Izgudrojums ir skaidrots ar šādiem zīmējumiem:

1. zīm. Būvkonstrukcijas nesagraujošas kontroles metodes shēma: pirmais būvkonstrukcijas elements (1), otrais būvkonstrukcijas elements (2), trieciena ierīce (3), akselerometri (4), impulsa uztvērējs (5), signāla analizators (6), darbstacija (7), bultskrūves (8).
2. zīm. Metāla būvkonstrukciju nesagraujošas kontroles metodes shēma: pirmā sija (1), otrā sija (2), akselerometri (4), impulsa uztvērējs (5), signāla analizators (6), darbstacija (7), bultskrūves (8), induktors (9), impulsa ģenerators (10).
3. zīm. Akselerometra (4) lineāro un leņķisko paātrinājumu mērīšanas kanālu shēma: Φx, Φy un Φz ir leņķisko paātrinājumu mērīšanas virzieni; x, y, z – lineāro paātrinājumu mērīšanas virzieni.

Izgudrojuma īstenošanas piemēri

[015] 1. piemērs:
Pārbaudāmā būvkonstrukcija sastāv no diviem būvkonstrukcijas elementiem (1) un (2), šajā gadījumā – sijām, kuras savstarpēji ir savienotas ar bultskrūvēm (8) (1. zīm.). Būvkonstrukcijas savienojošo mezglu nesagraujošas kontroles metodes shēma ietver šādas sastāvdaļas (1. zīm.): trieciena ierīce (3), akselerometri (4), impulsa uztvērējs (5), signāla analizators (6) un darbstacija (7). Akselerometri (4) ir piestiprināti pie būvkonstrukcijas elementiem (1) un (2), kā arī pie trieciena ierīces (3). Šādā veidā akselerometri (4) ir izvietoti trijos telpiski atdalītos punktos: trieciena slodzes pielikšanas vietā un divos punktos, proti, uz pārbaudāmiem būvkonstrukcijas elementiem (1) un (2). Akselerometri (4) ar vadiem tiek savienoti ar impulsa uztvērēju (5), no kura datus pārsūta uz signāla analizatoru (6) un pēc tam uz darbstacijas (7) displeju. Ar trieciena ierīces (3) palīdzību, dotajā piemērā – 0,5 kg smagu celtniecības āmuru ar metāla uzgali – būvkonstrukcijai pieliek dinamisko slodzi ar impulsa enerģijas vērtību 0,1–1,0 kJ. Atbildes signāli no pieliktās dinamiskās slodzes vienlaikus parādās visos trijos akselerometros (4), iegūtos signālus vienlaicīgi ieraksta trijos telpiski atdalītos punktos, tad veic koaksiālo pārvietojumu korelācijas funkcijas kontroli katra akselerometra (4) trīs lineārajiem un trīs leņķiskajiem pārvietojumiem, kas atbilst sešiem paātrinājumiem attiecībā pret slodzes pielikšanas vietu. Tad veic akselerometru (4) rādījumu salīdzināšanas rezultātu matemātisko apstrādi (izmanto lineārās un leņķisko sensoru koaksiālo pāru savstarpējās korelācijas funkciju konstruēšanas metodi un savstarpējās korelācijas funkciju integrālo diagnostikas parametru aprēķinu – saskaņā ar vispārzināmo metodiku [11]), kas ir pamats secinājumiem par

būvkonstrukcijas stāvokli. Pārbaudes procesu atkārto, periodiski atlaižot vaļīgāk vai pievelkot ciešāk savienojuma bultskrūves (8). Akselerometru (4) lineāro un leņķisko paātrinājumu mērīšanas kanālu shēma ir redzama 3. zīmējumā, kur shematiski ir attēlots akselerometrs (4) ar trīs lineāro paātrinājumu mērīšanas virzieniem x, y, z un trīs leņķisko paātrinājumu mērīšanas virzieniem Φ_x, Φ_y un Φ_z.

[016] 2. piemērs:

Pārbaudāmā būvkonstrukcija kā 1. piemērā. Būvkonstrukcijas savienojošo mezglu nesagraujošas kontroles metodes shēma ietver šādas sastāvdaļas (2. zīm.): akselerometri (4), impulsa uztvērējs (5), signāla analizators (6), darbstacija (7), induktors (9) un impulsa ģenerators (10). Metāla (tērauda, alumīnija) būvkonstrukciju dinamiski slogo ar impulsa elektromagnētisko lauku, kas rodas impulsa ģeneratora (10) izlādes rezultātā uz induktoru (9). Turklāt induktors (9) ar savu svaru (var tikt pielikta arī papildu slodze) iedarbojās uz būvkonstrukciju (2. zīm.). Impulsa ģeneratora (10) akumulētā enerģija var svārstīties no 0,1 līdz 10 kJ. Papildus ir iespējams mainīt raksturu izlādes impulsa strāvai induktorā no taisnstūra uz slāpētu sinusoīdu ar frekvenci no 50 līdz $5x10^4$ Hz.

[017] 3. piemērs:

Pārbaudāmā būvkonstrukcija kā 1. piemērā, savukārt būvkonstrukcijas savienojošo mezglu nesagraujošas kontroles metodes shēma – kā 2. piemērā. Pārbaudot būvkonstrukcijas no materiāliem, kuriem nepiemīt elektrovadītspēja un magnētiskās īpašības (piemēram, no koka vai betona), būvkonstrukcijas kontakta vietā ar induktoru (9) piestiprina metāla plāksni no alumīnija vai vara. Šādā veidā panāk elektromagnētiskās ietekmes ievērojamo palielināšanos uz būvkonstrukcijas materiālu un var veikt būvkonstrukciju nesagraujošu kontroli saskaņā ar izgudrojumu.

Informācijas avoti

[1] Zhao, J., Liu, T., Wang, Y.: Static Test Analysis of a Bridge Structure in Civil Engineering. Syst. Eng. Procedia., vol. 1, pp. 10–15, (2011). https://doi.org/10.1016/j.sepro.2011.08.003.

[2] Brozovsky, J.: Comparsion of compressive strenghts of concrete testing by different of Sclerometers. In: Procedia Engineering, vol. 65, pp. 245–259, (2013). https://doi.org/10.1016/j.proeng.2013.09.039.

[3] Kowalski, R., Wróblewska, J.: Application of a sclerometer to the preliminary assessment of concrete quality in structures after fire. Arch. Civ. Eng. vol. 64, pp. 171–186, (2018). https://doi.org/10.2478/ace-2018-0069.

[4] Wang, T., Celik, O., Necati Catbas, F., Zhang, L.: Practical calibration techniques for the modal impact hammer. In: Conference Proceedings of the Society for Experimental Mechanics Series, vol. 5, pp. 23–29, (2015). https://doi.org/10.1007/978-3-319-15212-7_3.

[5] Shamim, J.A., Abu Sayed, J.M., Bhowmik, P.K.: Design of a Model Dynamic Load Testing Machine. International Conference on Mechanical, Industrial and Energy Engineering, Paper No: MIE12-064, (2012) . https://doi.org/10.13140/2.1.4494.7522.

[6] Batuev, G.S. et al.: Engineering methods for studying shock processes. (Инженерные методы исследования ударных процессов). Moscow: Mechanical Engineering, p. 240, (1977).

[7] Guo, W., Xu, H., Liu, Z., Shi, J.: Ultrasonic technique for testing cold welding of butt-fusion joints in polyethylene pipe. In: American Society of Mechanical Engineers, Pressure Vessels and Piping Division, Paper No: PVP2013-97205, (2013). https://doi.org/10.1115/PVP2013-97205.

[8] Ultraskaņas defektoskopija, TUV NORD Baltik. [skatīts 2021. gada 13. maijā]. Pieejams: https://www.tuv-nord.com/lv/lv/pakalpojumi/testesana/konstrukciju-un-materialu-testesana-ar-nesagraujosas-kontroles-metodem-ndt/ultraskanas-defektoskopija-ut/

[9] Satapathy, S., Stefani, F., Saenz, A.: Crack tip behavior under pulsed electromagnetic loading. In: IEEE Transactions on Magnetics, vol. 41, pp. 226-230, (2005). https://doi.org/10.1109/TMAG.2004.838743.

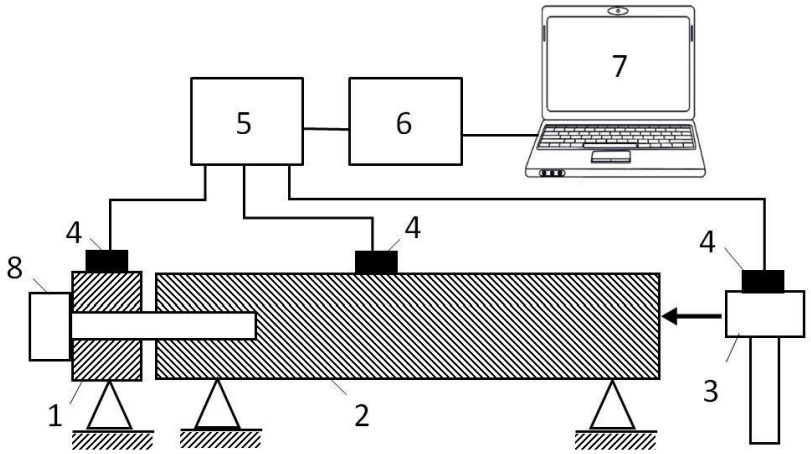
[10] Maksimenko, O.: The diagnosis is made by the string (Диагноз ставит струна). Science and life (Наука и жизнь), vol. 6, (2003). Pieejams: https://www.nkj.ru/archive/articles/2973/

[11] Sokolov, N., Kulak, V.: A modern approach to vibration testing: the transition from abstraction to real data. /Современный подход к виброиспытаниям: переход от абстракции к реальным данным/ Vestnik metrologa, Nr.1, (2014).

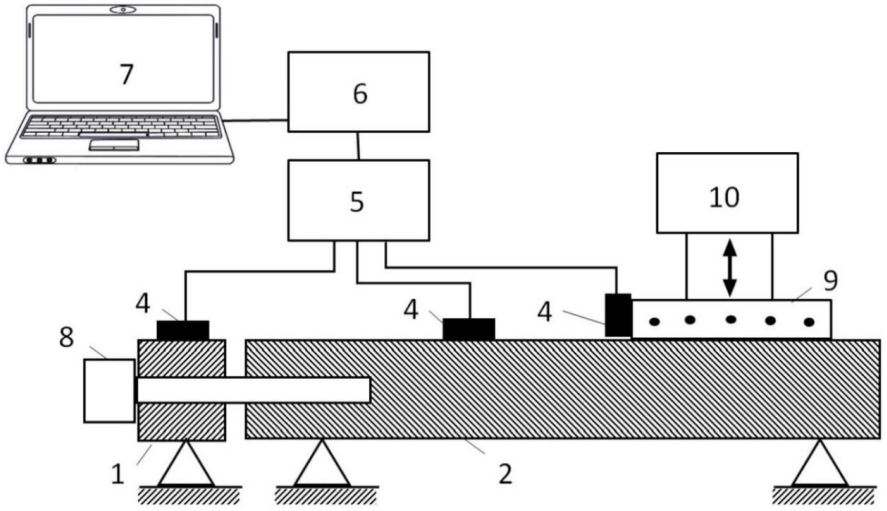
PRETENZIJAS

1. Būvkonstrukciju savienojošo mezglu nesagraujošas kontroles metode, kas ietver trieciena vai vibrācijas slodzes radīšanu un atbildes signāla reģistrēšanu, izmantojot akselerometrus (4), kas ir piestiprināti pie būvkonstrukcijas elementiem (1) un (2), kas atšķiras ar to, ka atbildes signālus vienlaicīgi reģistrē ar akselerometriem (4), kas uzstādīti trijos telpiski atdalītos punktos: trieciena vai vibrācijas slodzes pielikšanas punktā un divos punktos pētāmās būvkonstrukcijas elementu (1) un (2) savienojuma zonā abās pusēs attiecībā pret pētāmo būvkonstrukcijas elementu (1) un (2) savienojuma mezglu, turklāt akselerometru (4) rādījumu rezultātu matemātisko apstrādi veic, konstruējot lineāro un leņķisko akselerometru koaksiālo pāru korelācijas funkcijas, tad pēc frekvenču filtrācijas veic sākotnējo signālu un iegūto signālu integrālo diagnostikas parametru salīdzinājumu, balstoties uz kura rezultātiem secina par būvkonstrukcijas savienojošo mezglu stāvokli.

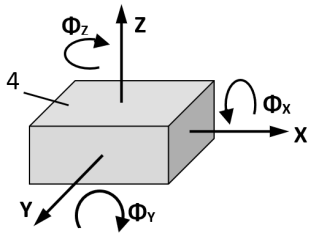
2. Būvkonstrukciju savienojošo mezglu nesagraujošas kontroles metode saskaņā ar 1. pretenziju, kas atšķiras ar to, ka trieciena vai vibrācijas slodzi rada, iedarbojoties vienu vai vairākas reizes uz būvkonstrukcijas elementu (1) vai (2), ar impulsa elektromagnētisko lauku.



1. zīm.



2. zīm.



3. zīm.

REFERENCES

[1] Tol S, Özgüven HN. Dynamic characterization of bolted joints using FRF decoupling and optimization. Mech Syst Signal Process. 2015; 54–55:124–138. doi:10.1016/j.ymssp.2014.08.005.

[2] Zhan J, Zhang F, Siahkouhi M. A step-by-step damage identification method based on frequency response function and cross signature assurance criterion. Sensors. 2021; 21(4):1029. doi:10.3390/s21041029.

[3] Yang B, Xuan FZ, Xiang Y, Li D, Zhu W, Tang X, et al. Lamb wave-based structural health monitoring on composite bolted joints under tensile load. Materials. 2017; 10(6):652. doi:10.3390/ma10060652.

[4] Rucka M. Monitoring steel bolted joints during a monotonic tensile test using linear and nonlinear Lamb wave methods: a feasibility study. Metals. 2018; 8(9):683. doi:10.3390/met8090683.

[5] Xu J, Wang C, Li H, Zhang C, Hao J, Fan S. Health monitoring of bolted spherical joint connection based on active sensing technique using piezoceramic transducers. Sensors. 2018; 18(6):1727. doi:10.3390/s18061727.

[6] Zhang M, Tang Z, Yun CB, Sui X, Chen J, Duan Y. Bolt looseness detection using SH guided wave and wave energy transmission. Smart Mater Struct. 2021; 30(10):105015. doi:10.1088/1361-665X/ac1d90.

[7] Stolze FHG, Worden K, Manson G, Staszewski WJ. Fatigue-crack detection in a multi-riveted strap-joint aluminium aircraft panel using amplitude characteristics of diffuse Lamb wave field. Materials. 2023; 16(4):1619. doi:10.3390/ma16041619.

[8] Liang Y, Feng Q, Li D, Cai S. Loosening monitoring of a threaded pipe connection using the electromechanical impedance technique—experimental and numerical studies. Sensors. 2018; 18(11):3699. doi:10.3390/s18113699.

[9] Zhu J, Qing X, Liu Q, Liu X, Wang Y. Monitoring of fiber-reinforced composite single-lap joint with electromechanical impedance of piezoelectric transducer. Materials. 2019; 12(19):3241. doi:10.3390/ma12193241.

[10] Caldwell SP, Radford DW. Composite single lap shear joint integrity monitoring via embedded electromechanical impedance sensors. J Compos Sci. 2023; 7(2):53. doi:10.3390/jcs7020053.

[11] Caldwell SP, Radford DW. The health monitoring of bonded composite joints using both thickness and radial impedance resonance responses. Sensors. 2024; 24(8):2508. doi:10.3390/s24082508.

[12] Serdjuks D, Kurtenoks V, Tatarinovs A, Mironovs V, Lapkovskis V, Buka-Vaivade K, Macevics A, Topcijs K, Vilnitis M. Method of coaxial accelerations correlation for quality assessment of structural joints. Procedia Struct. Integr. 2022; 37:547–554. doi:10.1016/j.prostr.2022.01.121.

[13] Serdjuks D, Kurtenoks V, Tatarinovs A, Buka-Vaivade K, Lapkovskis V, Mironovs V, Podkoritovs A, Topcijs K. Non-model vibration analysis method for health monitoring of structural joints. Procedia Struct. Integr. 2022; 37:555–562. doi:10.1016/j.prostr.2022.01.122.

[14] Buka-Vaivade K, Kurtenoks V, Serdjuks D. Non-destructive damage detection of structural joint by coaxial correlation method in 6D space. Buildings. 2023; 13(5):1151. doi:10.3390/buildings13051151.

[15] Kurtenoks V, Kurajevs A, Buka-Vaivade K, Serdjuks D, Lapkovskis V, Mironovs V, Podkoritovs A, Vilnitis M. The quality assessment of timber structural joints using the coaxial correlation method. Buildings. 2023; 13(8):1929. doi:10.3390/buildings13081929.
[16] Muttillo M, Stornelli V, Alaggio R, Paolucci R, Di Battista L, de Rubeis T, et al. Structural health monitoring: an IoT sensor system for structural damage indicator evaluation. Sensors. 2020; 20(17):4908. doi:10.3390/s20174908.
[17] Murray-Bergquist L, Bernauer F, Igel H. Characterization of six-degree-of-freedom sensors for building health monitoring. Sensors. 2021; 21(11):3732. doi:10.3390/s21113732.
[18] Fink M. Time reversal of ultrasonic fields. I. Basic principles. IEEE Trans Ultrason Ferroelectr Freq Control. 1992; 39(5):555–566. doi:10.1109/58.156174.
[19] Zeng L, Lin J, Huang L. A modified Lamb wave time-reversal method for health monitoring of composite structures. Sensors. 2017; 17(5):955. doi:10.3390/s17050955.
[20] Du F, Xu C, Wu G, Zhang J. Preload monitoring of bolted L-shaped lap joints using virtual time reversal method. Sensors. 2018; 18(6):1928. doi:10.3390/s18061928.
[21] Liang Y, Feng Q, Li D. Loosening monitoring of the threaded pipe connection using time reversal technique and piezoceramic transducers. Sensors. 2018; 18(7):2280. doi:10.3390/s18072280.
[22] Xu C, Wu G, Du F, Zhu W, Mahdavi SH. A modified time reversal method for guided wave-based bolt loosening monitoring in a lap joint. J Nondestruct Eval. 2019; 38:85. doi:10.1007/s10921-019-0626-1.
[23] Du F, Xu C, Zhang J. A bolt preload monitoring method based on the refocusing capability of virtual time reversal. Struct Control Health Monit. 2019; 26(8):e2370. doi:10.1002/stc.2370.
[24] Wang F, Song G. Bolt early looseness monitoring using modified vibro-acoustic modulation by time-reversal. Mech Syst Signal Process. 2019; 130:349–360. doi:10.1016/j.ymssp.2019.04.036.
[25] Panagiotopoulos CG, Stavroulakis GE. A numerical study on computational time reversal for structural health monitoring. Signals. 2021; 2(2):225–244. doi:10.3390/signals2020017.
[26] Sutin A, Kurtenoks V, Sabatier J, Burgett R, O'Neil M, Aranchuk S, et al. Time-reversal acoustic focusing of waves produced by seismic vibrators. J Acoust Soc Am. 2006; 120(5 Suppl):3369.
[27] Sutin A, Libbey B, Kurtenoks V, Fenneman D, Sarvazyan A. Nonlinear detection of land mines using wide bandwidth time-reversal techniques. Proc. SPIE 6217, 62171B (2006). doi:10.1117/12.673714.
[28] Fillinger L, Kurtenoks V, Rosenblum S, Sutin A, Sarvazyan A. Flexible tools for time reversal acoustics focusing applications. J Acoust Soc Am. 2007; 122(5 Suppl):3009. doi:10.1121/1.2942748.
[29] Fillinger L, Kurtenoks V, Lewis G Jr, Sutin A, Sarvazyan A. Time-reversal ultrasound system for enhanced drug delivery in the rat brain. In: Abstracts of the 9th International Symposium on Therapeutic Ultrasound; 2009 Sep; Aix-en-Provence, France. p. 105.
[30] Fu H, Sharif Khodaei Z, Aliabadi MHF. An event-triggered energy-efficient wireless structural health monitoring system for impact detection in composite airframes. IEEE Internet Things J. 2019; 6(1):1183–1192. doi:10.1109/JIOT.2018.2867722.
[31] Smetskaja V, Litvinenko A, Kurtenoks V, Stepanovs V, Lapkovskis V, Bespal'ko V. Study on thermal stability of multi-channel picosecond precise time-tagging system. In: 2023

IEEE 10th Jubilee Workshop on Advances in Information, Electronic and Electrical Engineering (AIEEE). 2023; 87–90. doi:10.1109/AIEEE58915.2023.10134855.

[32] Lapkovskis V, Litvinenko A, Kurtenoks V, Stepanovs V, Smetska V, Bespal'ko V. Multichannel synchronization for picosecond time-tagging system. In: 2023 IEEE 10th Jubilee Workshop on Advances in Information, Electronic and Electrical Engineering (AIEEE). 2023; 81–86. doi:10.1109/AIEEE58915.2023.10134773.

[33] Bespal'ko V, Litvinenko A, Stepanovs V, Kurtenoks V, Smetska V, Lapkovskis V. Compensation of Accuracy Error for Time Interval Measurements. Latvian J Phys Tech Sci. 2024; 61(1):43–51. doi:10.2478/lpts-2024-0005.



Viktors Kurtenoks dzimis Tukumā. Viņš ieguvis bakalaura grādu (1991) un maģistra grādu (1992) datortehnikā Rīgas Tehniskajā universitātē (RTU). Pašlaik viņš ir RTU doktora studiju programmas "Būvniecība" doktorants un SIA "Eventech" tehnoloģiju direktors. Viņa pētniecības intereses ir saistītas ar konstrukciju strukturālā stāvokļa monitoringu, augstas precizitātes laika mērīšanas instrumentāciju, signālu apstrādi, uz FPGA balstītām mērījumu sistēmām un laika reversijas metodēm konstrukciju savienojumu diagnostikā.

Viktors Kurtenoks was born in Tukums. He obtained a Bachelor's degree (1991) and a Master's degree (1992) in Computer Engineering from Riga Technical University (RTU). Currently, he is a doctoral student of the Doctoral Study Programme "Civil Engineering" at RTU and Chief Technology Officer at Eventech Ltd. His research interests focus on structural health monitoring, high-precision timing instrumentation, signal processing, FPGA-based measurement systems, and time-reversal methods for diagnostics of structural joints.



Viktors Kurtenoks was born on 2 December 1969 in Tukums. He obtained a Bachelor's degree (1991) and a Master's degree (1992) in Computer Engineering from Riga Technical University (RTU). From 2001 to 2008, he worked as a senior software/hardware/firmware designer at Artann Laboratories (Trenton, USA). He is currently Chief Technical Officer at Eventech Ltd, one of the leading developers of event timers and time taggers, and Chief Technical Officer leading full-cycle development at his own companies Digits Ltd and Juvitek Ltd; he also works at RTU. He is a doctoral student in the Doctoral Study Programme "Civil Engineering" at RTU.

His expertise covers full product development from idea to functional unit, high-speed digital, analogue and mixed-signal electronics, ultra-fast ICs (ADC, DAC, memory), DSP, microcontrollers and FPGA/CPLD design in VHDL.